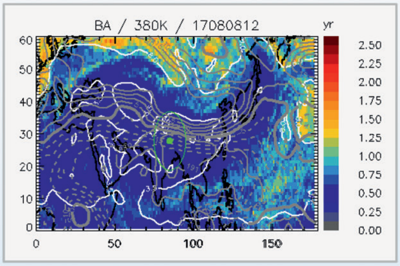

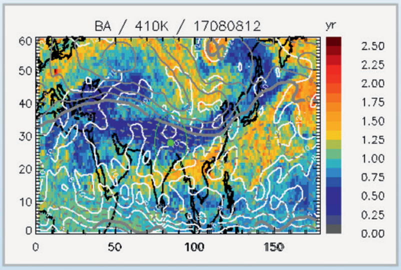

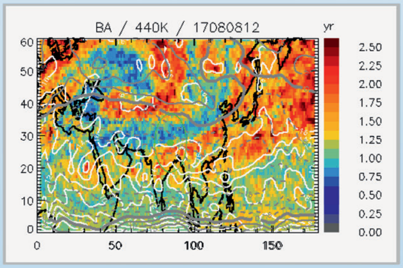

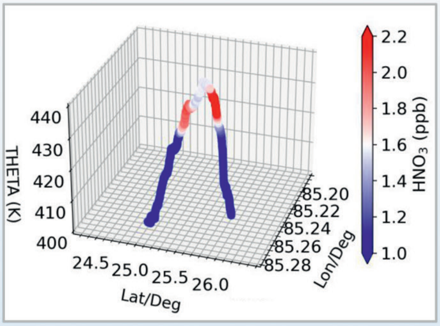

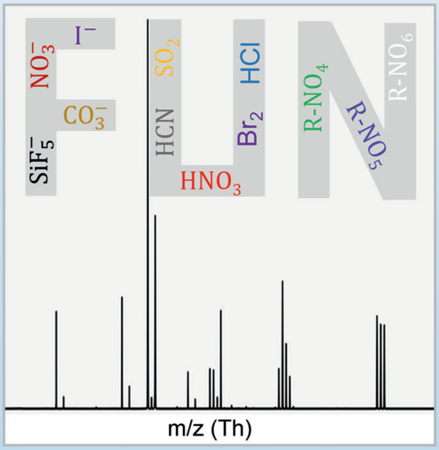

Atmospheric Trace Gas Measurements Using Chemical Ionisation Time-of-Flight Mass Spectrometry

Yun Li

Energie & Umwelt / Energy & Environment
Band / Volume 526
ISBN 978-3-95806-520-8

Mitglied der Helmholtz-Gemeinschaft

JÜLICH
Forschungszentrum

JÜLICH
Forschungszentrum

UNIVERSITY OF WUPPERTAL

DOCTORAL THESIS

Atmospheric Trace Gas Measurements Using Chemical Ionisation Time-of-Flight Mass Spectrometry

---

Author:
Yun LI

Supervisor:
Prof. Dr. Thorsten BENTER

A thesis submitted for
the degree of
Doctor of Natural Sciences

in the

School of Mathematics and Natural Sciences

March 23, 2020

The PhD thesis can be quoted as follows:

urn:nbn:de:hbz:468-20210429-145000-0
[http://nbn-resolving.de/urn/resolver.pl?urn=urn%3Anbn%3Ade%3Ahbz%3A468-20210429-145000-0]

DOI: 10.25926/7bwh-yd49
[https://doi.org/10.25926/7bwh-yd49]

Forschungszentrum Jülich GmbH
Institut für Energie- und Klimaforschung
Stratosphäre (IEK-7)

Atmospheric Trace Gas Measurements Using Chemical Ionisation Time-of-Flight Mass Spectrometry

Yun Li

Schriften des Forschungszentrums Jülich
Reihe Energie & Umwelt / Energy & Environment Band / Volume 526

ISSN 1866-1793 ISBN 978-3-95806-520-8

Bibliografische Information der Deutschen Nationalbibliothek.
Die Deutsche Nationalbibliothek verzeichnet diese Publikation in der
Deutschen Nationalbibliografie; detaillierte Bibliografische Daten
sind im Internet über http://dnb.d-nb.de abrufbar.

Herausgeber und Vertrieb: Forschungszentrum Jülich GmbH
Zentralbibliothek, Verlag
52425 Jülich
Tel.: +49 2461 61-5368
Fax: +49 2461 61-6103
zb-publikation@fz-juelich.de
www.fz-juelich.de/zb

Umschlaggestaltung: Grafische Medien, Forschungszentrum Jülich GmbH

Druck: Grafische Medien, Forschungszentrum Jülich GmbH

Schriften des Forschungszentrums Jülich
Reihe Energie & Umwelt / Energy & Environment, Band / Volume 526

D 468 (Diss. Wuppertal, Univ., 2020)

ISSN 1866-1793
ISBN 978-3-95806-520-8

Vollständig frei verfügbar über das Publikationsportal des Forschungszentrums Jülich (JuSER)
unter www.fz-juelich.de/zb/openaccess.

Abstract

Atmospheric trace gases whose concentrations range from parts per million by volume (ppt) to parts per quadrillion by volume (ppq) undergo complicated microphysical and chemical processes in the lower atmosphere and play a significant role in climate by indirectly affecting the global radiative feedback through particle formation processes. This work presents the first detailed validation and interpretation of nitric acid (HNO_3), hydrogen cyanide (HCN) and some other relevant trace gases measured during the first two campaign deployments of the innovative Time-of-Flight Chemical Ionisation Mass Spectrometer FunMass. The two campaigns span science objectives as versatile as upper tropospheric and lower stratospheric processes above the Asian Monsoon region for the 2017 StratoClim campaign and the nighttime oxidation of isoprene for the 2018 NO_3-Isoprene campaign.

The Asian Summer Monsoon (ASM) is the dominant circulation system in boreal summer. During high monsoon season, air in the highly polluted Asian boundary is rapidly transported into the Upper Troposphere and Lower Stratosphere (UTLS) by strong convective activities, where it is horizontally retained in the Asian Monsoon Anticyclone (AMA). With the upwelling motion inside the upper part of the AMA, these air pollutants can enter the global stratosphere, potentially affecting the worldwide climate.

During the StratoClim aircraft campaign from Kathmandu, Nepal, in July and August 2017, FunMass was deployed onboard the high-altitude research aircraft M55-Geophysica. On August 6 and 8 of the campaign, the first two successful high spatial and temporal resolution in-situ measurements of gaseous HNO_3 and HCN with high spatial and temporal resolution were carried out inside the AMA. The atmospheric concentrations of HNO_3 and HCN were calibrated with reference to gravimetrically controlled permeation devices. HNO_3 was further referred to ion-chromatographic analyses. The in-situ measurements show a good agreement with satellite observations, i.e. HNO_3 from Aura-MLS and HCN from ACE-FTS. Tracer correlations have been studied with CO and O_3 obtained by the airborne instruments COLD and FOZAN, respectively.

The HCN observations show significant vertical and horizontal signatures within the AMA which have been analysed by backward trajectory analyses employing the Lagrangian models TRACZILLA and CLaMS. Some of the structures are consistent with the CO measurements indicating quite recent convective events while some segments show CO enhancements without obvious HCN features, which is attributed to different origin regions. Measurements in both flights point to the existence of a layer with enhanced HCN at $\sim$ 365 K potential temperature level which probably is the main convective outflow layer.

A filament of high HNO_3 and O_3 correlated with high HCN signatures between 420 – 437 K was observed uncorrelated with any convective activities. A mean Age of Air (AOA) analysis employing long forward modelling nearly perfectly explains the formation of the filament as isentropic mixing of older HCN rich air from middle or high latitude lower stratosphere with high HCN which was caused by an overall strong enhancement from peatland burning in winter 2015 – 2016.

Given its good performance in measuring HNO_3 in the UTLS, FunMass was coupled to the SAPHIR chamber to measure HNO_3 with an improved concentric-DBD ion source while studying the nighttime oxidation of isoprene (C_5H_8), one of the most prominent and abundant Biogenic Volatile Organic Compounds (BVOCs), by NO_3 radicals in the atmospheric simulation chamber SAPHIR in July and August 2018. This process is deemed to play a major role in Secondary Organic Aerosol (SOA) formation. An online calibration unit employing the established permeation device was connected to the inlet line. HNO_3 formation from selected experiment days under very different conditions (with changes in isoprene, NO_2, O_3, humidity,

photolysis, *etc.*) is discussed. The first detection of organic nitrates is reported herein employing mass peaks corresponding to the respective CO_3^--clusters, especially the Isoprene Nitrate Peroxide (INP) as the first-generation product from the oxidation of isoprene by NO_3 radicals. FunMass showed a quite good response and signal-to-noise ratio for the INP measurements and also good to very good correlations with other parallel measurements, mainly by the Br^- -CIMS and Vocus-PTR instruments. However, quite a strong variation in absolute responses on different measurement days were identified, which remains up-to-date unexplained. FunMass contributed excellent HNO_3 measurements and has shown great potential for the measurement of highly oxidized SOA precursors like INP.

Apart from the relevant atmospheric results presented herein, this thesis has shown that FunMass can perform as an extremely sensitive tool for the analysis of various atmospherically relevant processes under extreme conditions in the upper troposphere and lower stratosphere as well as for ground-based and chamber-based measurements.

Contents

List of Figures

List of Tables

List of Abbreviations

AC	Alternative Current, 10 KHz
ACE	Atmospheric Chemistry Experiment
AIRS	Atmospheric infrared sounder
AMA	Asian Monsoon Anticyclone
AOA	Age of Air
ATAL	Asian Tropopause Aerosol Layer
ATTL	Asian Tropopause Transition Layer
BDC	Brewer-Dobson Circulation
BVOCs	Biogenic Volatile Organic Coumpounds
CCMs	Chemistry Climate Models
CIMS	Chemical Ionization Mass Spectrometry/Spectrometer
CLaMS	Chemical Lagrangian Model of the Stratosphere
CLS	Confined Lower Stratosphere
COPAS	COndensation Particle counting System
CPT	Cold Point Tropopause
CRDS	Cavity Ring Down Spectroscopy
DBD	Dilectric Barrier Discharge
ECMWF	European Centre of Medium-Range Weather Forecasts
EOS	Earth Observing System
FEP	Fluorinated ethylene propylene
FOV	Field of View
FS	Free Stratosphere
FTS	Fourier Transform Spectrometer
HV	High Voltage
IC	Ion Chromatography/Chromatographic
ID	Inner Diameter

IEK-7	Institute of Energy and Climate: Stratosphere
IEK-8	Institute of Energy and Climate: Troposphere
IF	Ion Funnel
IMR	Ion-Molecular Reaction
IS	Ion Source
LRM	Laps Rate Minimum
m/z	mass-to-charge ratio
MCP	multichannel plate
MLS	Microwave Limb Sounder
MSS	Mission Support System
MVK	Methyl Vinyl Ketone
OD	Outer Diameter
PFA	Perfluoroalkoxy alkanes
ppb	parts ber billion (by volume)
ppm	parts per million (by volume)
ppq	parts per quadrillion (by volume)
ppt	parts per trillion (by volume)
PTFE	Polytetrafluoroethylene
RF	Radio Frequency
SAPHIR	Simulation of Atmospheric PHotochemistry In a large Reaction Chamber
sccm	standard cubic centimetre per minute
slm	standard litre per minute
SOA	Secondary Organic Aerosols
TOC	Top of Confinement
ToF	Time-of-Flight
TTL	Tropical Tropopause Layer
UHSAS	Ultra-High Sensitivity Aerosol Spectrometer
UTLS	Upper Troposphere and Lower Stratosphere
VOCs	Volatile Organic Compounds
x_*A*	the concentration or mixing ratio of *A*, where *A* stands for chemical species ausch as H_2O, HNO_3, HCN, *etc.*

ZEA-1	Central Institute of Engineering, Electronics and Analytics: Engineering
ZEA-2	Central Institute of Engineering, Electronics and Analytics: Electronic Systems
ZEA-3	Central Institute of Engineering, Electronics and Analytics: Analytics

Chapter 1

Introduction

Measurements of important atmospheric trace gases play a key role in understanding very different regimes of the changing atmosphere. This thesis reports atmospheric measurements employing one of the most sensitive techniques for measuring trace gases — Chemical Ionization Mass Spectrometry (CIMS) — to learn about climate relevant processes in the Upper Troposphere and Lower Stratosphere (UTLS) above the Asian Monsoon region as well as the oxidation of plant emissions in the atmospheric boundary layer.

1.1 The Asian Monsoon Anticyclone

The Asian Monsoon Anticyclone (AMA) is the dominant circulation system in boreal summer, which have a global influence on variations in air composition and meteorology. It is a large anticyclonic vortex with high pressure in the centre, located in the Asian UTLS and contrary to the cyclonic vortex with low pressure in the centre above the Asian surface in the monsoon season [114]. The AMA covers the domain of $10° - 50°$ N and $60° - 110°$ E, spreading from the Mediterranean in the west to the West Pacific Ocean in the east.

Figure 1.1 schematically depicts the location and dynamics of the AMA in high monsoon season. Through deep convection and a conduit air is pumped from the heavily polluted Asian surface rapidly into the upper troposphere, facilitating transport of water and air pollutants into the lower stratosphere that moisten and pollute this relatively dry and clean atmospheric layer [101, 37, 103, 114, 78, 152]. Previous studies have speculated the formation of the Asian

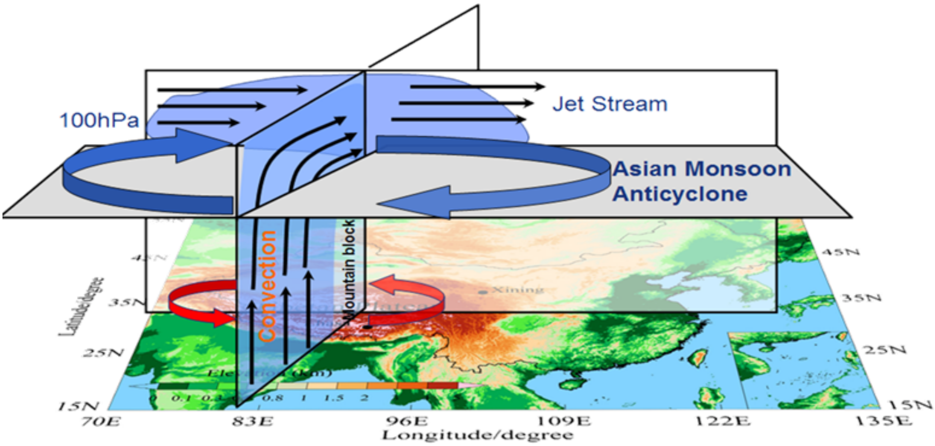

Figure 1.1: Depiction of the location and dynamics of the AMA from Dr. Yong Wang.

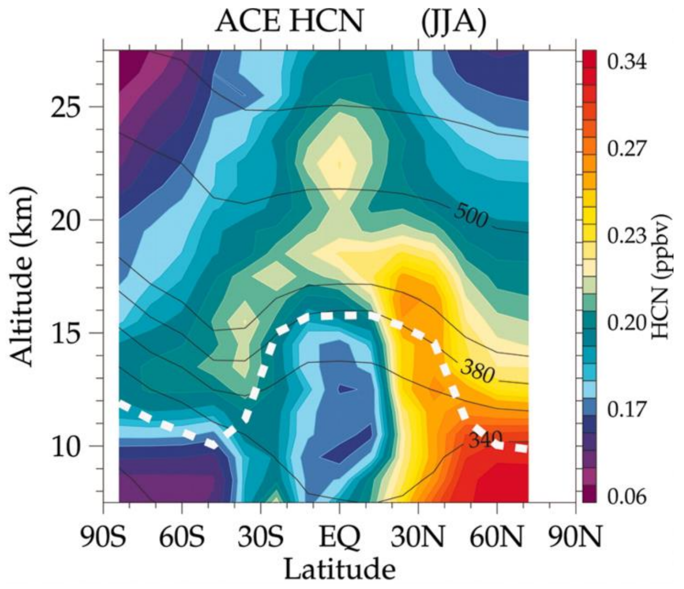

Figure 1.2: HCN Climatology from ACE-FTS observations during July – August in the AMA [114].

Tropopause Aerosol Layer (ATAL) is closely associated with the rise of Asian surface emissions — both aerosols and precursor gases — into the AMA [139, 155]. A very recent study shows [55] that ammonium nitrate particles are formed in the upper troposphere from the upward transport of ammonia from ground sources during Asian monsoons. This study employed satellite observations, high-altitude aircraft measurements, atmospheric trajectory simulations and cloud-chamber studies. Particles formed in the UTLS involving HNO_3, H_2SO_4 or primary organic aerosols affect the radiative budget by reflecting sunlight back into space or trap heat in the atmosphere, in turn influencing the monsoon weather and climate [83].

The AMA is consequently impacting not only the Asian monsoon region but also the global atmosphere. The climatology of HCN in Fig. 1.2 shows the propagation of polluted air into the deep stratosphere. Trace gases of tropospheric origin being enhanced and confined into the AMA have been observed by satellites [38, 39, 73]. The modelling study by Vogel and co-authors indicated that air masses in the AMA make their way into the lower stratosphere like an upward spiralling ascent [144]. The balloon-borne measurements based on the southern slopes of the Himalayan mountain further suggested the air in the AMA is transported upwards and then distributed "above the top of confinement" of the anticyclone and it can be transported to all directions especially northward to the extratropical lowermost stratosphere but also (to a minor fraction) into the tropical tropopause layer (TTL) [15], which is in agreement with the modelling study [145]. Analyses on the hydrogen cyanide (HCN) observations from the ACE-FTS satellite suggested that the quasi-isentropic eddy shedding and mixing at around 400 K (potential temperature, Θ) in the AMA [37, 112] can lead to a fast (weeks to months) influence of air uplifted in the AMA in both the equatorial and the high-latitude lower stratosphere, eventually entering the ascending branch of the Brewer-Dobson circulation (BDC) [114]. This has also been further supported by balloon-sonde measurements, aircraft observations and modelling studies [156, 96].

Understanding the air composition in the AMA is of vital importance to clarify the dynamical, microphysical and chemical processes that are highly relevant to the ATAL, ozone and climate. Satellite observations tend to have very good spatial and temporal coverage, but the resolution and sensitivity are mostly not high enough to identify and analyse underlying smaller-scale processes. Model simulations are of great help to understand atmospheric dynamics and chemistry. However, the parametrization in chemistry climate models (CCMs) still needs to be further improved to produce more reliable results due to insufficient representation of convection, mixing or heterogeneous chemistry. Carrying out in-situ measurements of particles and trace gases with different origins (tropospheric or stratospheric origin) and obtaining corresponding high-resolution profiles in the Asian UTLS enable us to study climate-relevant physical and chemical processes that influences the air composition in the UTLS in a rather small region. Meanwhile, in-situ measurements also help to improve the parametrization of CCMs for better prognostic performances.

1.2 Measuring atmospheric trace gases with Chemical Ionization Mass Spectrometry

Biogenic and anthropogenic emissions are happening every moment releasing volatile inorganic and organic compounds into the natural atmosphere and changing its chemical composition. Although dry or wet deposition helps to remove chemicals, a large number of them remain in the atmosphere. These chemicals are vulnerable to different chemical and physical processes. The mixing ratio of atmospheric trace gases ranges from parts per million by volume (ppm) to parts per quadrillion by volume (ppq). Sulphur dioxide (SO_2), nitric acid (HNO_3) and hydrogen cyanide (HCN) in the UTLS are some of the widely discussed trace gases with different origins. The primary sources of SO_2 are volcanic eruptions and energy industry activities [33]. HNO_3 in the troposphere is mainly produced from the oxidation of NO_x(= NO + NO_2), while the photolysis of N_2O is primarily responsible for the formation of HNO_3 in the stratosphere. HCN is mainly emitted from biomass or biofuel burning processes [137, 116]. These trace gas species play a significant role in the formation of aerosols in the UTLS either by direct gas-particle partitioning due to their low volatility and large solubility [9, 121, 84] or by contributing after chemical conversion [137, 116].

Chemical Ionization Mass Spectrometry(CIMS) has been widely used in the past decades to carry out atmospheric trace gas measurements with a high temporal resolution and a low detection limit.

Different ionisation techniques are applied to conduct atmospheric trace gas measurements with quadrupole mass spectrometers. Primary airborne measurements for SO_2 and reactive nitrogen gases with CIMS were carried out by Möhler and co-authors at 1980s and 1990s [67, 95, 92, 93]. HNO_3 was measured with $CO_3^-(H_2O)_n$ in the UTLS at mid-latitudes [125] and the same technique was later applied to a ground-based measurement of HNO_3 and SO_2 [45]. Huey and co-authors studied the reactions of SF_6^- and I^- with reactive nitrogen precursors (e.g., N_2O_5) and co-products (e.g., HNO_3 and $ClNO_2$) with CIMS in the laboratory [57] and later carried out CIMS measurements of HNO_3 and SO_2 using SF_6^- ionisation at the South Pole [58]. Kita [65] developed a SiF_5^--CIMS to measure HNO_3 on the ground. HCl, HNO_3 and SO_2 were measured using SF_5^- as the reagent ion in the UTLS with the instrument onboard the NASA WB-57F high-altitude aircraft [87] or on the new German High Altitude and Long range research aircraft (HALO) flying in the extratropical tropopause [61, 62]. Measurements of gas-phase inorganic and organic acids, such as HONO, HNCO, HCOOH, *etc.* from biomass fires were done with negative-ion proton-transfer CIMS employing (CH_3COO^-) ionisation [137, 116, 138].

With the time-of-flight (ToF) detecting technique later being greatly improved and widely used for laboratory studies and ground-based measurements [60, 153, 4, 86], I^- ionisation high-resolution ToF-CIMS was used to conduct airborne measurements of both inorganic and organic gas species in the free troposphere [75, 76]. Whereas, ToF-CIMS has not been applied to measure trace gases in the UTLS due to the fact that the instrument has to be adapted to harsh environmental conditions to perform reliable measurements.

FunMass is a versatile ToF-CIMS that is particularly developed for airborne measurements under extreme conditions in the UTLS [64]. It has a clean and efficient ion source that can produce different reagent ions (CO_3^-, I^-, SF_6^-, *etc.*) to detect multiple atmospheric trace gases, such as SO_2, HNO_3, HCN, *etc* [2, 64]. As FunMass was later applied to a chamber study to measure HNO_3 formation during the nighttime oxidation of isoprene, it also showed capability to measure organic nitrates with CO_3^- ionisation. FunMass is capable of highly selective, sensitive and fast-responsive measurements of atmospheric trace gases as well as parallel measurements of multiple species.

1.3 Tropospheric chemistry background

Atmospheric oxidants are rich in the Earth's boundary layer, which results in enormously complicated air composition in the lower troposphere. Daytime chemistry is dominated by hydroxyl (OH) radicals initiated chain reactions in both clean and polluted atmosphere. The OH radical has different sources: (1) electronically excited oxygen atoms from the photolysis of ozone (O_3) reacting with water vapour (R1 and R2) [119], which is more important in the upper troposphere; (2) the decomposition of nitrous acid (R3) upon irradiation with light in the wavelength range from 300 to 405 nm [46, 132]; (3) recycling of OH radicals from the reaction of nitrogen monoxide (NO) with hydroperoxyl radicals (HO_2) (R4 and R5), which is usually produced from the reaction of OH with atmospheric (semi-)volatile organic compounds, especially in polluted air [131, 79].

$$\mathrm{O_3} + \mathrm{h}\nu(\lambda < 340nm) \longrightarrow \mathrm{O_2} + \mathrm{O(^1D)} \tag{R1}$$

$$\mathrm{O(^1D)} + \mathrm{H_2O} \longrightarrow 2\,\mathrm{OH} \tag{R2}$$

$$\mathrm{HONO} + \mathrm{h}\nu(300nm < \lambda < 400nm) \longrightarrow \mathrm{OH} + \mathrm{NO} \tag{R3}$$

$$\mathrm{HO_2} + \mathrm{NO} \longrightarrow \mathrm{OH} + \mathrm{NO_2} \tag{R4}$$

Since the production of OH radicals is strongly related to sunlight, the night-concentration of OH radicals is (almost) zero. The important nighttime oxidant, the nitrate (NO_3) radical, is generated from the reaction of nitrogen dioxide (NO_2) with O_3. NO_3 could further react with NO_2 to maintain an equilibrium with N_2O_5 (R5 and R6). NO_3 radicals are generated in the daytime as well, but it can hardly survive from daylight photolysis. The two species NO_3 and N_2O_5 are active in numerous atmospheric chemical systems [13].

$$\mathrm{NO_2} + \mathrm{O_3} \longrightarrow \mathrm{NO_3} + \mathrm{O_2} \tag{R5}$$

$$\mathrm{NO_3} + \mathrm{NO_2} \rightleftharpoons \mathrm{N_2O_5} \tag{R6}$$

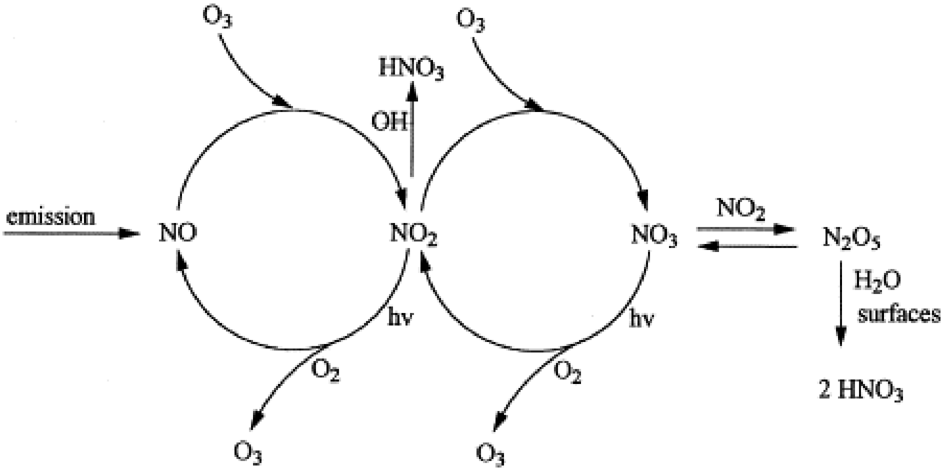

Figure 1.3: The reaction scheme of O_x-NO_x-HO_x[7]

The kinetics, mechanisms and products of the gas phase-reactions within the O_x-NO_x-HO_x system in the troposphere have been well understood. A reaction scheme has been reviewed by Atkinson [7], as is shown in Fig. 1.3. However, regarding to the chemistry involving Earth's surface emissions, the knowledge gap in understanding the changes in tropospheric composition, the formation of secondary organic aerosols (SOA) and the heterogeneous chemistry of gases on particle surfaces still exists. Poor air quality in the Earth's boundary layer results in adverse health conditions. Associations between exposure to the ambient particulate matters and chemical composition and health effects have been evaluated by Heal and co-authors [48]. The atmospheric oxidation of volatile organic compounds (VOCs) emitted from biogenic or anthropogenic sources produces notorious SOA precursors [8, 44, 19, 34, 50] and causes high ozone concentrations [66, 133] in the lower troposphere which inflict harm to crops and human beings. As one of the most abundant biogenic volatile organic compounds (BVOCs), isoprene arouses strong concern about its nighttime oxidation by the NO_3 radical due to the great uncertainty in the production of nitrates — the very active SOA precursors [99, 11, 19, 127].

1.4 Scientific questions and thesis structure

FunMass was newly developed to take part in the aircraft field campaign in Kathmandu, Nepal in high monsoon season of 2017. The campaign is part of the European project StratoClim (http://www.stratoclim.org/) to investigate the air composition and dynamical processes in the AMA as a major entry for tropospheric pollutants into the global lower stratosphere. This part of the work is focused on the following issues: (1) the distribution of HNO_3 and HCN in the AMA; (2) the influence of convective events on trace gases in the AMA; (3) the air mass origin of some local features in HNO_3 and HCN observed along the flight paths. In-situ measurements and satellite observations of HNO_3 and HCN combined with Lagrangian model simulations are used to explore the issues above.

The campaign focusing on the nighttime oxidation of isoprene by NO_3 radicals was carried out employing the atmospheric simulation chamber (SAPHIR) in the Summer 2018 with well controlled conditions. In this campaign, I aimed to measure HNO_3 production, which is a by-product during the NO_3-initiated isoprene oxidation process. The second goal was to evaluate the performance of FunMass in measuring organic gas species in comparison with parallel measurements by other ToF mass spectrometers.

Following this introduction about the atmospheric background and a brief overview of atmospheric trace gas measurements using CIMS, Chapter 2 gives a detailed description of state-of-the-art CIMS measurements by FunMass. Chapter 3 introduces the in-situ measurements of HNO_3 and HCN in the UTLS during the StratoClim aircraft campaign and puts them into perspective with satellite data. Lagrangian trajectory analyses on the in-situ data are presented in Chapter 4 in order to identify convective activities during the ASM and air mass origins of the observed air parcels. Chapter 5 is focused on HNO_3 measurements with FunMass during NO_3-initiated oxidation of isoprene and also introduces and discusses the performance of FunMass measuring organic products. Chapter 6 summarizes the work and results presented and also gives perspectives to future improvements of the technique and related research highlights.

Chapter 2

Fundamentals of the instrumentation

2.1 Chemical Ionization Mass Spectrometry

Chemical Ionization Mass Spectrometry (CIMS) is capable of selectively and sensitively measuring atmospheric trace (ppm to low ppb range) and ultra trace (low and sub ppb range) species. In CIMS, chemical species are converted to ions which are then analysed for their masses and sorted into a spectrum based on their mass-to-charge ratios (m/z, unit: the Thomson (symbol: Th)). A general chemical ionisation mass spectrometer consists of five major parts: a sample inlet, an ion source, a transfer stage, a mass analyser and a detector. Reagent ions are produced in the ion source converting sampled neutral gaseous tracers into product ion masses. Product ions are differentiated by the mass analyser according to their m/z thereafter. Thus, qualitative and quantitative analyses can be completed according to the peak information presented in a mass spectrum.

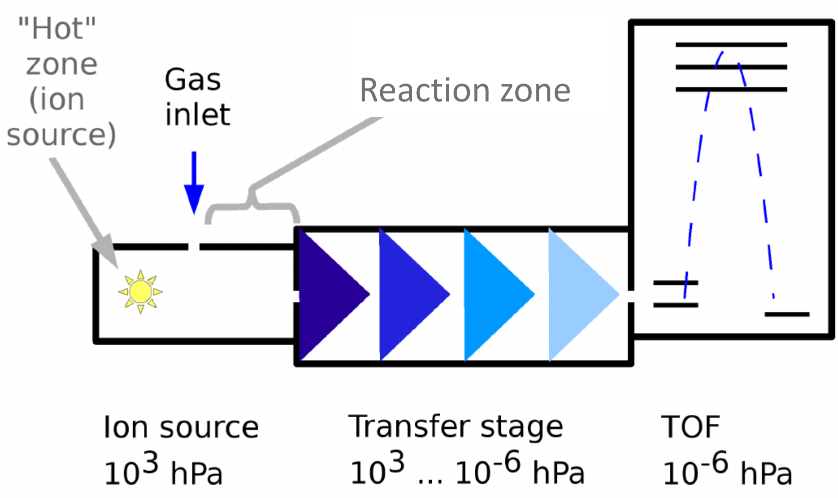

Figure 2.1: Schematic set-up of a general chemical ionisation time-of-flight mass spectrometer [2].

All instruments deployed in aircraft field campaigns are restricted by their physical sizes, weights and power consumption. Airborne instruments must meet more sophisticated standards and certifications to successfully carry out measurements considering mechanical vibrations during the flight and extremely low pressure and temperature conditions in the UTLS. All kinds of mass analysers have their own benefits and drawbacks. Quadrupole analysers have been widely used in atmospheric trace measurements, e.g. [56]. The advantages of quadrupole detectors are that they have high transmission and low ion acceleration voltages and work under moderate high-vacuum. Meanwhile they allow high scan speeds. However, monitoring a larger number of masses simultaneously only works at the cost of low time resolution which does not suit well for airborne measurements. Though ToF analysers can not compete with the best quadrupole analyser in terms of sensitivities, it is beneficial to obtain a broad range of mass peaks with fairly good sensitivity simultaneously. Hence, characterisation and realisation of parallel measurements for multiple species are feasible with Tof mass spectrometers. Measurements presented in this work were conducted with a compact ToF analyser so that it is possible to make full use of limited measuring time and to acquire full mass spectra up to > 300 Th for practically analysing multiple species at the same time.

All the measurements mentioned in this thesis were carried out with a time-of-flight chemical ionisation mass spectrometer (ToF-CIMS), which is named FunMass. It is an innovative and versatile airborne CIMS. It is equipped with a Dielectric Barrier Discharge (DBD) ion source (IS) to produce negative reagent ions, an Ion Funnel (IF) to enforce ion transfer efficiency, a ToF analyser to measure multiple species in parallel and an online gas calibration system. The DBD IS and ion funnel of FunMass were developed and characterized by Albrecht [2] and the development of the airborne instrument was primarily done by Khattatov [64]. FunMass is originally designed for airborne measurements in the UTLS, but ground-based deployment is feasible as well. Since during my doctoral study I was involved in part of FunMass development and characterization, a brief description of the theory and technique applied to FunMass is introduced in this chapter.

The weight of FunMass is about 180 Kilograms and its size is 140 cm × 60 cm × 60 cm (L×W×H). Figure 2.2a shows an image of the instrument. All components and connections among them are schematically shown in Fig. 2.2b. Major components (IS, IF and ToF analyser) will be detailed later. Different colours in Fig. 2.2b represent the efforts made by different institutes: Institute for Energy and Climate Research: Stratosphere (IEK-7), Central Institute of Engineering, Electronics and Analytics: Engineering (ZEA-1), Central Institute of Engineering, Electronics and Analytics: Electronic Systems (ZEA-2) and Tofwerk AG. FunMass was designed in IEK-7 and those parts produced in-house are highlighted in cyan in Fig. 2.2b; The frame holding all units together and the housing of IS, ToF and main power supply were manufactured by ZEA-1; ZEA-2 designed and built the power units for IS and IF; The complete ToF analyser with a customized transfer stage and ion optic unit was delivered by Tofwerk AG, Thun, Switzerland.

2.2 Chemical ionisation within FunMass

2.2.1 DBD ion source, ion-molecule reaction and ion funnel

A dielectric barrier discharge (DBD) is a high voltage electrical discharge between electrodes, one of which is coated by a dielectric barrier. The initial conception of the DBD IS for FunMass is shown in Fig. 2.3. The DBD IS consists of a ceramic-coated electrode (white) and a grounded electrode which is a capillary (ID ca. 80 – 100 μm). The electrode is made of stainless steel and the ceramic acts as the dielectric barrier with a thickness of about 1 mm. High voltage

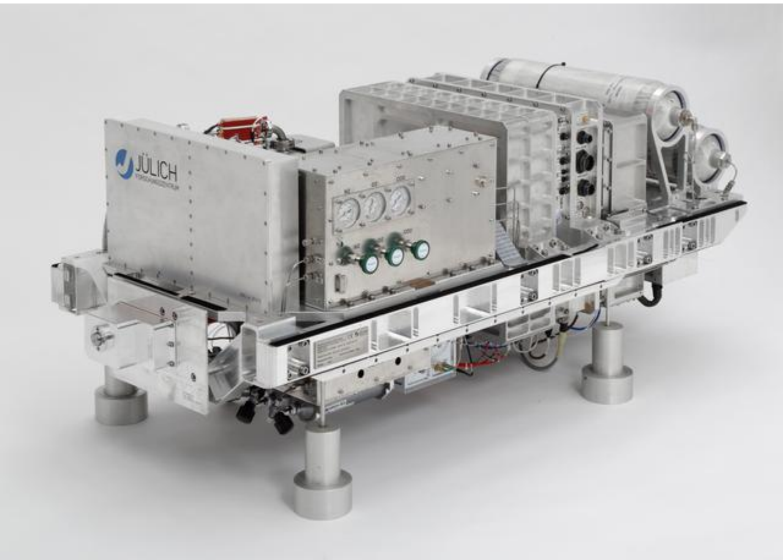

(a) Photograph of the FunMass airborne instrument (L. Limbach, Forschungszentrum Juelich)

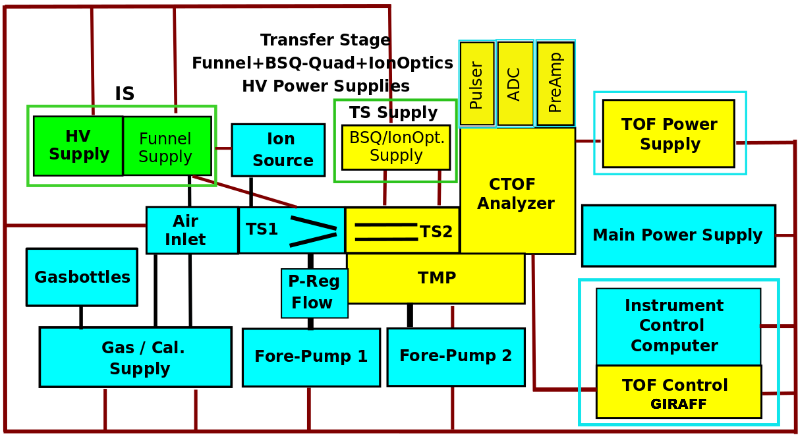

(b) Components of FunMass. Different colours indicate work done dy different institutes: ZEA-2 (green), IEK-7 (cyan) and Tofwerk (yellow). The complete structure and the housings indicated by cyan rectangles have been constructed and built by ZEA-1. [64]

Figure 2.2: The FunMass airborne instrument

(HV) (3 – 5 kV, AC) generated with a radio frequency (RF, ∼10 kHz) power supply [2] is introduced to the electrode to break down gas molecules around the ceramic, where the glow of the plasma in Fig. 2.3 is observed. A very similar setup (the standard-DBD) was used for the airborne measurements and a new development (the concentric-DBD) came later for the chamber measurements, which is introduced in the following sections.

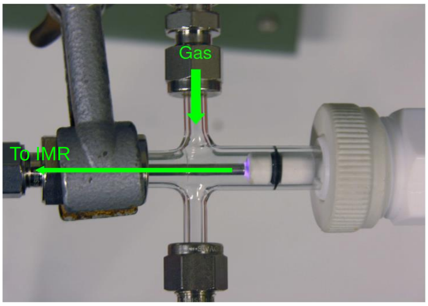

Figure 2.3: Preliminary set-up of the DBD Ion source

Multiple negative reagent ions can be produced employing the DBD IS, including "carbonate" ions (CO_3^-), nitrate ions (NO_3^-), iodide ions (I^-) as well as sulphur hexafluoride ions (SF_6^-). The pressure in the IS may vary in the range of 70 – 200 hPa, dependent on input flows. Table 2.1 summarizes the parameters that are used to produce different reagent ions. High pressure in the ion source can reduce the leakage of ambient air (during flight) in order not to pollute the ion production and also enhance collisions of ions with neutral gases to somewhat thermally relax the mixture, i.e. reducing radicals and other highly excited species. Detectable gas species with these reagent ions have been summarized by Albrecht [2].

Table 2.1: Optimal settings in the standard-DBD ion source for different reagent ions

Reagent ion (m/z, Th)	High voltage (kV)	IS pressure (hPa)	IS flow	Carrier flow
CO_3^- (60)	2 – 5	∼ 120	2 sccm CO_2 (5.0)	450 sccm O_2 (6.0)
I^- (127)	3 – 4	100 – 180	20 sccm CH_3I	400 sccm N_2 (6.0)
			(125 ppm in N_2)	
NO_3^- (62)	∼ 3	80 – 100	600 sccm synthetic air	
SiF_5^- (123)	∼ 5	80 – 120	40 sccm SF_6/SiF_4	500 sccm N_2 (6.0)
			(165/330ppm in N_2)	

After exiting the IS reagent ions expose themselves to analytes in the ion-molecule reaction (IMR) chamber, which is about 15 cm long and where ions collide and react with analyte molecules. Laboratory experiments with FunMass suggest that product ions are formed in the IMR chamber via either charge exchange reaction (R7) or nucleophilic addition (R8). Pressure in the IMR chamber was maintained at ∼ 25 – 35 hPa by a dry scroll pump (IDP-3, Agilent) at the speed of 60 L min^{-1}. The transition time of gases and ions in the chamber is estimated to be 2 s, allowing for sufficient ion-molecule reactions to turn all analytes into ions.

Charge exchange:

$$A + R^- \longrightarrow R + A^- \tag{R7}$$

Nucleophilic addition:

$$A + R^- \longrightarrow RA^- \tag{R8}$$

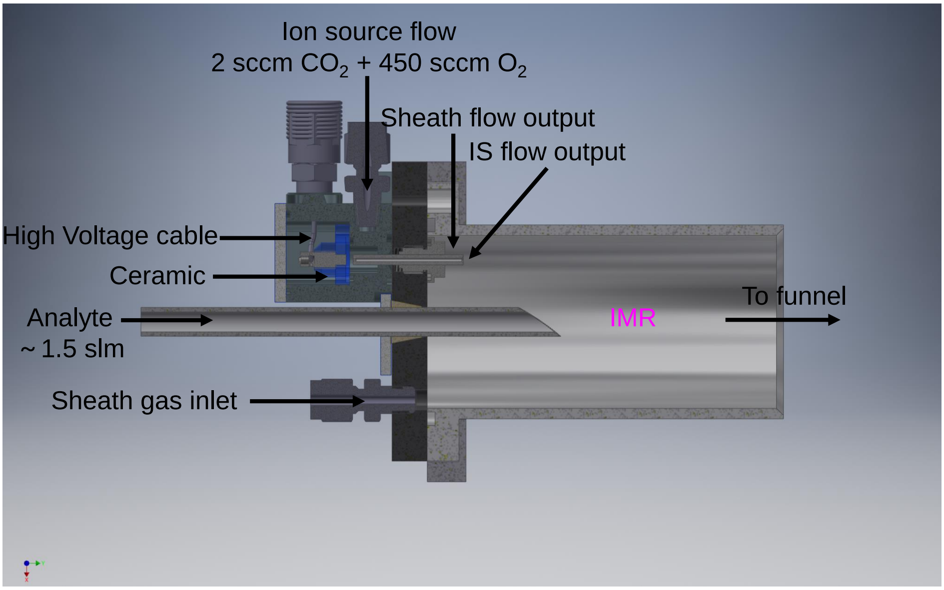

Figure 2.4: Cross-section of the standard-DBD Ion source and flow settings during airborne measurements.

Entering the IF, ion-molecule reactions continue but most of the ions are collected inside the funnel while more than 90 % of the neutral gas is pumped away. Only about 100 standard cubic centimetre per minute (sccm) from a total flow of around 2 standard litre per minute (slm) in the IMR is transported into the orifice, however, with an enhanced ion abundance. More details about the ion-molecule reaction stage are given in the work of Albrecht and Khattatov [2, 64].

2.2.2 Standard-DBD ion source

The DBD IS used for airborne measurements, later referred to as standard-DBD, was a very compact and more robust version of the preliminary IS in Fig. 2.3. Figure 2.4 shows the cross-section of the IS and IMR chamber. A highly efficient reagent ion for detecting HNO_3 is the carbonate ion ($CO_3{}^-$) [95, 45] produced from a CO_2-O_2 gas mixture passing through the IS. A 20 mm × 10 mm ceramic plate (the blue colour in Fig. 2.4) is mounted in the backplate of the IMR. The HV electrode is introduced into the ceramic plate. A 5 cm long ID = 0.1 mm capillary on the opposite side of the ceramics acts as the grounded electrode. The discharge is burning between the ceramic plate and the capillary which transfers the reagent ion gas flow into the IMR. A third flow can be introduced into the IMR region via the sheath gas inlet either as a sheath flow or to prompt the formation of reactive cluster ions for analysing specific species, for example, $CO_3{}^- \cdot (H_2O)_n$ or $I^- \cdot (H_2O)_n$ clusters ($n \geq 1$).

The dominant negative ion initially produced in an electric discharge in pure O_2 is $O_3{}^-$ [41, 122]. O_2 molecules become charged initially with the addition of an electron, generating $O_2{}^-$ (R9) and O^- (R10). Then the three body reaction forms $O_3{}^-$ (R11). $CO_3{}^-$ (m/z=60) is formed via the three body reaction of O^- attaching to CO_2 (R12) or from $O_3{}^-$ reacting with CO_2 (R13).

$$O_2 + e \longrightarrow O_2{}^- \tag{R9}$$

$$\mathrm{O_2 + e \longrightarrow O^- + O} \tag{R10}$$

$$\mathrm{O_2 + O^- + M \longrightarrow {O_3}^- + M} \tag{R11}$$

$$\mathrm{CO_2 + O^- + M \longrightarrow {CO_3}^- + M} \tag{R12}$$

$$\mathrm{{O_3}^- + CO_2 \longrightarrow {CO_3}^- + O_2} \tag{R13}$$

In the IMR, ${CO_3}^-$ combines with HNO_3 to form a specific, detectable ion cluster — ${CO_3}^- \cdot HNO_3$ (m/z=123 Th) via the nucleophilic addition:

$$\mathrm{HNO_3 + {CO_3}^- \longrightarrow {CO_3}^- \cdot (HNO_3)} \tag{R14}$$

The ionisation of HCN, however, differs from HNO_3 in terms of the product ions. Instead of forming ${CO_3}^- \cdot HCN$ as the final product ion, an intensive response to the injection of HCN into the IMR appears at m/z = 26 Th, which is attributed to CN^-. It is hypothesized that ${CO_3}^- \cdot HCN$ clusters most probably decompose in the ion transfer stage and forms CN^-, though it may have formed primarily in the IMR chamber. However, the initial cluster at 87 Th was also detected in the calibrations but seemed strongly blended by an unknown species.

$$\mathrm{HCN + {CO_3}^- \longrightarrow {CO_3}^- \cdot (HCN)} \tag{R15}$$

$$\mathrm{{CO_3}^- \cdot (HCN) \longrightarrow \ \longrightarrow CN^- + HCO_3} \tag{R16}$$

On one hand the standard-DBD IS is advantageous to produce a clean spectrum dominated by reagent ions, but on the other hand it doesn't provide enough residence time for reagent ions in the IMR. The high pressure in the ion source as a result of the small capillary outlet produces a jet of ions into the IMR and the ion jet is only 2 - 3 mm wide in 5 cm downstream of the IMR, which is diagnosed by using a blocker. This results in poor mixing among reagent ions, the analyte gas and sheath flow, which then constrains the formation of product ions and called for an improvement of the DBD IS for later measurements. Despite the impact on not enough mixing, the standard-DBD IS still provided quite a good sensitivity [64].

2.2.3 Concentric-DBD ion source

Because in the standard ion source set-up, the mixing of the high speed ion gas flow from the capillary with analyte gas in the IMR chamber was not optimal. Therefore, the DBD IS has undergone a major modification for the NO_3-isoprene campaign. A concentric-DBD IS was newly developed for the ground-based HNO_3 measurements following the Eisele concentric flow design [28]. Figure 2.5a shows a cross section of the ion source. The machined ceramics part is marked with red contour. The ambient air sampling gas line and the high voltage cable are coloured in yellow and blue, respectively. The black arrows indicate the main flow directions. When 3 – 4 kV (AC) was applied to trigger the high voltage discharge, the gas in the discharge gap that is marked in red in Fig. 2.5a, is ionised and lights up appearing as the cylindrical bluish purple glow in Fig. 2.5b. As the centrally oriented ion flow and the inner analyte flow reach the IMR chamber with or without sheath gas (the cyan arrows in Fig. 2.5a), gentle mixing and rapid ion-molecule reactions take place.

A comparison of the performances of the two ion sources used for airborne measurements (standard-DBD) and chamber measurements (concentric-DBD) is shown in Table 2.2. The concentric-DBD IS enhances the production of total ions under slightly lower voltage, though it slightly reduced the reagent ion signal since the IS flow is not directly injected into the funnel. Two spectra employing the parameters in Table A.1 are shown in Fig. 2.6, obtained during background measurements in the aircraft campaign and chamber study. The standard-DBD IS conclusively produced CO_3^- and the spectrum appeared very clean. But some minor and excited species survived in the concentric-DBD IS, such as 77 Th, 80 Th, 83 Th, 95 Th, *etc.* This can be a result of the low pressure in the concentric-DBD IS, which is roughly the same as that in the ion funnel and henceforth reduces the chance that "hot" ions get deactivated from collisions but instead they reach the IMR (and may cause some additional reactions). The main advantage of the concentric DBD IS is that reagent ions are dispersed in the IMR instead of a convergent ion jet, thus ions and neutral species are better mixed allowing for more efficient conversion of analyte species into ions.

Table 2.2: The performance of DBD ion source

Ion source	high voltage (kV)	Total ion counts (TIC, cps)	Reagent ion (CO_3^-, cps)	Mass resolution
standard-DBD	3.27	1.456×10^7	1.124×10^7	366.4
concentric-DBD	2.78	1.597×10^7	9.934×10^6	580

2.3 Ion transfer stages and the time-of-flight mass analyser

After leaving the IMR through the customized 0.5 mm orifice after the ion funnel, ions enter the two transfer stages that are standard Tofwerk design. The first stage works at $\sim10^{-2}$ hPa and employs a big segmented quadrupole (termed as "BSQ" by Tofwerk AG). The second stage is an ion optic system (10^{-5} hPa), shaping the ion beam for the extractor at the ToF entrance. The pressure in the ToF is held at $< 10^{-6}$ hPa by a 4-stage Turbo pump (TC110, Pfeiffer Vacuum GmbH) that also pumps the two preceding transfer stages.

The principle of a ToF analyser is to separate ions of different m/z by their flight time along a field-free drift path of certain length. It assumes that all ions start their journey at the same time, which is achieved by pulsing ion packages out of a continuous ion beam. Figure 2.7 shows a scheme of the CToF (= compact ToF) analyser by Tofwerk AG used in FunMass. Ions leaving the transfer stages are accelerated perpendicularly to their travel direction by an extractor which releases an ultra-short electrical field pulse generated by the pulser to gain their initial potential energy (E_{el}) before entering the ToF region. The charged ions (q being the charge of the ion with mass (m), where q/m is equal to an integer number (z) of electron charges (e), and thus $q = ez$) have gained the kinetic energy E_k resulting in a q dependent velocity v. The green dashed line in Fig. 2.7 shows the drift region of ions in the CToF. In order to keep the dimension of a ToF analyser reasonable, the ions are reflected by an electrical field from the reflector and take a V-shape path (twice the length of the drift length) to the detector.

$$E_{el} = qU = ezU = \frac{1}{2}mv^2 = E_k \tag{2.1}$$

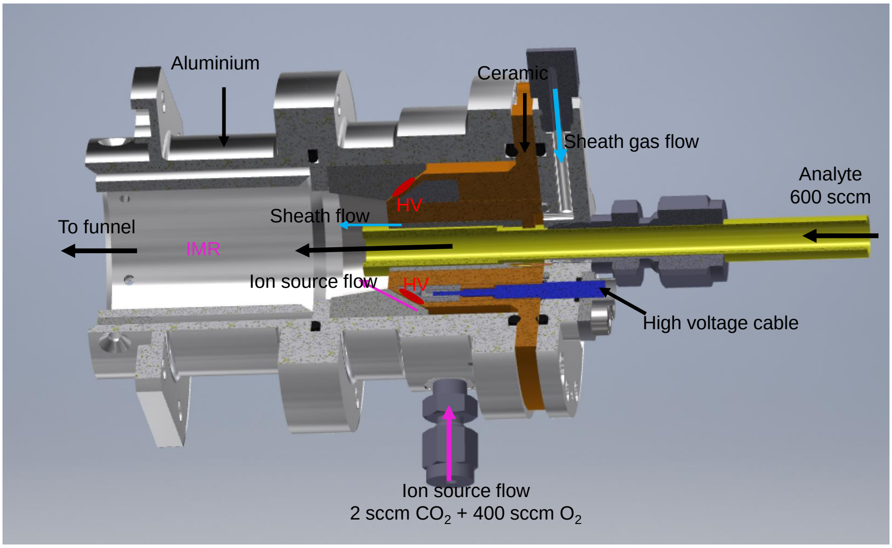

(a) Three quarters cross section of the concentric-DBD IS and flow settings during chamber measurements. The PFA analyte flow tube is in yellow

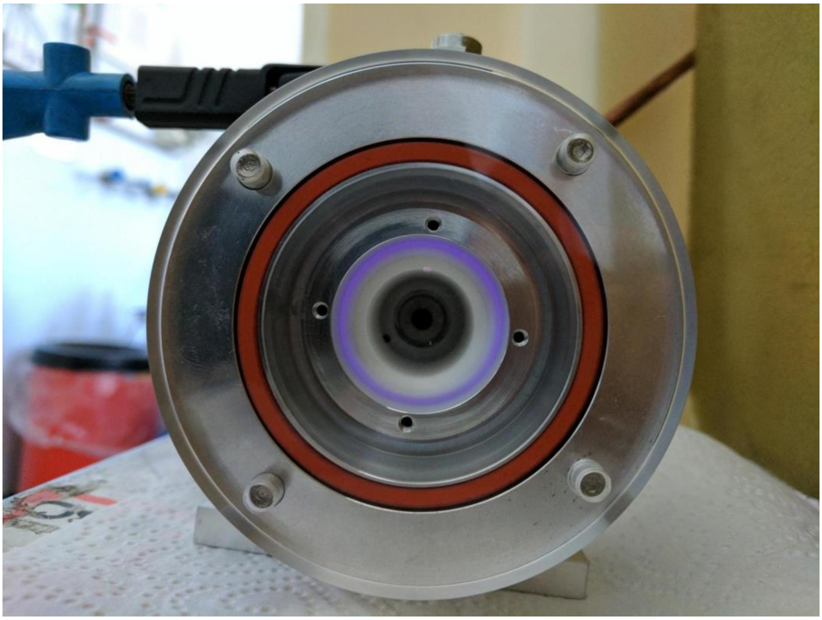

(b) The glow in concentric-DBD IS produced from the discharge of CO_2 and O_2 around the ceramic by applying 3 kV (AC) viewed (a view from the downstream side).

Figure 2.5: The concentric-DBD ion source

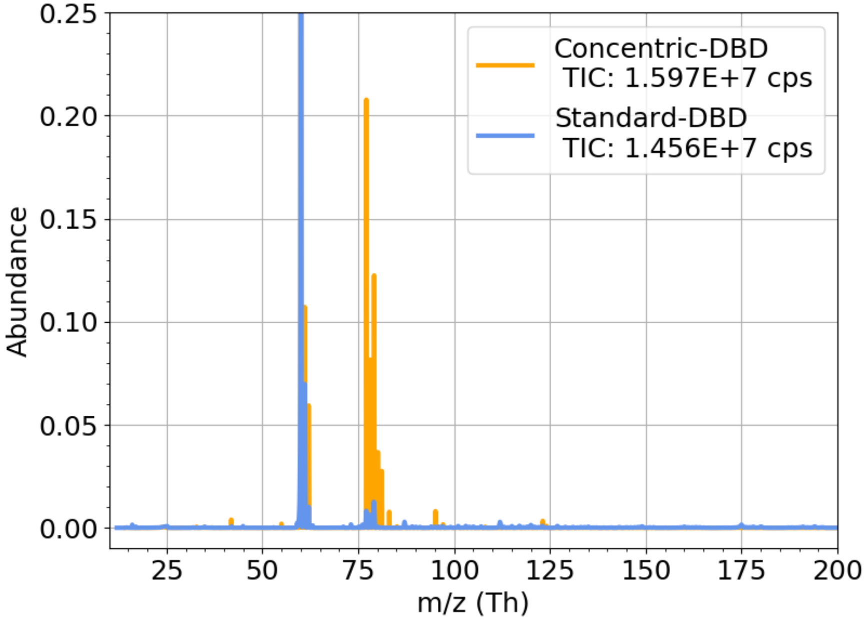

Figure 2.6: Mass spectra during blank airborne (August 6, 2017) and chamber (July 31, 2018) measurements. Note that the abundances of CO_3^- during both blank measurements are 1. Here y scale is only in the range of 0 – 0.25 to show the mass peaks better.

The velocity (v) of ions can then be calculated from 2.1 and rearranged into

$$v = \sqrt{\frac{2ezU}{m}} \tag{2.2}$$

i.e., v is inversely proportional to the square root of mass. Hence, the drift time (t) of lighter ions is shorter than that of heavier ones along a fixed length (s) of field-free space and is proportional to the square root of m/z

$$t = \frac{s}{v} = \frac{s}{\sqrt{2eU}}\sqrt{\frac{m}{z}} \tag{2.3}$$

Further, the time interval Δt between the arrival times of ions of different m/z is proportional to the difference between two different ions' square root of m/z, according to the equation 2.4.

$$\Delta t = s \times (\sqrt{\frac{m_1}{z_1}} - \sqrt{\frac{m_2}{z_2}}) \tag{2.4}$$

Therefore, extending the drift length will help to resolve ions with close m/z ratios, because ions will have larger travelling time gap to reach the detector. A ToF analyser in a larger dimension will give a longer flight path, but it will increase the size and weight and thereby limit the installation aboard aircraft and also lead to losses of ions due to collisions with residual gas and scattering as well as the divergence of the ion beam [43]. Using reflector(s) in a ToF analyser will extend the flight path by mirroring the track of ions at no cost of increasing the

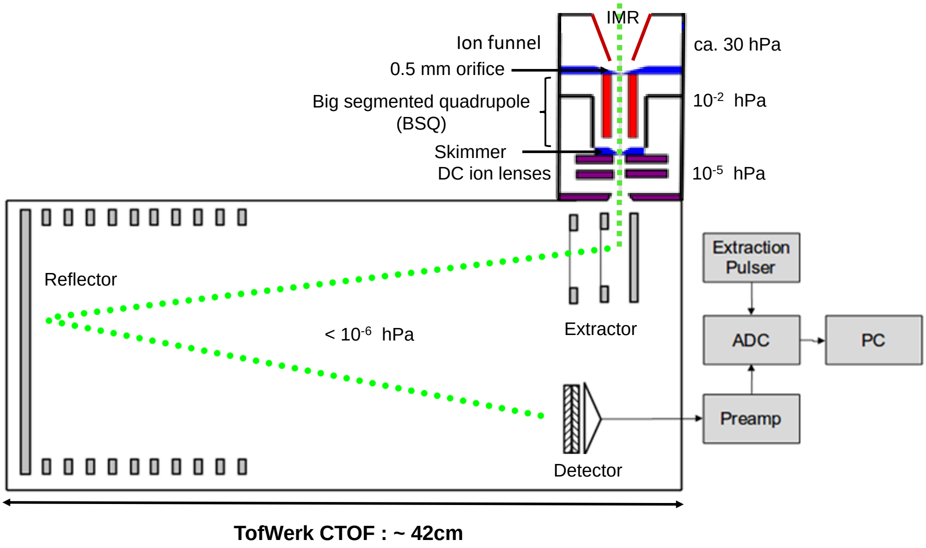

Figure 2.7: Schematic of the ion transfer stages and CToF analyser

dimension.

At the end of the flight path, ion packages hit a detector composed of multichannel plates (MCP) in time intervals of several nanoseconds (ns) to produce electric current pulses by inducing electron avalanches across the plates which are held at around 1950 V (direct current) across. The pulses are amplified by a special pre-amplifier and digitized by an extremely fast analog-to-digital converter (ADQ1600, Teledyne Signal Processing Devices Sweden AB) — ADC in short. These data are stored on a hard drive or solid state device (in-flight).

The so-called CTOF has been chosen for FunMass due to space and weight constraints. The extraction frequency of the CToF in FunMass is 60 kHz. Each extraction triggered by the pulser forms one mass spectrum and it takes 13.6 μs for each spectrum to complete recording all 21760 data points. If the time interval between two consecutive spectra is too short, high masses from the previous extraction will arrive together with low masses from the following one. A delay in each pulser is therefore applied to eliminate the interference between two spectra so that a new spectrum will not start until the previous one is completed. The digitization rate of the ADC hardware is 1 ns, which means that the dwell time of one data point dealt by the ADC is 1 ns. All raw ion signals are stored in an HDF5 file, which can be further processed. The $\sim$ 42 cm long flight path in the CToF analyser leads to a maximum resolving power of 800 which is sufficient to give well resolved mass spectra with single m/z unit resolution to identify many volatile inorganic species in the UTLS, for example, SO_2, HNO_3, HCN, *etc.*, by their respective ion clusters or breakdown products.

2.4 Quantitative analysis

2.4.1 Calibration

Raw mass signals are generally reported as ion counts per unit time, namely counts per second (cps) or Hz, in mass spectrometry. As is suggested in the work by Huey and co-authors [56] on the condition when less than a few percent of reagent ions are converted to product ions, atmospheric concentrations or mixing ratios can be determined from the equation below:

$$[A] = \frac{[A^-]}{kt[R^-]} \tag{2.5}$$

where $[A]$ is the concentration of the analyte gas in (R7); $[A^-]$ is the raw product ion signal; $[R^-]$ is the raw reagent ion signal; k and t are the effective reaction rate and time respectively. Later in the context the concentration of A is shown as x_A with A being H_2O, HNO_3, HCN, *etc.* The reaction rate constants and time of different species, therefore, have to be determined for FunMass before extracting atmospheric concentrations. Equation 2.5 can be reformed as Eq. 2.6, which means that the ratio of raw product ion to raw reagent ion – termed as normalized product ion signal from now on – is proportional to the analyte concentration. The proportionality factor (kt) is the sensitivity of FunMass to the analyte.

$$\frac{[A^-]}{[R^-]} = kt[A] \tag{2.6}$$

In this way, the proportionality factor can be determined by applying a linear regression between known amounts of analyte gas and the corresponding normalized product ion signals.

A home-made permeation oven developed by von Hobe and co-workers [51] is used to produce a certain amount of analyte in the range of its ambient mixing ratio. Figure 2.8 shows a modified drawing of this permeation oven. HNO_3 source gas is from a commercial diffusion tube (Fine Meteorology Slrs), which is filled with HNO_3 azeotrope (68 % HNO_3 + 32 % H_2O) and placed in a permeation chamber. The chamber is temperature controlled and its inner as well as all internal tubes are coated with SilcoNert-2000. Temperature in the chamber is maintained at 25 °C to keep a constant permeation rate. The flow through the oven is adjustable to produce different mixing ratios of HNO_3. But as a result of HNO_3 being very sticky, it is also advisable to use a bypass flow to later dilute the outflow from the oven rather than to change the flow through the oven for smaller x_HNO_3.

This permeation oven is used for multiple trace gas species, e.g. HNO_3, SO_2, HCN and OCS. Permeation rates of gas species can be obtained by gravimetric analysis – calculating the weight loss rates of the permeation tubes determined by regular weighing with a high-precision balance (CPA225D, Sartorius Lab Instruments GmbH & Co. KG). While this method works well for other non-sticky species, it is found to be not so reliable for determining the permeation rate of HNO_3 – k_p_HNO_3. The loss rate of HNO_3 does not always drop linearly over a year of continuous monitoring. Figure 2.9 shows the changing weight of the HNO_3 permeation tube along with time. An obvious change in the loss rate of HNO_3 happened in early July 2018, where the blue (k_p_HNO_3 = 10 ng min^{-1}) and black (k_p_HNO_3 = 25 ng min^{-1}) slopes meet each other in Fig. 2.9. Ion chromatographic (IC) analysis was carried out to obtain k_p_HNO_3 before further applying the permeation oven to a chamber study.

2.4.2 Data analysis for airborne measurements

Because online calibrations for HNO_3 and HCN measurements were not deployed during the aircraft field campaign, off-line calibrations were carried out in the laboratory with the permeation oven in Autumn 2017. Khattatov [64] described a detailed procedure for calibrating HNO_3 and HCN in the laboratory by applying k_p_HNO_3 = 6.53±0.07 ng min^{-1} and k_p_HCN = 68±2 ng min^{-1}. k_p_HNO_3 was calculated from the gravimetric analysis by applying a correction factor 0.68, because H_2O emits together with HNO_3 from the azeotrope at the same ratio.

However, HNO_3 has also been reported to decompose to NO_x when stored at high concentration [117, 91], which might cause an even slightly lower effective permeation rate.

The calibrations for HNO_3 and HCN were carried out with the same settings in all units of FunMass as for in-flight measurements. The linear correlation between normalized ion signal and x_HNO_3 or x_HCN is shown in Fig. 2.10. Peak fitting was applied to separate 26 Th from an artifact signal at 25 Th in the spectra [64]. In addition, k_p_HCN is recalculated (89.3 ng min^{-1}) with the weight loss just observed within the calibration period instead of the whole weighing history (71.2 ng min^{-1}). The proportionality factors of the linear fitting for HNO_3 and HCN calibration are 1.168×10^{-5} ppt^{-1} and 2.258×10^{-7} ppt^{-1}, respectively. The corresponding detection limits for HCN and HNO_3 are 64 ppt and 0.8 ppt integrated by a 20 s period. How to obtain the concentrations of trace gases for in-flight measurements by using the linear regression equation is explained below.

To not lose data due to instrument or power issues during flights, data acquisition was automatically restarted every 20 minutes, which means that a new data file (.h5) was created every 20 minutes. The data acquisition and processing procedure written by Khattatov [64] enables us to merge all data files into one for every flight — usually $\sim$ 4 hours for Geophysica campaigns — to facilitate the data analysis.

Figure 2.11a shows the raw normalized product ion signal of HNO_3 (red dots) during the 6th flight. A 2-min-interval blank measurements of HNO_3 and HCN were done after measuring ambient air for 20 minutes. Because HNO_3 can hardly reach the true blank value within 2 minutes due to its stickiness, the average of the last 20 s blank mode signals is used as the blank value (black dots). This adds a small additional uncertainty — by a possible overestimation of the blank — to the reported HNO_3 atmospheric concentrations. We are positive that our reported accuracy of ± 30 % is accounting for all the calibration issues discussed. A polynomial fitting is applied to assume a consistent background signal (the blue line) during each flight. Subtracting background values from measurement ones will give the differences that are caused

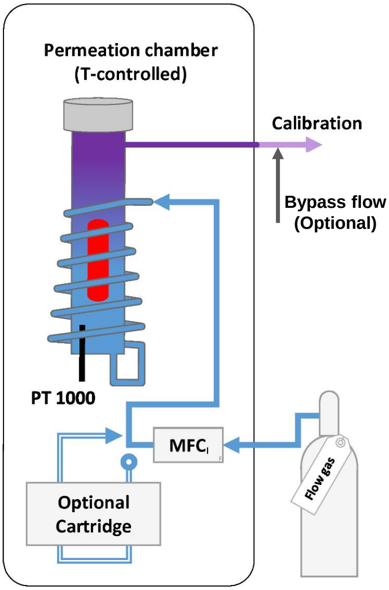

Figure 2.8: The adapted diagram of the permeation oven [51]

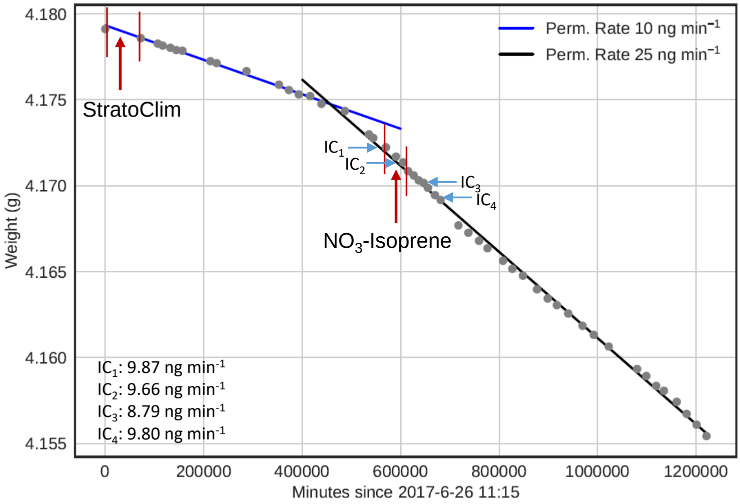

Figure 2.9: Gravimetric analysis of the HNO_3 permeation device.The blue and black linear regressions yield loss rates of 10 ng min $^{-1}$ and 25 ng min^{-1} respectively. The red arrows point to the time periods when the StratoClim and NO_3-Isoprene campaign took place. The blue arrows show when the IC analyses were done and the corresponding permeation rates are listed in the lower left corner.

by certain amounts of analyte species. Figure 2.11b shows the concentrations of HNO_3 from the 6th flight of the StratoClim campaign derived with this calculation. Determination of HCN mixing ratio in the UTLS is done following the same procedure, however, without a possible interference by overestimation of blanks.

2.4.3 Data analysis for chamber measurements

Measurements of HNO_3 in a chamber study were carried out as described in Chapter 5 with online calibration employing the permeation oven. But due to the dramatic change of the $k_p\_HNO_3$ right before the chamber experiments, IC analyses were carried out by trapping HNO_3 into water before applying the permeation oven to chamber measurements. 800 sccm synthetic air that ran through the oven was connected to a PTFE wash bottle, where HNO_3 dissolved into 250 mL water (milli-Q, >18.18 MΩ·cm) because of its extremely high solubility. This process was kept for around 2 weeks. Both the beginning and ending time of HNO_3 collection were recorded. Water was readily refilled into the wash bottle during the collection to ensure HNO_3 was not lost together with the carrier gas. The solution was then subjected to IC analysis in the Central Institute of Engineering, Electronics and Analytics (ZEA-3) in Forschungszentrum Jülich. The average $k_p\_HNO_3$ is 9.53±0.1 ng min^{-1}, which is only 40 % of the value derived from gravimetric analysis as is indicated by the black line in Fig. 2.9. Determining $k_p\_HNO_3$ from gravimetric analysis is based on the assumption that HNO_3 stays stable and only HNO_3 is emitted from the permeation tube, which in reality is not the case (subsection 2.4.1). The IC directly measures nitrate ions ($NO_3{}^-$) that only originate from HNO_3 dissolving into the water. From this point of view, the IC outcome is not influenced by the azeotropic

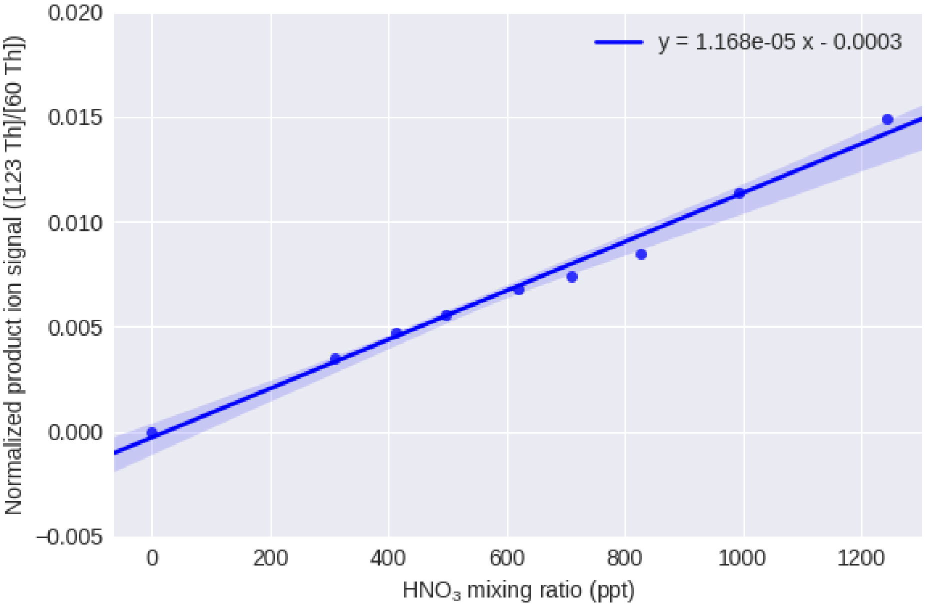

(a) Calibration for HNO_3

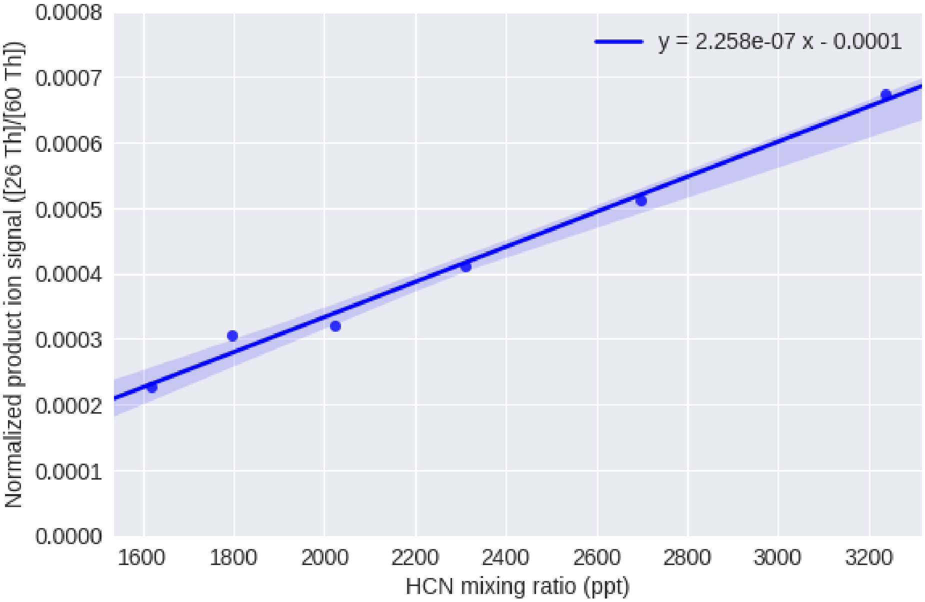

(b) Calibration for HCN

Figure 2.10: Linear regression between normalized ion signal and x_HNO_3 (a) or y_HCN (b). Mixing ratios calculated from the permeation rates are on the x-axis. Normalized product ion signal minus the blank signal is shown on the y-axis.

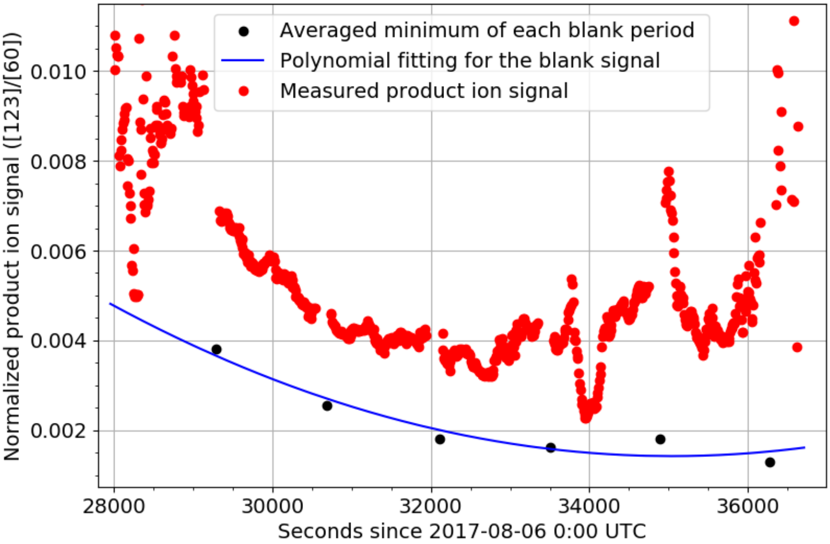

(a) Normalized product ion signals of HNO_3 during flight with an average of 10 s, measurements in red and average blank minima in black. The polynomial fitting for the background is in blue.

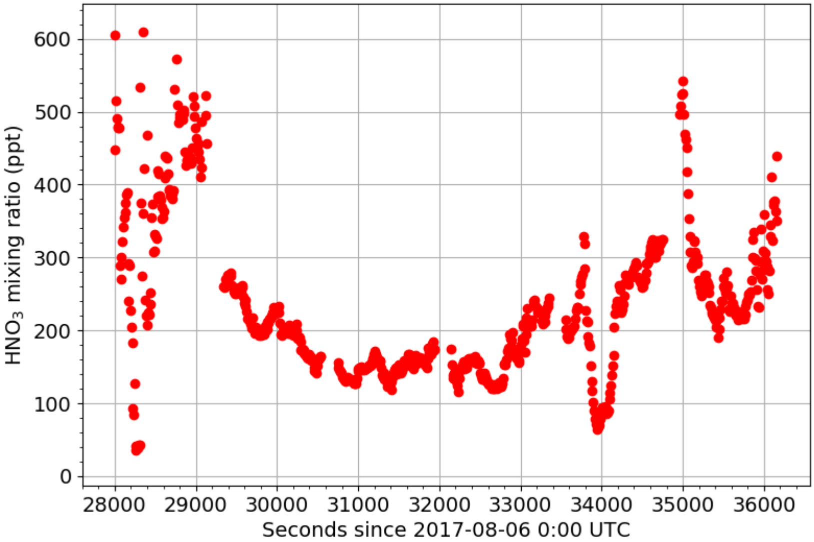

(b) Atmospheric concentrations of HNO_3 during flight by applying the calibration curve in Fig. 2.10a. Data averaged within 10 seconds.

Figure 2.11: Raw and interpreted data for in-flight measurements

mixture or the decomposition of HNO_3 and is therefore applied to the HNO_3 measurements in the chamber study, given that it has been widely adopted in a number of studies [57, 45, 65].

An example of the calibration process is shown in Fig. 2.12. The online calibration for the chamber measurements was conducted by running 800 sccm zero air through a mass flow controller (MFC_I, see the diagram of the permeation oven) as a carrier to bring HNO_3 out from the permeation chamber. Air mixed from liquid reservoirs available at the SAPHIR chamber and therefore extremely dry was employed in order to prevent water deposition on tubing walls. A constant flow through the permeation oven was maintained so that the equilibrium of HNO_3 on all the walls is robust and k_p_HNO_3 stays really stable. The x_HNO_3 in 800 sccm air is around 759 ppt, which will lead to the change of normalized product ion signal when switching FunMass measurement from blank mode to calibration. The following four measurement modes are applied to the calibration procedure:

mm: measuring chamber air.
bm: determining the background signal by sampling chamber air from which particles and HNO_3 have been filtered out.
cma: adding a known amount of HNO_3 from the permeation oven to blank measurements.
cmb: measuring chamber air with extra addition of HNO_3.

Determining x_HNO_3 with the help of online calibration is based on Eq. 2.7. $[A_m]$ is the x_HNO_3 to be determined. $[A_c]$ stands for the x_HNO_3 from the permeation oven (759 ppt). ΔD_c and ΔD_m are the increments of normalized product ion signals in cma and mm, respectively, compared to the background (bm) (Fig. 2.12). $[A_m]$ is calculated via Eq. 2.8. In this case, the interpretation of HNO_3 concentrations is less influenced by the background value, because enough dwell time was given to allow HNO_3 to equilibrate on walls during each

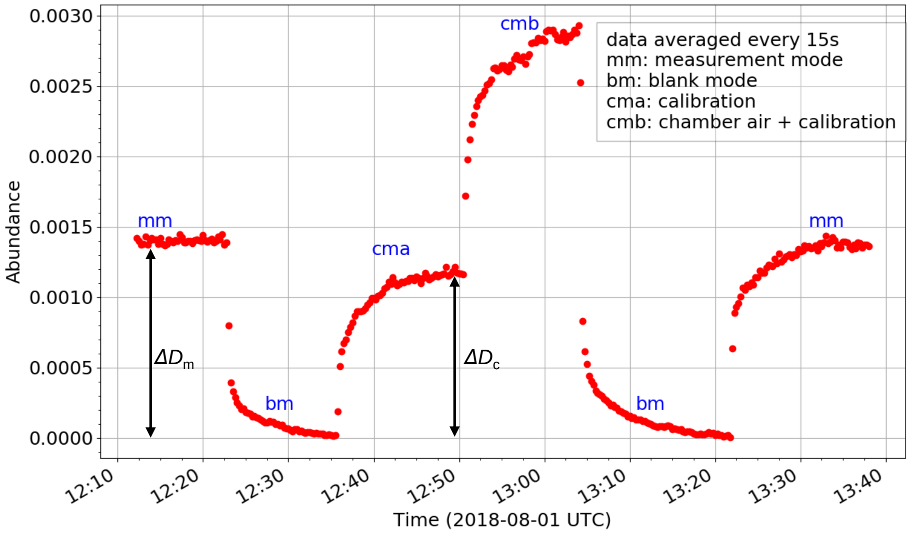

Figure 2.12: An example of the online calibration cycle taken from August 01, 2018. The abundance refers to the normalized signal relative to the CO_3^- ions.

measuring period.

$$\frac{\Delta D_c}{\Delta D_m} = \frac{[A_c]}{[A_m]} \tag{2.7}$$

$$[A_m] = \frac{\Delta D_m}{\Delta D_c}[A_c] \tag{2.8}$$

Chapter 3

In-situ measurements with FunMass in the UTLS

In order to conduct the first airborne in-situ measurements of trace gases, particles, and clouds within the UTLS above the Asian Monsoon region, a payload of 26 instruments aboard the high-altitude research aircraft M55-Geophysica was deployed during the StratoClim aircraft field campaign in the high monsoon season during the time period of July 16 – August 14, 2017 from Kathmandu, Nepal. StratoClim is an integrated research project funded by the European commission, aiming to improve the representation of chemical and dynamical processes affecting ozone and climate within Chemistry-Climate Models. In particularly, the Asian Summer Monsoon (ASM) region, which is the globally most active input region of polluted boundary layer air from the troposphere into the UTLS via the AMA, has never been studied by spatially highly resolved aircraft measurements before. Therefore, StratoClim provides highly relevant data to test and improve global models.

M55-Geophysica shown in Fig. 3.1 has been successfully adopted within European projects in many campaigns all around the globe to study problems such as Arctic stratospheric ozone loss [52] and tropical convection [17]. It is one of a few stratospheric research aircraft worldwide.

FunMass was deployed in the left wing pod of the aircraft in order to measure SO_2, HNO_3 and HCN during the field campaign. Considering the extreme ambient conditions throughout flights (rather dramatic changes in temperature, pressure and humidity), space and weight constraints on the aircraft as well as vibrations along flights, it is, however, very challenging to operate sophisticated and highly sensitive instruments onboard and perform reliable measurements. This chapter will provide an overview of the FunMass deployment during StratoClim.

3.1 The FunMass aircraft inlet system

FunMass was mounted in the left wing pod of the aircraft, which is pointed out in Fig. 3.1. The wing pod can house a instrument at the length of 2 m with an ID of 60 cm and a total mass of up to 200 kg. The wing pod was initially designed for the halogen oxide instrument (HALOX) of IEK-7 and the front of the pod is a primary inlet (ID = 40 cm), which reduces the air flow speed inside the inlet from the aircraft speed of 200 m/s down to about 40 m/s by a vertical inner plate about 75 cm downstream. The flow is diverted from the plate to a bypass along the lower half of the wing pod to run out at the rear end of the pod. The front part of the inlet is shown in Fig. 3.2. A bent tube (ID = 20 mm, 35 cm long) is attached onto the exterior surface of the vertical plate in the front of the wing pod. Its opening is oriented backward of the flight direction so that only gases and small particles can pass through the tube. Right behind the tube is the secondary inlet of FunMass, which sucks in air from the centre of the flow coming out of the tube and introduces it to the ion-molecule reaction region in FunMass. Fluid dynamics

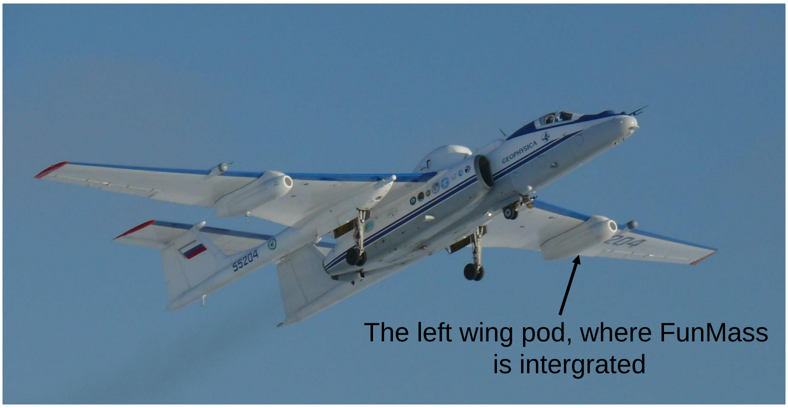

Figure 3.1: FunMass on board of M55-Geophysica

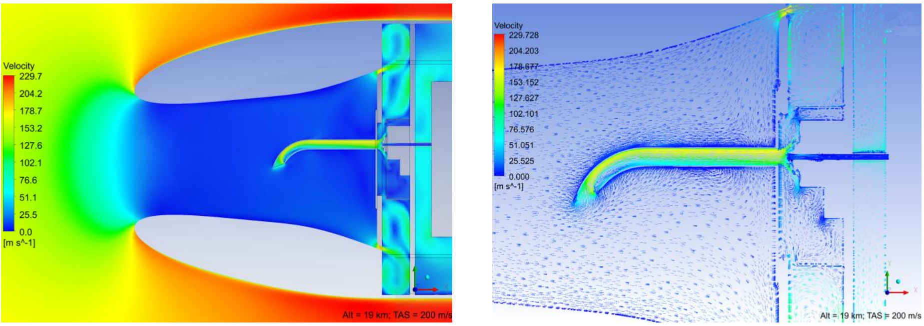

Figure 3.2: Left: The velocity of air around the wing pod during flights. Right: The velocity and direction of the air flow through the inlet. The simulation and plots are provided by Armin Afchine from IEK-7.

simulations of the setup have been carried out by A. Afchine at IEK-7 as is shown in Figure. 3.2. The simulation in the figure illustrates the velocity gradient in the wing pod ensures that the primary inlet takes in exterior ambient air rather than the air in the wing pod and then conveys it to the secondary inlet with minimum wall contact.

The secondary inlet can be switched on/off by a Python control and data acquisition program during flights. More technical details about the secondary inlet and the control program can be found in Khattatov [64]. The mechanism of the secondary inlet during flights is briefly introduced here. The inlet was heated to 60 °C to prevent H_2O vapour condensation and reduce HNO_3 adsorption on the wall despite that the inner surface of the tube is coated with Silconert-2000. The trigger to set the inlet open or close was ambient pressure. If ambient pressure was lower than 200 hPa, about 12 km in geometric altitude (z, all further altitudes without specifications will be given in z), the secondary inlet was switched open to start ambient air measurements. Otherwise, the secondary inlet remained closed. The sampled air flow was regulated by the secondary inlet to keep the IMR pressure constant at a preset value, which obviously is a critical parameter for the conversion of analyte molecules to ions or ion clusters through reactions with the CO_3^- reagent ion produced from the standard-DBD IS and therefore is critical for the calibration. The pressure in the IF makes an significant difference in the transfer process considering ion collisions and reactions. Besides, laboratory experiments revealed the optimal pressure for CO_3^--initiated chemical ionisation in the IMR is $\sim$ 30 hPa. This value allows an intake of $\sim$ 1.5 slm by the secondary inlet, which is monitored downstream by a flow meter that is used to detect the sum of analyte, IS, and sheath gas flows subtracted by the flow into ion transfer stages ($\sim$ 100 sccm).

3.2 Flight planning

Airborne measurements enable detailed probing of dynamical and chemical processes in the UTLS during the ASM by chasing after certain atmospheric features which are predicted from dedicated model simulations. For the StratoClim campaign a devoted flight planning team gathered forecasts from different Lagrangian and Eulerian models including parametrizations for convective events or not. Near real-time satellite data from the Aura-MLS instrument [73] were available. All these data could be displayed in the dedicated flight planning tool — the so-called mission support system (MSS) [115] in order to optimize flight routines plans well before actual flights.

In total, eight flights were planned and carried out during StratoClim utilizing the given meteorological conditions to explore the major scientific objectives. Flights generally lasted 3 – 4.5 hours and mainly sampled the layer between 12 and 20 km extending from the upper troposphere (UT) to the lower stratosphere (LS) in and above the AMA.

FunMass was in active measurement mode during the first seven campaign flights. However, the secondary inlet failed to switch open for the first 5 flights [64] due to a technical problem. On the last flight a failure of the turbopump led to a shut-down of the mass spectrometer, so no data were acquired (more details see the thesis of Khattatov [64]). As a result, ambient measurements by FunMass can only be reported for flight 6 on Aug. 6, 2017 (F6) and flight 7 on Aug. 8, 2017 (F7). The detailed flight conditions and objectives are described below.

F6 was dedicated to obtain the horizontal structure of the tropopause in the AMA. The aircraft took off at around 7:25 (local time) and flew a round trip in the numeric sequence over North India and South Bangladesh, as is shown in Fig. 3.3a with x_CO at the potential temperature level of 370 K (Θ = 370 K). The background CO field was calculated by the Chemical Lagrangian Model of the Stratosphere (CLaMS) [111, 110] driven by ERA-Interim reanalysis [110, 24], which is provided by the European Centre of Medium-Range Weather Forecasts (ECMWF). The CO distribution was initialized on July 1, 2017 at 500 hPa (z = $\sim$ 6 km) using the atmospheric infrared sounder (AIRS) measurements [157].

CO is a surface origin tracer mainly emitted in different kinds of combustion processes. The average profile of CO is 120 ppb near the surface, decreasing mixing ratio with height to 80 ppb just below the tropopause [29, 157] and around 20 ppb in the LS [20]. CO has an average lifetime of $\sim$ 2 months in the lower atmosphere [100] due to its reaction with OH radicals, which together with its vertical gradient makes it a good indicator for convective processes.

To study the horizontal structure of the tropopause layer, the aircraft stayed at a constant flight level ($\sim$17 km) most of the time, as is suggested in Fig. 3.3c. Simulated injections of CO from the troposphere into the tropopause layer were obvious for some parts of the flight track. Hence, F6 provides a good opportunity to study convective influences on trace gases in the AMA.

F7 was planned to survey the vertical structure of the UTLS during the ASM. The flight started at around 3:41 (local time) and flew over the northern part of India, as is shown in Fig. 3.3b. This flight covered a larger vertical span from 12 km to 19 km and was carried out with more steps and dives to better resolve the vertical structure of the AMA and the LS above it, see Fig. 3.3d. There were no evident simulated signatures of CO injection into higher altitudes

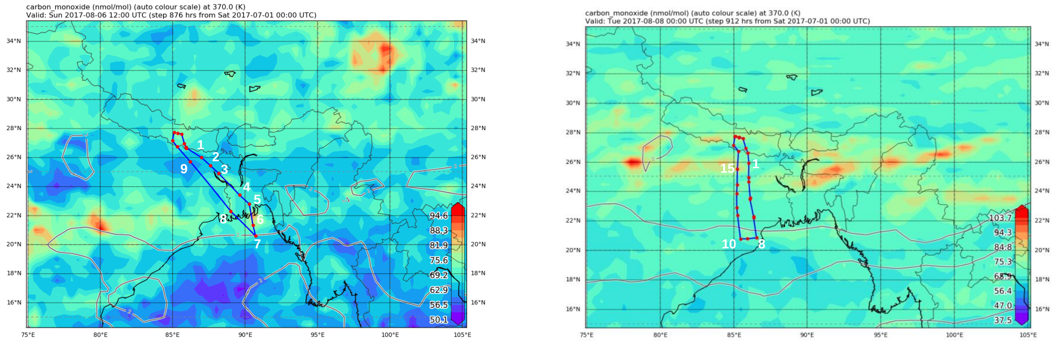

(a) CLaMS CO at Θ = 370 K in F6

(b) CLaMS CO at Θ = 370 K in F7.

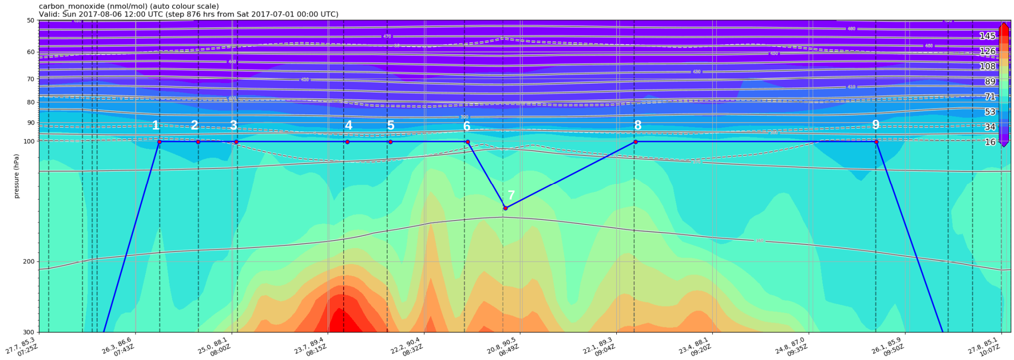

(c) CO vertical distribution along F6 from 300 – 50 hPa

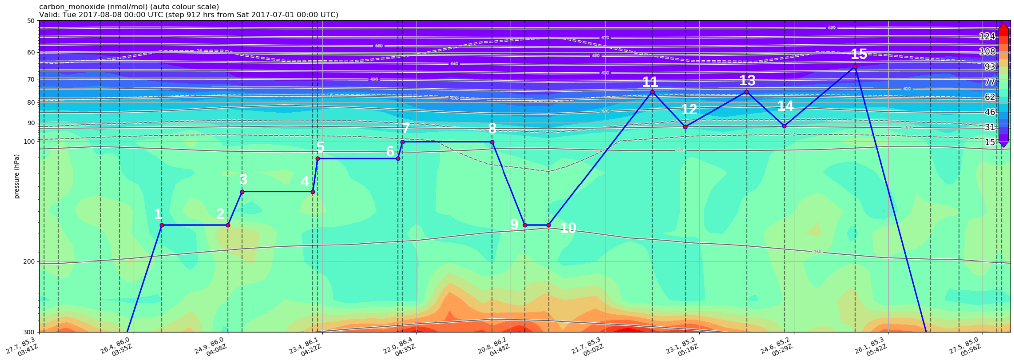

(d) CO vertical distribution along F7 from 300 – 50 hPa

Figure 3.3: Horizontal and vertical CO mixing ratio along the flight paths (blue lines) of F6 and F7. x_CO are modelled with CLaMS initialized using AIRS measurements at 500 hPa on July 1, 2017. The white numbers starting from 1 in the plots mark the numeric sequential track of the aircraft when sampling in the UTLS.

above 200 hPa in comparison to F6 except for some enhancements of CO in small regions, which might stem from convective events that happened some days earlier.

3.3 In-situ data interpretation

3.3.1 In situ HNO_3 and HCN data

The CO_3^--CIMS is capable of detecting species including HNO_3, HCN and SO_2 [2, 64]. A calibration unit was implemented for in-situ SO_2 measurements in the UTLS. It failed to function during ambient sampling and probably contaminated real-time atmospheric measurement in spite of proper function during ground tests right before flights (more details given by Khattatov [64]). This failure unfortunately does not allow to interpret SO_2 measurements but causes no harm to HNO_3 or HCN measurement. The determination of x_HNO_3 and x_ HCN from raw mass spectra using permeation rates from gravimetric analysis has been described in Section 2.4 in detail.

The in-situ measured profiles of HNO_3 and HCN by FunMass are summarized in Fig. 3.4. The cold-point tropopause (CPT) is extracted from in-situ temperature measurements along the flights recorded by the aircraft's avionic system. F6 was sampling outflow from convection at 17 km (Sec. 3.2), the vertical span of the FunMass sampling is, therefore, small with Θ varying only from 360 K to 380 K (reddish-yellow squares). During F7 the aircraft climbed up into the LS (Θ = 437 K), to almost the maximum flight level. Thus, a vertical profile of HNO_3 and HCN throughout the UTLS region was measured (bluish stars). The CPT height was 371 K (z = 16.8 km or 100 hPa in pressure coordinate) and 382 K (z = 18 km or 68 hPa) for F6 (blue dashed line) and F7 (red dashed line) respectively. To discuss observed features in the vertical range covered by FunMass it is sensible to introduce three layers consistent with the defined layers based on balloon measurements [15]:

- the Asian Tropopause Transition Layer (ATTL): Θ varying from 360 – 385 K covering the whole tropopause region. The thickness of the layer depends on the lower boundary where the laps rate minimum (LRM) is and the upper boundary where the CPT is. This layer has strong confinement in the AMA and is very vulnerable to convective events.
- the Confined Lower Stratosphere (CLS): Θ varying from 385 – 420 K. This layer is the part of the lower stratosphere that is still subjected to the confinement of the AMA. The upper boundary of the CLS is termed as the Top of Confinement (TOC) layer which is around 420 – 440 K. Slow ascent of air from the AMA and overshooting convection can happen in this layer.
- the Free Stratosphere (FS): the stratosphere above the TOC layer. It is not influenced by the confinement of the AMA any longer. Overshooting convection is also very unlikely to reach it.

HNO_3 is a key atmospheric inorganic acid with extreme solubility and can be found in considerable quantities in both gas and particle phases. Tropospheric x_HNO_3 vary from tens of ppt to a few ppb dependent of x_NOx and particle density [57, 58, 65, 159, 121, 71]. Lightning events additionally prompt HNO_3 formation due to large amounts of freshly produced NO_x [134, 74, 88]. A typical HNO_3 profile in the troposphere shows a slight positive gradient from the surface to the UT. From the UT to the LS HNO_3 experiences a strong increase due to less uptake by water droplets and high NO_x concentration in the stratosphere, and keeps increasing with altitude until reaching the FS [123].

In both F6 and F7 the majority of data points sampled below the tropopause reveal x_HNO_3 being less than 400 ppt. HNO_3 measured below the tropopause from F6 had much higher variabilities than that from F7, which is mainly attributed to very recent convective activities and will be further discussed in Chapter 4. An increase from $\sim$ 250 ppt at 380 K in the ATTL to $\sim$ 2.3 ppb at 437 K in the CLS was observed. Another feature is that the HNO_3 distribution shows rather low variability up to 420 K, while higher up in the TOC layer it varies in a wider range by more or less 1 ppb at the same Θ level. On one hand, this may be caused by different mixing processes in the ATTL and CLS. In-mixing dominates in the ATTL due to convective influences, while isentropic-mixing has more influence on the distribution of chemical species in the CLS and FS because of the well-stratified structure and much lower influence of convection-induced disturbance. On the other hand, the confinement of the AMA may lead to horizontally evenly distributed trace gases. The air slowly spirals up and therefore is somewhat confined horizontally in the ATTL, while in the CLS and FS long-range transport may bring in air masses from the mid-latitudes or TTL, which can show very different chemical composition [144]. Attention is drawn to the highest flight levels above 420 K where the aircraft obviously crossed a filament with higher x_HNO_3 ($\sim$ 700 ppt) while ascending from 420 K to 437 K. This filament will be discussed in details in Chapter 4.

HCN is an important tropospheric tracer of biomass burning and exhibits strong seasonal and regional variations [39, 80]. A major source of HCN is peat burning, which dominates Southeast Asia, Peninsula and Indonesia. Ocean uptake is supposed to be the major tropospheric sink of HCN, which results in a lifetime of 4 – 6 months in the troposphere and lower concentration of HCN in the boundary layer, especially in the marine boundary layer [82, 81]. In the tropical free troposphere HCN increases slightly with altitude, while in the tropical lower stratosphere HCN decreases at a higher rate corresponding to a stratospheric lifetime of around two years. The global climatology from satellite observations [70] suggested 200 – 280 ppt and 180 – 230 ppt HCN in tropical UTLS in summer and winter, respectively.

Profiles for HCN in the UTLS were also observed from F6 and F7, which are shown in the right plot of Fig. 3.4. Again, below the tropopause HCN showed a very high horizontal variability in the UT in F6 in comparison with F7, which is most likely associated with rather fresh convection. A decline of HCN by 100 ppt appeared from 360 K to 370 K, however, HCN started to increase slightly from 370 K to 380 K. Both HCN and HNO_3 profiles show similar enhancements at around 365 K (the main convective outflow level, ca. the LRM) and 380 K (ca. CPT), which indicates that at least part of the HNO_3 enhancements originating from convective events and were not just caused by lightning. The stronger enhancement of HCN at around the LRM also shows that HNO_3 was not yet produced there from its source NO_x but more likely to be elevated. A very similar signature in HCN as discussed for the F7 HNO_3 profile was observed at higher potential levels around the TOC, which does not fit the characteristics of a tropospheric origin biomass burning tracer like HCN. It calls for more efforts to analyse surface emissions, convection parametrization and back-trajectories to clarify the connection between tracer measurements and regional dynamic impacts.

3.4 FunMass measurements *vs.* satellite observations

3.4.1 EOS Aura MLS HNO_3

The Earth Observing System (EOS) Microwave Limb Sounder (MLS, https://mls.jpl.nasa.gov/index-eos-mls.php) is one of four instruments on the NASA's EOS Aura satellite, launched on July 15, 2004 [148]. MLS measures microwave thermal emission from the Earth's limb to remotely sense vertical profiles of atmospheric gases, temperature, pressure, and cloud

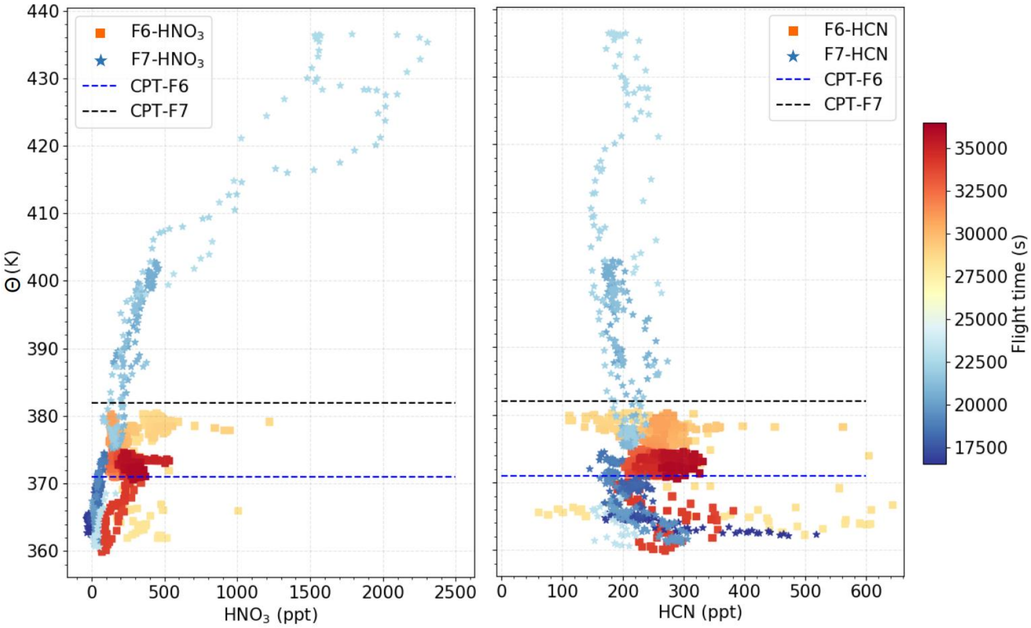

Figure 3.4: FunMass HNO_3 profiles (10 s integration) for individual flights against potential temperature with F6 in reddish-yellow squares and F7 in bluish stars. The cold point tropopause is shown in dashed line. The flight time is shown in seconds since 0:00 UTC of the respective flight day, which makes F7 appear in blueish (afternoon) and F6 in orange to reddish colours (morning).

ice water content. MLS measurements are made globally day and night from the ground to ~90 km every ~24.7 s, providing a total amount of 3500 profiles per day and latitudinal coverage from 82° S to 82° N. A feature of the MLS technique is that its measurements can be obtained regardless of the presence of ice clouds and aerosols that prevent measurements by shorter-wavelength infrared, visible and ultraviolet techniques. The global measurements provided by MLS help improve our understanding of Earth's atmosphere and global climate change [73, 59, 136].

MLS provides valuable global measurements for atmospheric trace gases, like CO, SO_2, CH_4, *etc*. The useful range of HNO_3 measurements by MLS is 215 – 3.2 hPa [123], which covers the measuring range of FunMass. The single-profile precision and accuracy for HNO_3 in the current version of MLS data (v4) are 0.6 and 1 - 2 ppb, respectively [85]. The resolution of MLS HNO_3 is 3.5 – 5.5 km vertically and 400 – 550 km horizontally. In the cross-track direction the MLS field of view (FOV) spans 3 km. Aura-MLS also produces HCN profiles above 46 hPa, which is beyond the Geophysica ceiling altitude. Therefore, in-flight HNO_3 measurements are compared with MLS HNO_3, while HCN in-situ data are compared with another satellite observation — ACE-FTS — in the following subsection.

Figure 3.5 shows an overview of HNO_3 horizontal distributions on different pressure levels in the area of 80° – 110° E , 15° – 35° N from July to August 2017, of all MLS observations falling into the flight region. HNO_3 at higher pressure levels than 178 hPa are not shown due to the fact that minor differences existed between these pressure levels. The trend that HNO_3 increases from 100 hPa to 68 hPa into the LS is very consistent between MLS and FunMass, which is

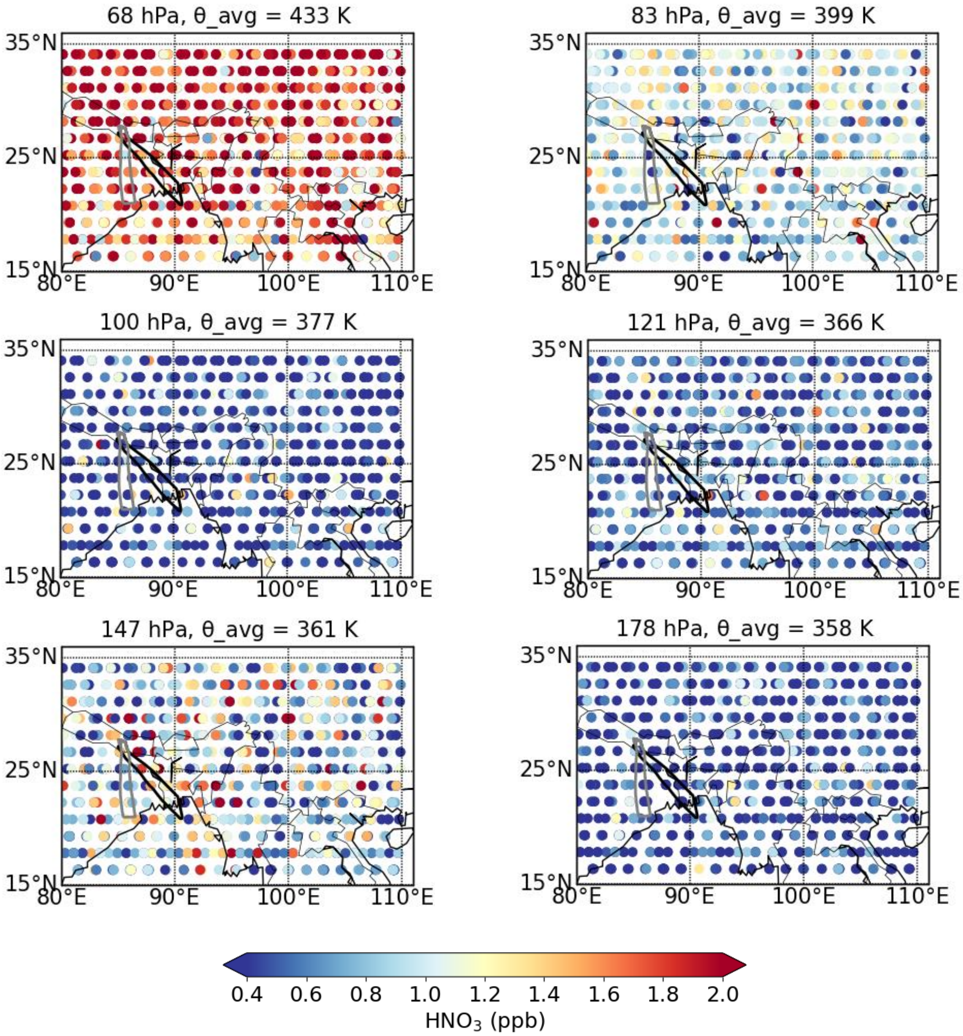

Figure 3.5: Overview of HNO3 horizontal distributions on different pressure levels of MLS from July to August 2017. Θ_avg is the mean potential temperature of all data points falling in the region at corresponding pressure level. The flight paths of F6 and F7 are in black and grey, respectively.

also shown in the vertical profiles depicted in Fig. 3.6 with pressure plotted against x_HNO_3. For the vertical profiles satellite data from more than 10 years have to be averaged in order to get reasonable standard deviations. The long-term average, however, will not reflect the interannual variability.

The in-situ HNO_3 measurements by FunMass basically agree very well with MLS observations in the UTLS, especially higher up into the LS, where the air is assumed to be more homogeneously mixed. MLS also observed quite some variability in the horizontal distribution in Fig. 3.5 with some "hot spots" at 147 hPa, especially over the Himalaya slopes, Northwest India and Bangladesh. The satellite observations are in agreement with the LRM layer (outflow layer) observed by FunMass at 360 – 365 K. The enhancements at the CPT level are not so

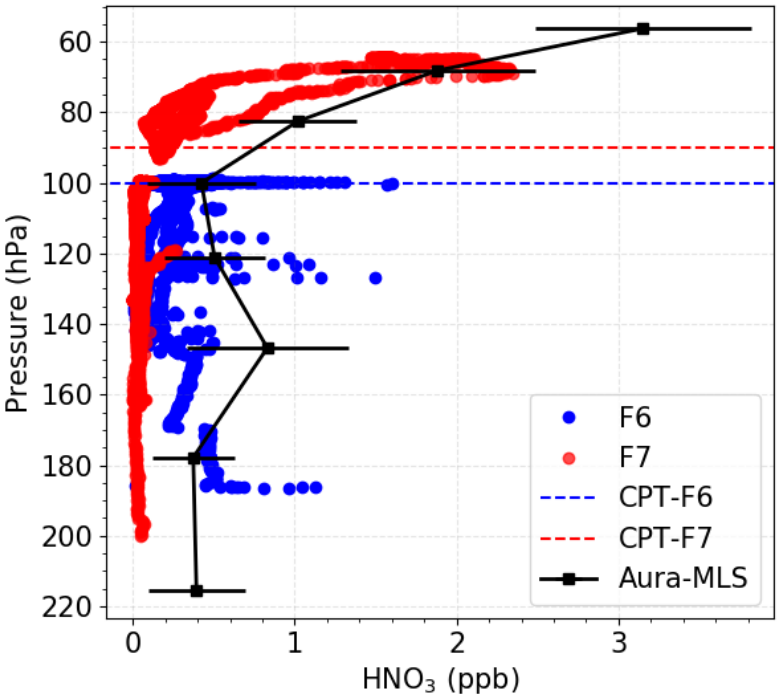

Figure 3.6: Vertical HNO_3 profiles measured by FunMass and Aura-MLS. Dashed lines show the tropopause heights. FunMass HNO_3 is integrated over 1 s. MLS HNO_3 is averaged ($\pm 1\sigma$) in the time period of July – August from 2005 to 2016 over the region 15° – 35° N, 80° – 110° E. The error bars indicate one standard deviation.

obvious in MLS at 100 hPa as FunMass observations, indicating on average convection to these levels was not so abundant in the 2017 AMA. The convection from the Indian Subcontinent potentially conveys NOx into the upper troposphere where NOx can be converted into HNO_3 on a timescale of days and HNO_3 can be lifted up into the CPT. In general very good agreement has been found between MLS observations and in-situ measurements, which is quite reassuring of both measuring techniques.

3.4.2 ACE–FTS HCN

The Atmospheric Chemistry Experiment (ACE, http://www.ace.uwaterloo.ca/instruments_acefts.php) is a satellite mission on board the Canadian satellite SCISAT, that takes measurements of the Earth's atmosphere. It is a high spectral resolution (0.02 cm^{-1}) Fourier Transform Spectrometer (FTS) operating in the mid-infrared from 2.2 to 13.3 μm (750 – 4400 cm^{-1}). ACE-FTS provides data products of temperature, pressure and trace gas profiles [70, 129, 47]. Since ACE-FTS uses the solar-occultation technique (i.e. vs. the setting and rising sun) which gives high signal-to-noise ratio, it allows highly sensitive measurements of atmospheric gas species but reduces the number of observational points per orbit to only two as compared to more than 200 for MLS. The number of measurements in regions with high cloud cover (e.g. the ASM region over India and Southeast Asia) are strongly reduced as well.

Fig. 3.7 exhibits the horizontal distribution of HCN observed by ACE-FTS from July to August 2017 at different geometric altitude levels — 12.5 km, 14.5 km, 16.5 km, 17.6 km, 18.5 km and 19.5 km — that are most relevant to the AMA. The confinement of the AMA becomes visible from 12.5 km and gains more visibility up to 17.5 km. At 14.5 km more data points indicating high HCN fall in the AMA with a difference of $\sim$ 150 ppt compared to air outside the AMA at the same latitude. The coverage of the AMA becomes more apparent at 16.5 km and its edge is clearer, even though x_HCN therein is nearly the same as that at 14.5 km. Some high HCN data points are observed at 18.5 km above the AMA, which illustrates the tropopause is not an absolute transport barrier. Similar slow tropopause-crossing transport is also observed in in-situ CO measurements [53]. At 19.5 km the air becomes very homogeneous with $\sim$ 200 ppt HCN in the tropics and subtropics due to no convective input and HCN continuously being depleted as a result of photolysis and oxidation.

HCN vertical profiles observed by FunMass and ACE-FTS data are presented in Fig. 3.8 with geometric altitude on the y-axis. In general, FunMass HCN measurements agree very well with ACE-FTS observations despite that ACE-FTS gives a slightly positive bias in the tropopause region, which may be due to HCN interannual variability. HCN measured during F6 shows higher variability below the tropopause than during F7, similar to HNO_3 measurements, and corresponds well with the ACE-FTS observations averaged over the flight region. A gradual decrease was found in in-situ HCN data only for F7 below the tropopause from 300 ppt at 13 km to 200 ppt at 17 km, which does not show up in F6. This may be a result of in-mixing of freshly uplifted air in the AMA causing more evenly distributed trace gases. Above the tropopause HCN varies from 160 ppt to 240 ppt and even exhibits an increasing trend along with altitude, which is correlated with stratospheric tracers like O_3 and HNO_3 and will be further explored in the following Chapter combining model simulations.

3.5 Tracer-tracer correlations

Tracer-tracer correlations are powerful tools for investigating atmospheric transport and mixing and separating it from atmospheric chemical processes. Such correlations, for example, are used to investigate chemical ozone loss in the Arctic [113, 94] and the extratropical tropopause transition layer [61, 54, 49]. O_3 and HNO_3 are well-known stratospheric tracers because their main sources are photochemical reactions in the stratosphere, while CO and HCN are known as tropospheric tracers given that they are mainly produced in the planetary boundary layer (in these cases by combustion processes).

Parallel in-flight CO and O_3 measurements are used to analyse the relationship between tracers in order to understand chemical transition from the UT to the LS. Here we used CO data from the airborne Cryogenically Operated Laser Diode (COLD) spectrometer at a sensitivity of a few ppb and with an accuracy of 6 – 9 % as was described in [140]. O_3 was measured with the FOZAN chemiluminescent ozonesonde instrument with an accuracy of 10 % [158]. O_3-HNO_3 and O_3-HCN correlations are, however, only available for F7 due to an instrumental failure in FOZAN during F6.

The linear correlation of O_3 to HNO_3 with O_3 < 250 ppb and HNO_3 < 400 ppt is not detailed here any longer, as it has been discussed by Khattatov [64]. However, it is shown in Fig. 3.9 that air parcels with high O_3 and HNO_3 measured in the CLS/FS in F7 may stem from the stratosphere in northern high latitudes, as the correlation coefficient (0.00407 from FunMass) of O_3 to HNO_3 with O_3 > 200 ppb and HNO_3 > 400 ppt is larger than the value determined from mid-latitude lower stratosphere and more close to the coefficient derived from ACE-FTS observations in the polar region [113].

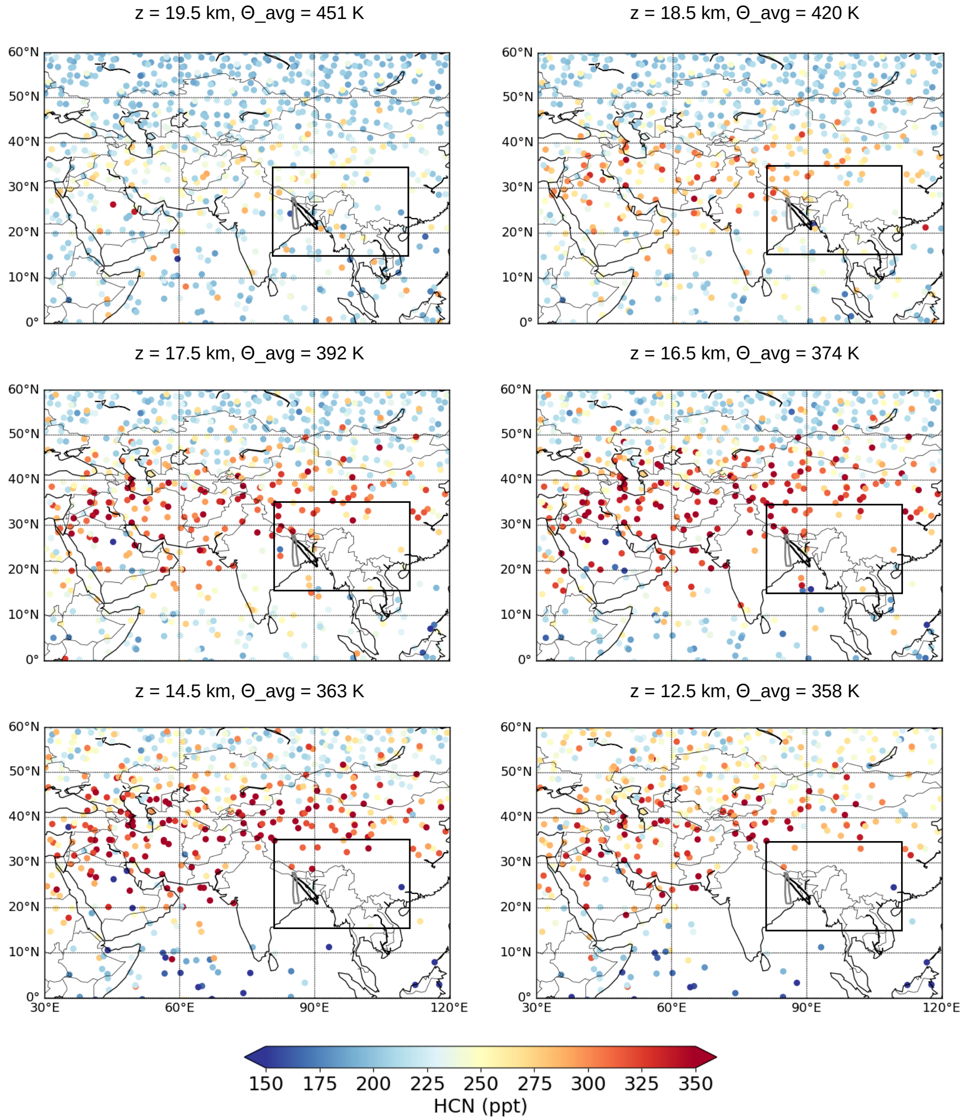

Figure 3.7: ACE-FTS HCN observations at different geometric altitudes from July to August 2017 over the region of 0° – 40° N, 30° – 120° E. The mean potential temperature Θ_avg is calculated from the temperature and pressure of data points falling into the mapped region at corresponding altitude. The flight paths of F6 and F7 are in black and grey, respectively. HCN from the black frames (15° – 35° N, 80° – 110° E) over 12 years are used to determine the mean profile of HCN in Fig. 3.8

Fig. 3.10 gives several such correlations for a number of species measured during F6 and F7 of the StratoClim campaign. A quasi ’L’-shape representing a tight anti-correlation is observed between CO and O_3, as is depicted in the upper left figure. In the ATTL ($\Theta < 420$ K), the flat part of the ’L’-shape is missing due to in-mixing processes probably caused by convective events. As O_3 formation increases with the altitude and CO is oxidized by OH radicals, an anti-correlation

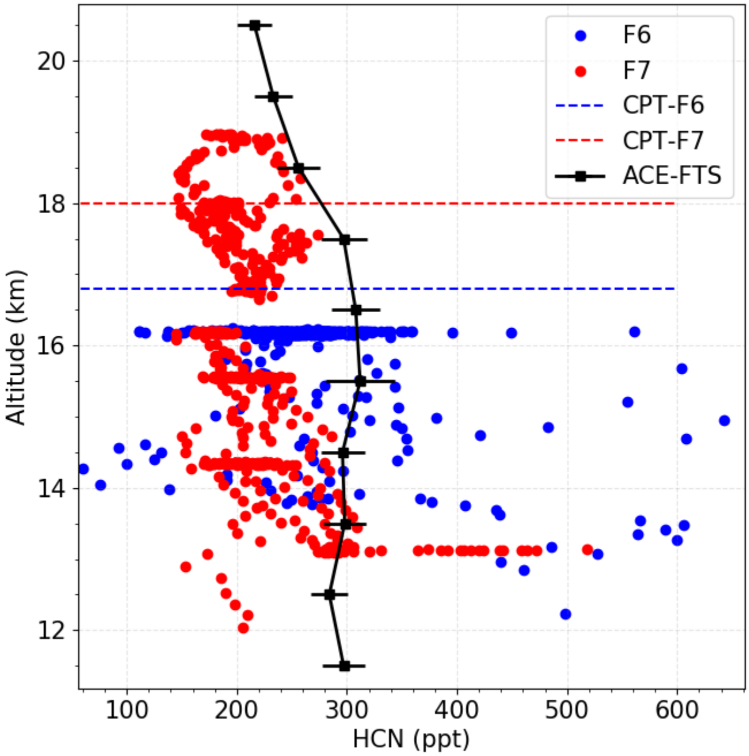

Figure 3.8: HCN Vertical profiles measured by FunMass and ACE-FTS. FunMass HCN is integrated over 10 s intervals. ACE-FTS HCN is averaged ($\pm 1\sigma$) in the time period of July – August from 2005 to 2016 over the region 15° – 35° N, 80° – 110° E. The black bars indicate the variability in the averaged ACE-FTS measurements by $\pm 1\ \sigma$

between CO and O_3 appears from the CLS towards the FS ($\Theta > 420$ K) . CO reaches a constant stratospheric background in the lower stratosphere, while O_3 steadily increases with Θ as a result of the photolysis of air.

CO-HNO_3 in the lower right figure shows similar correlation with high CO and low HNO_3 in the ATTL, low CO and HNO_3 in the CLS and increasing HNO_3 in the FS regardless of CO. However, the anti-correlation of HNO_3 with CO is not so tight as that of O_3 with CO in the ATTL (due to higher variabilities in HNO_3 in F6, see Figs. 3.6 and A.1) meaning that there is fresh HNO_3 production from NOx that has been injected by convective events or produced from lightning, while HNO_3 production in the LS results from the NOx production from N_2O photolysis.

As is shown in the upper right figure, in the ATTL where x_O_3 is below 200 ppb, HCN-O_3 correlation shows strong variability most probably due to convective influences, which is also shown in the linear correlation of HCN to CO in the lower left figure, especially in the ATTL with CO in the range of 60 – 80 and 120 – 140 ppb. The scattered linear correlation of CO with HCN in the ATTL may also indicate the different sources of CO and HCN, of which the emission

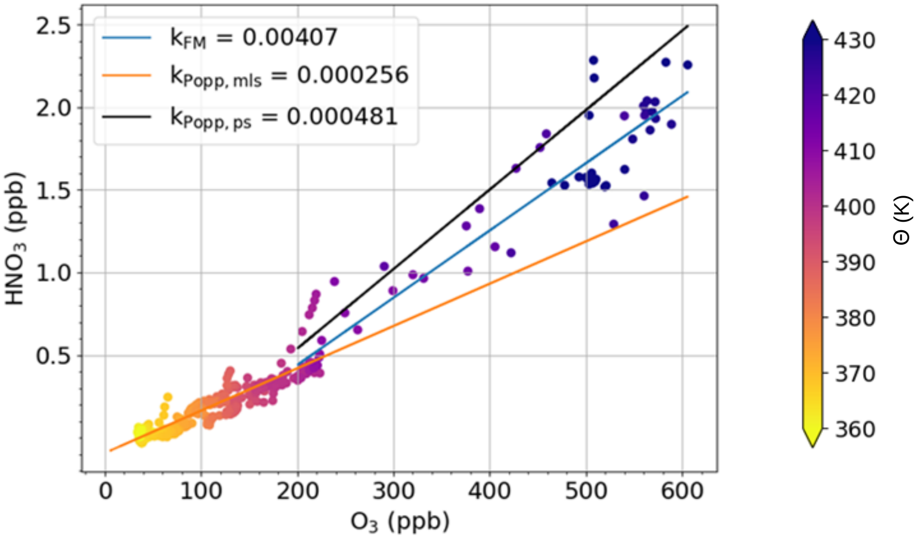

Figure 3.9: Scatter plots of O_3 to HNO_3 in F7 coloured by potential temperature (Θ) and linearly fitted by the blue line for $O_3 > 200$ ppb and $HNO_3 > 400$ ppt. The orange and black lines are the linear regression fitting for HNO_3-O_3 in mid-latitude lower stratosphere and polar stratosphere, respectively, suggested in Popp et al [113]. The corresponding linear coefficients of the three lines are shown in the legend. Note that the orange fitting includes all data points, while the blue one is drawn from $O_3 > 200$ ppb and $HNO_3 > 400$ ppt.

factors are rather different even though they both are mainly emitted from biomass burning activities [1]. Air composition above the CLS is very unlikely to be convectively influenced, therefore there is hardly any variability in HCN and HNO_3 above 420 K.

However, an unexpected linear increase of HCN with O_3 in the CLS/FS appeared in O_3-HCN, which is not in line with other tracer results such as CO. Since no convective signatures which will lead to enhanced x_CO in the CLS/FS are shown in CO measurements, the enhancement of HCN here is unlikely to be caused by overshooting convection. To understand the reason behind it, more detailed discussion will be done in Chapter 4 by analysing the origins and age of air masses in the CLS/FS.

3.6 Conclusions

In-situ measurements of HNO_3 and HCN in the UTLS were conducted with FunMass — an innovative airborne chemical ionisation time-of-flight mass spectrometer — employing the standard-DBD ion source aboard the high-altitude research aircraft M55-Geophysica in high ASM season from July 16 to August 14, 2017. During this time period, the StratoClim aircraft campaign took place in the Indian Subcontinent to investigate the atmospheric chemistry and dynamics above the notoriously heavily polluted South-East Asian region. During the campaign different numerical and Lagrangian models together with satellite observations were used to plan flight paths chasing interesting atmospheric phenomena.

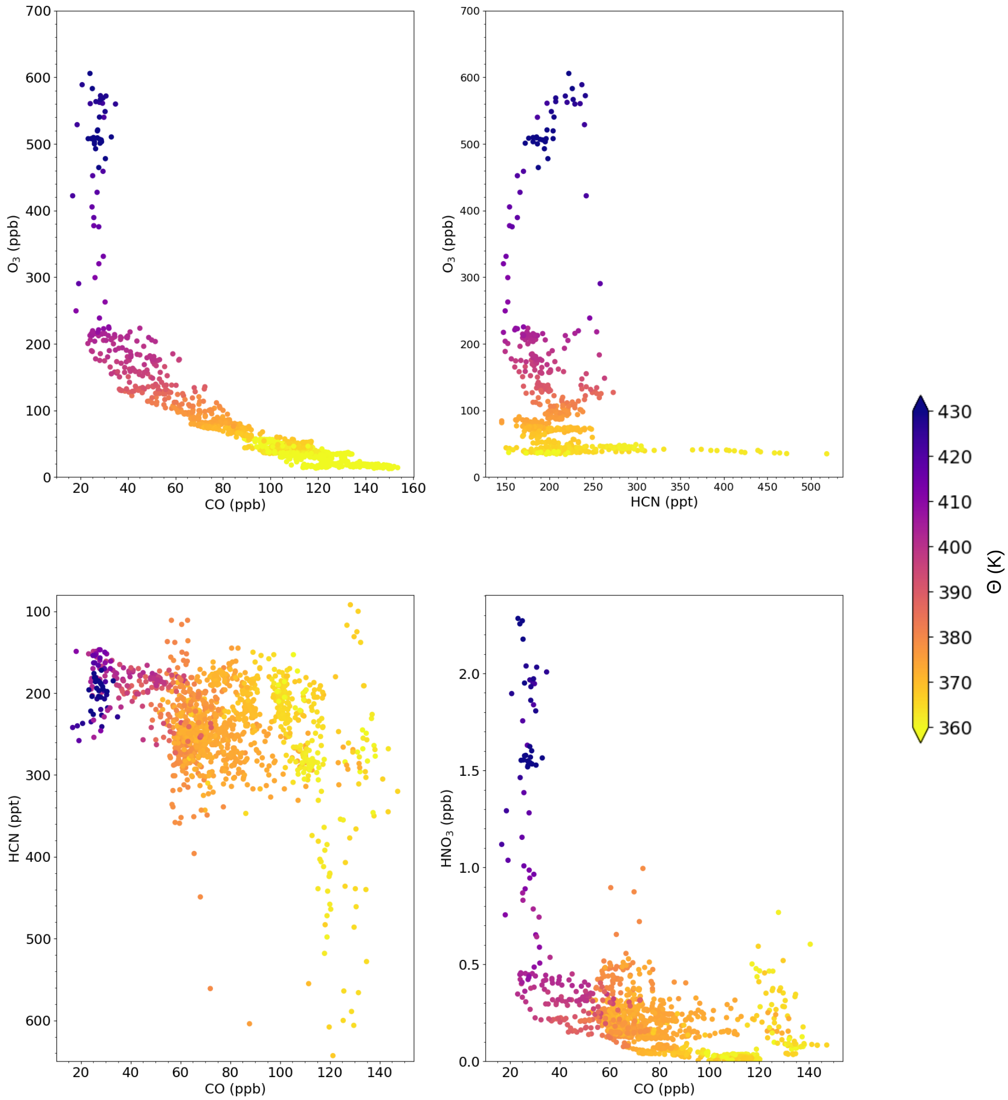

Figure 3.10: Scatter plots of CO to O$_3$, HCN to O$_3$, CO to HCN and CO to HNO$_3$ for F6 and F7 coloured by potential temperature (Θ). O$_3$ in F6 is missing due to an instrument failure in FOZAN. An "L"-shape is observed in the relationship between tropospheric and stratospheric tracers, such as CO to O$_3$, HCN to O$_3$ and HNO$_3$ to CO. A linear correlation is observed between tropospheric tracers (HCN to CO) or stratospheric tracers (HNO$_3$ to O$_3$)

.

Employing the CO_3^- ionisation scheme the detection limit of FunMass to HNO_3 and HCN integrated in 20 s is 0.8 ppt and 66 ppt respectively. FunMass measured HNO_3 and HCN successfully in two flights (F6 and F7) out of eight in total due to a failure in the secondary inlet system from F1 to F5 and in F8 when the turbopump was overheated. F6 and F7 were tuned to obtain the horizontal and vertical structure of the AMA separately. The work presented in this chapter yields several important results:

1. High-resolution vertical profiles of HNO_3 and HCN in the AMA and the lower stratosphere above it were obtained with FunMass using the CO_3^- ionisation scheme. HNO_3 exhibits a steady increase from tens of ppt in the upper troposphere to 2.3 ppb in the lower stratosphere. The x_HCN varies from 300 ppt in the upper troposphere to 200 ppt in the lower stratosphere.
2. HNO_3 and HCN show strong variability from $360\text{ K} < \Theta < 382\text{ K}$, indicating in-mixing of trace gases in the AMA caused by injection of boundary or biomass burning plumes from convection. Lightning activities may also contribute to the variability of HNO_3 in the AMA due to NO_x production from air, which is later converted into HNO_3 within days. However, a clear attribution to convective or lightning sources can not be made based on the available data.
3. FunMass HNO_3 and HCN measurements in the UTLS were compared to MLS HNO_3 and ACE-FTS HCN observations, respectively. The satellite data used for comparison are averaged within the time period of July–August from 2005 to 2016 over the region $15°$ – $35°$ N, $80°$ – $110°$ E. The high-precision vertical profiles of HNO_3 and HCN from FunMass agree rather well with the averaged satellite observations, even though ACE-FTS seems to have a slightly positive bias in the tropopause region probably resulted from interannual variabilities in the profiles.
4. Tracer-tracer correlations of HCN/HNO_3 to O_3, HCN/HNO_3 to CO were investigated to illustrate relevant chemical or physical processes causing high variability of HNO_3 and HCN in the ATTL. The ATTL between 360 K – 380 K seems to be strongly affected by direct outflow from deep convective events based on intense enhancements found in HCN and HNO_3. The HCN-CO correlation may indicate sources of the two species, which are both biomass burning products, do not match locally. CO-HNO_3 correlations imply that some enhancements in HNO_3 do have convective origin and some others could stem from lightning produced NO_x. Generally, HNO_3 and O_3 exhibit a rather tight linear correlation as expected.
5. A general slightly positive correlation between HCN and O_3/HNO_3 is found in the FS. The increasing HCN with O_3 above 420 K disobeys the characteristics of tropospheric tracers and does not appear in CO measurements, which needs further investigation employing model simulations (presented in Chapter 4) due to lacking enough measurement data for speculations based on statistics.

Chapter 4

Trajectory studies on convective influence and air mass origins

The ASM is not only impacting precipitation and climate in Asia but also transporting air pollutants emitted from the densely populated South-East Asia into the upper troposphere of the Mediterranean to the west and the Pacific to the east, see e.g. [142]. It is a globally significant meteorological phenomenon. The origins as well as the further fate of the observed air parcels, therefore, has to be studied in order to understand trace gas distributions in the AMA and the implications for ozone and climate. This can be done by employing available Lagrangian models driven by meteorological reanalysis data.

On the other hand the in-situ measured time series of gas species of tropospheric origin like CO and HCN or mostly stratospheric origin like O_3 and HNO_3 can be employed to test the consistency of the trajectory modules. This chapter presents studies comparing the observed structures of HCN to air mass origins simulated from two different Lagrangian models — CLaMS and TRACZILLA. Attention should also be paid when discussing the correlation between air mass origins and HCN features because HCN sources are not homogeneously distributed over the land mass but exhibit some variability due to biomass or biofuel burning related emission factors.

4.1 Model descriptions

During the StratoClim aircraft campaign 2017 mainly two Lagrangian models were employed to derive air mass origins and trajectories of air parcels along flight paths: the Chemical Lagrangian Model of the Stratosphere (CLaMS) [144] run by the theory group in IEK-7 and TRACZILLA [135] of the Laboratoire de Météorologie Dynamique (LMD), Paris. The model simulations and trajectory calculations were done by the responsible research groups. Herein, the model results are used to study trace gas distributions in the flight region, through which the performance of both trajectory modules can be evaluated.

The general set-up and features of the modules are introduced below.

The Chemical Lagrangian Model of the Stratosphere (CLaMS)

Three-dimensional model simulations covering the ASM season 2017 and pure backward trajectory calculations for the StratoClim flights were conducted with CLaMS. CLaMS can simulate mixing and chemistry along trajectories [90, 89, 69, 110, 143]. Meteorological fields including winds, temperature, pressure, *etc.* from ERA-Interim [24] reanalysis data provided by the ECMWF are applied to drive the model. For the vertical velocity, diabatic heating rates are used by applying the diabatic approach with contributions to vertical velocities from radiative heating including the cloud influences, latent heat release, mixing and diffusion.

For three-dimensional global CLaMS simulations, artificial tracers are released from defined regions in the Earth's boundary layer ($\sim 2 - 3$ km above the surface following orography corresponding to zenith angle ζ < 120 K). The defined regions are shown in 4.1 (a) with their full names listed in Table 4.1 and are masked as the air mass origins of the artificial tracers — "emission tracers". The vertical range of the three-dimensional global CLaMS simulations is from the surface up to Θ = 900 K (z = $\sim$ 37 km). The horizontal resolution of the simulation is 100 km and the maximum vertical resolution is around 400 m near the tropopause. The sum of all the different emission tracers in the model boundary layer including the emission tracers for the background (remaining surface) is equal to 1 at the mixing time step. The global CLaMS simulation was initialized on May 1, 2017 for the summer-fall season 2017. In the simulation, the composition of an air mass above the model boundary layer will be a combination of air released from the boundary layer after May 1, 2017 and older air originating from the free troposphere or stratosphere. More details about the three-dimensional global CLaMS simulations can be found in studies conducted by Vogel and co-workers [143, 145, 144]. In this part of the work only the air mass origins are discussed to explain the observed HCN structures.

For the pure trajectory calculations, only the advective transport is considered, totally neglecting mixing or chemistry. The back-trajectories are calculated for 40 days based on the diabatic approach and are released at the aircraft positions every second along the flight paths. They can be used to analyse the transport pathways of air parcels and possibly trace their origins.

TRACZILLA

TRACZILLA [106] is a modified version of the trajectory module FLEXPART [130]. It is used to calculate 30-day diabatic and kinematic backward trajectories. The adiabatic calculations are based on the diabatic radiative heating rates from the ERA-5 reanalyses at 20 km horizontal resolution and 1h frequency. Kinematic transport is based on the meteorological vertical wind velocity. In the vertical coordinate, the upper and lower bottom of the trajectories are 50 hPa and 300 hPa respectively. Between 70 and 200 hPa the module contains 22 standard levels so that the TTL is well resolved.

A 1000 back-trajectories cluster is released each second for flight levels above 450 hPa. This cluster of trajectories is followed back for 30 days. The trajectories from a single point are dispersed by adding a vertical diffusion which is equivalent to a random motion D = 0.1 m^{-1}/s^{-1}. The trajectories are limited in the domain of 10° W – 160° E in longitude and 0 – 50° N in latitude, see Fig. 4.1 (b) and Table 4.1 for corresponding defined region names of air mass origins. The domain encompasses perfectly with the circulation region of the AMA and its flexible edge as east-to-west eddy shedding happens. The trajectories are assumed to terminate on the following conditions: (1) hit a convective cloud; (2) exit from the lateral boundary of the domain, reach the lower 300 hPa surface, or reach the upper 50 hPa surface. In rare cases, air parcels get lost to the boundary; (3) reach the 30 days limit without exiting or hitting a cloud. Whether a parcel hits a cloud or not is judged by comparing the location of the parcel along its trajectory to the cloud top height. The cloud top temperature and height (CTTH) product [126, 25] from the geostationary satellites MSG1 and Himawari8 using the IR brightness temperature are adopted to identify main convective source regions. The time that a trajectory travels from the release to the encountering of a convective cloud is then defined as the computed age, which tells the time scale of the convective events. More detailed model descriptions about TRACZILLA can be found in the papers published by Tissier and Legras (2016) [135] and Bucci et al (2020) [16].

Both CLaMS and TRACZILLA backward trajectories are tracing air parcels back for a certain time period to their source regions. They each have their own strengths and weaknesses. Convection parametrizations implemented in TRACZILLA make it a better tool to represent deep convective events than CLaMS. However, the high lower boundary (300 hPa) in TRACZILLA cannot allow the model to capture air masses sources that may be below 300 hPa and be

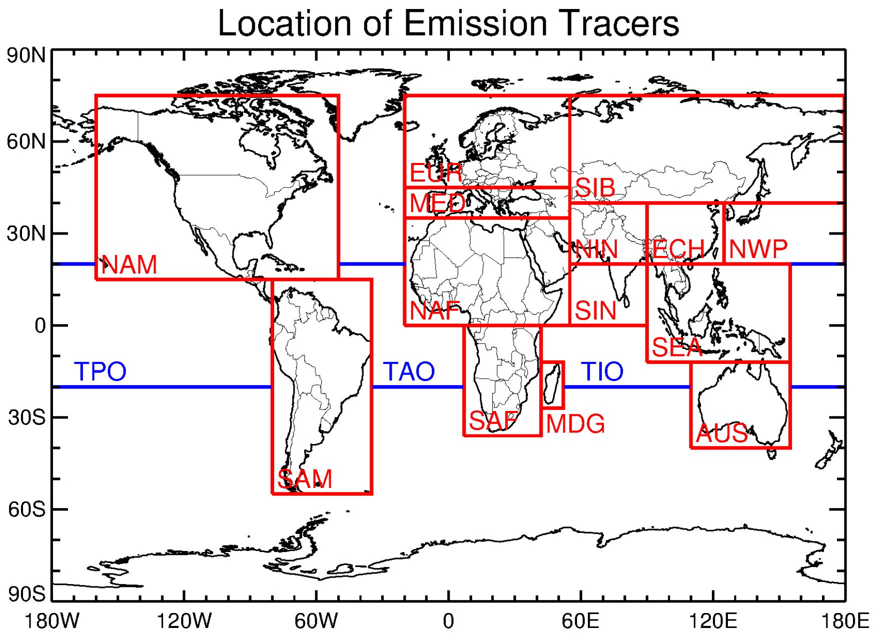

(a) CLaMS

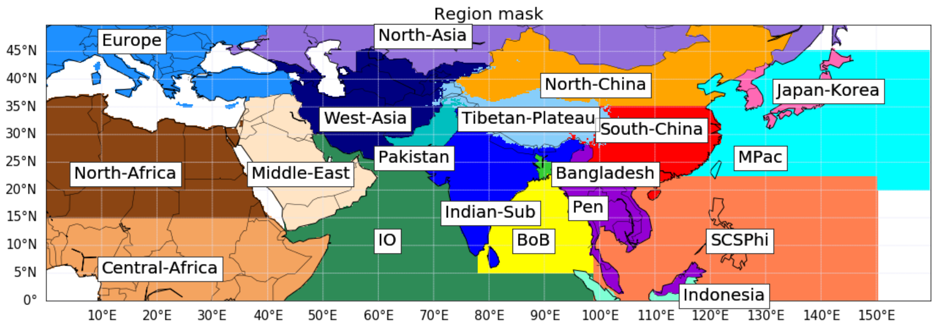

(b) TRACZILLA

Figure 4.1: Region mask of air mass origins defined in the CLaMS (a) and TRACZILLA (b) trajectory modules.

transported into or together with the clouds. As for the CLaMS trajectory module, it has a higher vertical coverage and the ability to trace back air masses into the lower troposphere. But obtaining useful information of convective events in CLaMS is difficult due to missing corresponding parametrization. By combining the two Lagrangian models, it is possible to tackle the influence of surface emissions and convective events on the air composition in the AMA.

Table 4.1: List of the short names of main source regions defined in models

	Short name	Long name	Reference[1]
CLaMS	NAM	North America	C-NAM
	TPO	Tropical Pacific Ocean	C-TPO
	SAM	South America	C-SAM
	TAO	Tropical Atlantic Ocean	C-TAO
	EUR	Europe	C-EUR
	MED	Mediterranean	C-MED
	NAF	North Africa	C-NAF
	SAF	South Africa	C-SAF
	SIB	Sibera	C-SIB
	NIN	North India	C-NIN
	SIN	South India	C-SIN
	TIO	Tropical Indian Ocean	C-TIO
	ECH	East China	C-ECH
	NWP	Northwest Pacific	C-NWP
	SEA	Southeast Asia	C-SEA
	AUS	Australia	C-AUS
	MDG	Madagascar	C-MDG
TRACZILLA	Pen	Peninsula	T-PEN
	South-China	South China	T-SCH
	Tibetan-Plateau	the Tibetan Plateau	T-TP
	Indian-Sub	the Indian Subcontinent	T-INS
	IO	Indian Ocean	T-IO
	Bob	the Bay of Bengal	T-BOB
	SCSPhi	South China Sea and Philippine	T-SCSPhi
	MPac	Middle Pacific	T-MPac

[1] 'X-ORIGIN' is used for later discussion about air mass origins for simplicity, where 'X' stands for C or T for the models CLaMS or TRACZILLA, respectively.

4.2 Convective signatures along flights

4.2.1 F6

Flight 6 was designed to investigate convective events reaching the tropopause layer, as has been pointed out in Chapter 4. Analyses on ERA5 diabatic trajectories here, which are more consistent with in-situ observations with respect to ERA-Interim and ERA5 kinematic trajectories [16], are adopted to investigate convection along the flight path. CO and HCN are shown in Fig. 4.2 as convectively influenced tracers for the discussion, considering that they are both emitted from different kinds of combustion processes in the boundary layer. The shorter life time (~ 2 months) makes CO a better tracer for convection detection with less potential interference of in-mixing or isentropic mixing.

TRACZILLA attributes the air parcel whose trajectory hits a cloud top to be convectively influenced. The black trace in the upper panel of Fig. 4.2 indicates the percentage of the dispersive 1000-trajectory cluster released every second along the flight path that hits a cloud during the 30-day simulation, abbreviated as "x_convec" later in the discussion. Θ values show the vertical coordinate of the aircraft, indicating the ambient measurement was mainly carried out in the tropopause region ($\sim 370 - 380$ K) apart from a dive to the upper troposphere.

Throughout F6 rather high convective fractions are diagnosed by TRACZILLA in line with high average HCN mixing ratios compared to F7, which has quite some lower HCN on the same levels, as has been illustrated in Fig. 3.4.

At 28.4 ks (thousand seconds) a sharp drop in x_convec appears when the aircraft ascends to 380 K, which is clearly reflected in observed x_CO and also somewhat in x_HCN (Fig. 4.2, lower panel). HCN shows a pronounced but uncorrelated dip at 28.3 ks. A quite high short-term

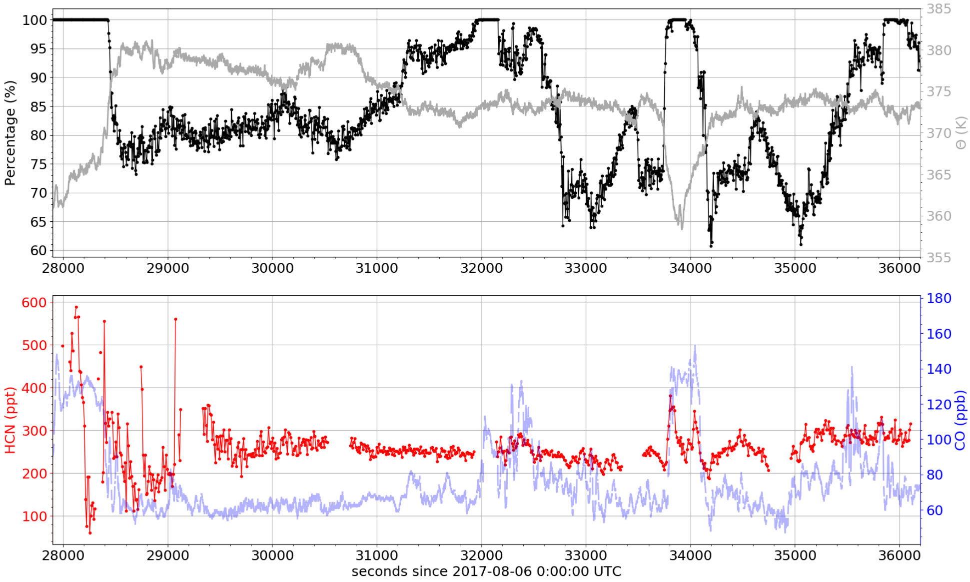

Figure 4.2: Convective fraction, x_HCN and x_CO along F6. Top: The percentage of trajectories (out of 1000) released at each second that hit a convective cloud in TRACZILLA. Flight level is given in potential temperature Θ in grey. Bottom: Time series of HCN (red) and COLD CO (blue). Note that HCN values larger than 600 ppt are not shown for a better view of the small structures.

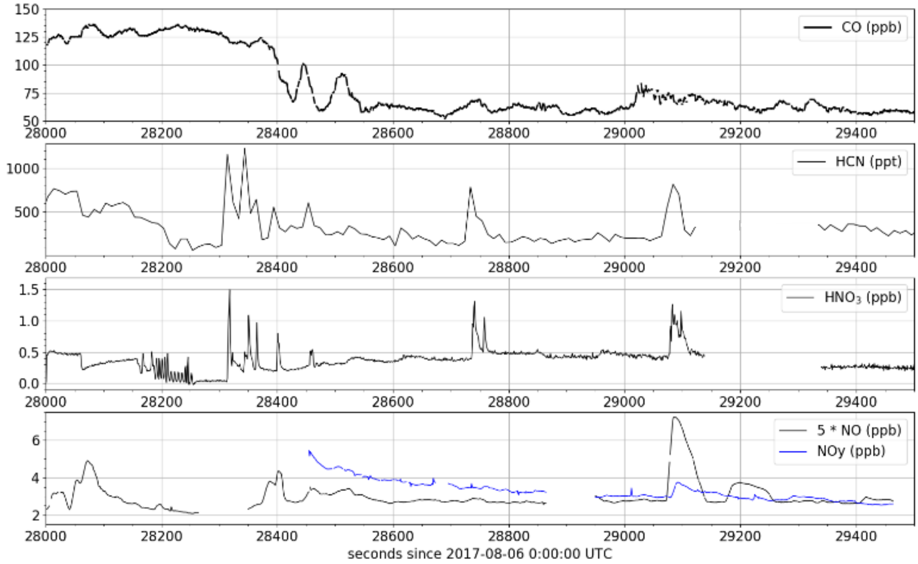

Figure 4.3: Time series of COLD CO, FunMass HCN and HNO_3, SIOUX NO and NOy between 28 – 29.5 ks for F6. The units of all species are listed in the legends. Note that x_NO is multiplied by 5 to show the structures better.

variability ("spikes" on < 50 s time scale) is especially pronounced in x_HCN and continues until about 29.2 ks. These spikes are most probably not caused by instrumental noise but due to very short convective signatures, see Fig. 4.3. Similar spikes also exist in x_CO and SIOUX (Stratospheric Observation Unit for nitrogen oXides) NO/NO_y measurements. These signatures found geographically on order of tens of kilometres obviously can not be reproduced in the model. Starting from around 29.5 ks this short term variability decreases in both HCN and CO.

Between 29.5 – 33 ks a slight decrease of x_HCN goes along with increasing convective fraction. Instrumental drift as a cause seems unlikely since the same behaviour repeats on the return leg of the flight. A possible reason is the occurrence of inhomogeneities of x_HCN in the boundary layer combined with convective uplifts of relatively HCN-poor air

During the descent of the dive between 33.8 – 34.2 ks, HCN increases by 150 ppt from 370 K down to 360 K. A slightly smaller difference appears during the ascent of the aircraft back to its original flight level. TRACZILLA suggests constantly very high convective input during this time period, which is also very well correlated with COLD CO. But x_CO does not show the same twin peak feature as HCN, which does not indicate an instrumental problem since CO and HCN, primarily being produced in biomass/biofuel burning, show quite different emission factors for different burning materials. While CO is produced with pretty constant emission factors, HCN shows an enhanced emission factors for peat burning by a factor of 10 [5], which is most common in the Peninsula and Indonesia. CO emission factors vary by a factor of 3 – 4 at most (also maximum for peat). This may indicate a shallow convective outflow layer at around 365 K with enhanced HCN source input. More details will be given in the air mass origin discussion section.

The other flight interval evidently sampling convectively influenced air parcels is 32 – 32.5 ks. The same feature appears between 35.5 – 36 ks when the aircraft flies back to Kathmandu after the dive from point 6 to 8 in the north coast of the bay of Bengal, see Fig. 3.3a. The

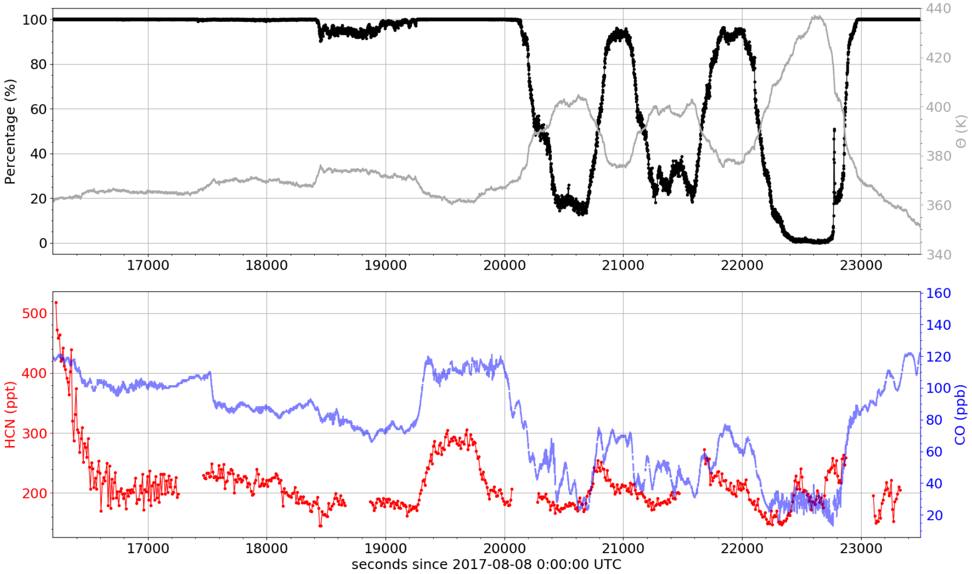

Figure 4.4: Convective fraction, x_HCN and x_CO along the flight F7, similar to Fig. 4.2.

convective features coincide with COLD CO enhancements, as is shown in the lower panel of Fig. 4.2, but do not show up in x_HCN. This may be explainable by the different source origins with varied CO and HCN abundances, of which the discussion will be followed in next section.

4.2.2 F7

The focus of flight 7 was to investigate the vertical structure and air composition in the UTLS. The CPT height detected during this flight was at $\Theta = 382$ K, being ~ 10 K higher than that during F6. There were generally no strong and fresh convective events affecting the tropopause region.

The profiles in Fig. 3.4 suggests fresh convection brings up HCN-rich tropospheric air into the AMA, which results in the patchy and on average somewhat higher profile observed in F6. x_HCN at somewhat lower levels in F7 (the shallow dive and ascent between 19.2 – 19.8 ks) show similarly high values as F6 up to more than 300 ppt. This indicates levels below the CPT up to around 370K can be strongly influenced by convective outflow. The feature is linked to the convective events in South China region which could date back 1 – 2 days, as is suggest in the Figure S6 published by Bucci and co-authors [16].

During F7, CO obviously shows a much stronger vertical gradient over the Tibet Plateau and the Indian Subcontinent with x_CO decreasing from 120 ppb to 60 ppb due to its shorter atmospheric lifetime. While the features in HCN seem to be clearly enhanced just in the outflow layer and the signatures seem to be more of a combination of convective activities and probably emission regions. Therefore, it is also of great importance to study the origins of air parcels along the flight path to better understand the small scale features in HCN.

4.3 Air mass origins

4.3.1 F6

Three-dimensional global simulations with CLaMS and diabatic back-trajectories calculations with TRACZILLA are computed to trace the origins of air parcels encountered along F6 driven by ERA-Interim and ERA5 meteorological fields, respectively. As has been illustrated in Sec. 4.1, in terms of the vertical levels of the source regions, TRACZILLA origins exhibit a more physical representation of convection between 50 – 300 hPa, while those in CLaMS go deeper down into the troposphere ($\sim$ 2 – 3 km above the Earth surface) without a convective parametrization. Figure 4.5 shows x_HCN and Θ as well as the fractions of air mass origins from CLaMS and TRACZILLA. In the discussions below, the fraction of origins of the air sample is abbreviated as 'X-origin', see Table 4.1 for the abbreviations for the corresponding origins.

The main contributing regions in the upper and lower troposphere simulated in TRACZILLA and CLaMS respectively are very similar, dominated by air masses from South China, the Indian Subcontinent, the Tibet-Plateau and Southeast Asia during F6, no matter whether convective parametrization is implemented into the model (TRACZILLA) or not (CLaMS). This agrees well with previous studies [144, 102, 38, 30, 31] on the conclusion that air masses from India, China and South-East Asia are more likely to make the AMA rich in trace gases of lower tropospheric origin.

The T-PEN (Peninsula) and C-SEA (Southeast Asia) tracers do not cause any obvious HCN enhancements during the flight, although C-SEA shows similar side peaks at the twin peak locations (33.8 and 34 ks). But the T-PEN tracer does very well correlate to the CO features at 32.5 and 36 ks. This may further imply that the emission factors of x_HCN are very unevenly distributed in the lower tropospheric emission regions [1, 5].

T-SCH (South China) and C-ECH (East China), however, consistently reproduced the enhanced HCN layer very well that is shown up as the twin peak. In addition, T-SCH also shows strong contributions to the convectively influenced CO features at 32.5 ks and 36 ks where no such obvious HCN signatures are observed, while C-ECH does not show much correlation to the CO features. This seeming inconsistency with the major sources of HCN that are suspected to be the Peninsula and Indonesia may be resolved by the boundary layer meteorology, which is not treated in either model and which may bring the air from South-East Asia into the north joining the cyclonic motion of the Asian Monsoon.

At some other locations, TRACZILLA and CLaMS simulations give different air mass origins at, e.g. 28.4 ks for the dramatic drop, 28.5 ks for the extremely high variability in x_HCN, 32 ks and 36 ks for the fresh convection features observed in CO.

The sharp drop at 28.4 ks simulated by TRACZILLA for the convection fraction and discussed in Sec. 4.2 is already attributed to convection from T-INS (India-Sub). In CLaMS this drop is not so clearly visible in any regional tracer, except that C-SEA and C-SIN (South India) show some decreases. After reaching the flight level in the tropopause region, air parcels seem to be a complex mixture of air masses from various origins instead of being exclusively influenced by convection from the Indian Subcontinent. This is quite consistent in TRACZILLA and CLaMS and for both models T-INS and C-NIN (North India) dominate the fractions.

The enhanced x_HCN observed at around 29.2 ks — unfortunately overlapped with a calibration interval — does not correspond to any of the TRACZILLA origin tracers. But C-NIN (North India) shows somewhat similar behaviour and also decreases slightly from 29.8 ks to 32 ks. This is unlikely to be caused by instrumental performance, because after the dive on the way back from 34.2 ks on a corresponding increase in HCN is observed.

The convective signatures observed in x_CO at 32 – 32.4 ks and 35.5 – 35.8 ks (Fig. 4.2) are captured by T-SCH and T-PEN, which contribute to the enhancement of CO in the tropopause

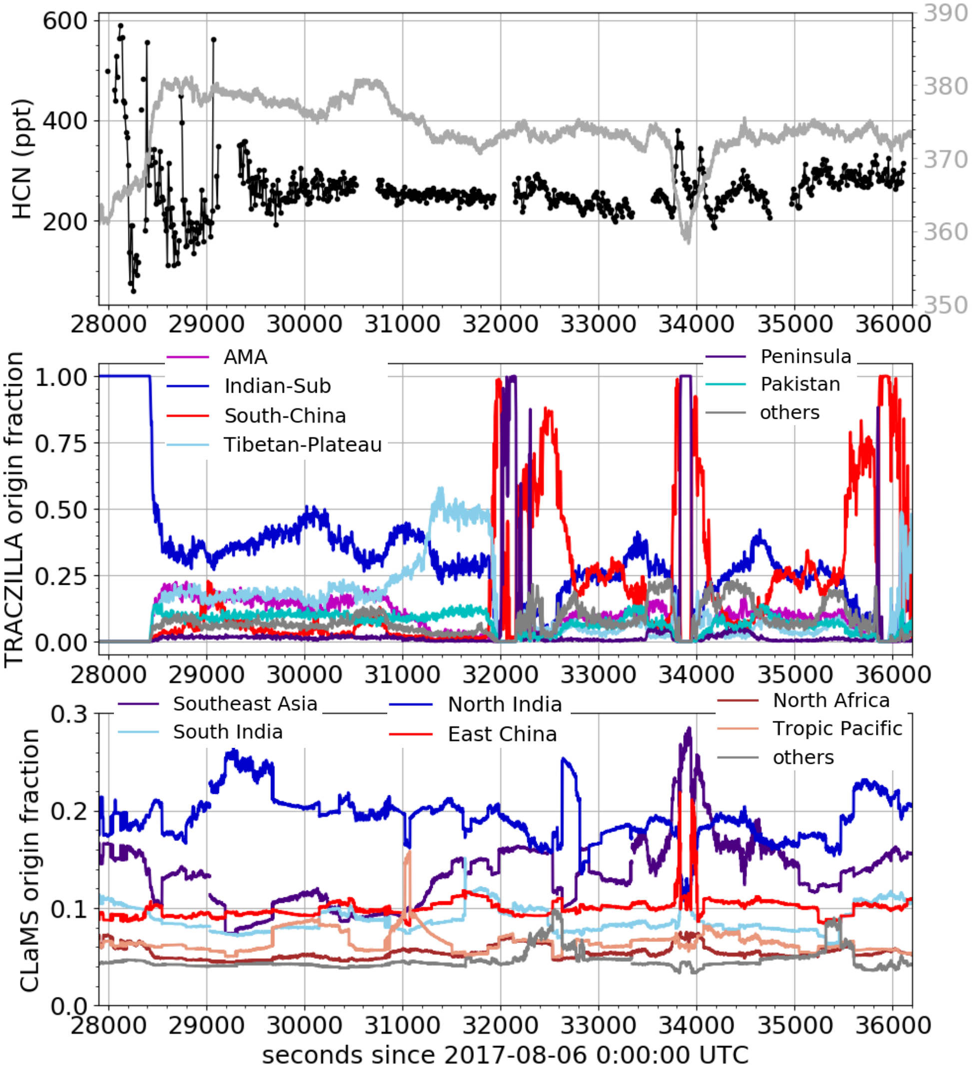

Figure 4.5: Fractions of air mass origins of air parcels along flight 6. Top: x_HCN (black) and Θ (grey). Middle: Fraction of air mass origins in TRACZILLA. Bottom: Fraction of air mass origins in CLaMS. Note that the colours used in the middle and lower panels partly represent different source regions in the middle and lower panels. The sum of minor source regions apart from the ones listed is given as "others" (grey).

region. But the peaks of CO at 32 ks and 35.8 ks fit better to the structure of T-PEN, while other peaks of CO impacted by convection are more driven by T-SCH. In CLaMS only at 32.6 and 35.4 ks C-NIN and to less extend C-SEA seem to be enhanced along with x_CO. However, CLaMS seems unable to capture the impact of this obvious convective event very well due to the missing convective parametrization. In contrary to CO, some small fluctuations alone in x_HCN appear during the two convectively influenced flight intervals at 32.4 ks and after 35 ks, but are not reproduced in the model simulaitons. Even though T-SCH shows some qualitative enhancements at these locations, the tracers mentioned above either from TRACZILLA or CLaMS do not show clear correlations to x_HCN.

4.3.2 F7

For F7, among the simulated tracers, air parcels originating from the Indian Subcontinent namely the T-TP (Tibetan-Plateau) and T-INS (or C-SIN and C-NIN) are dominating over all other air mass origins during the measuring period of FunMass, as is shown by the Figs. 4.6 and A.3. The India Subcontinent, the Tibet-Plateau and South China are found to be the three most important contributors to the simulated convective influence. The tracers from Southeast Asia and the Tropic Pacific ocean also make some minor contributions.

T-INS seems again related to the drop of x_HCN at 16.4 ks when T-INS drops to almost zero contribution. But the T-INS for this flight is not so well correlated with x_HCN as that in F6, because x_HCN already drops before T-INS decreases sharply to zero. The intense features in T-SCH and T-TP around 17 ks do not seem to be strongly reflected in x_HCN, while T-TP correlates quite well with x_HCN at least up to 19.2 ks. C-NIN shows similar decreasing trend at 18.4 ks, which is, however, delayed compared to the decrease in x_HCN and T-TP.

The simulated lower tropospheric tracers C-NIN, C-SEA and C-TPO (Tropical Pacific Ocean) are found to possibly make contributions to the enhanced x_HCN in the shallow dive between 19.2 – 19.8 ks, while TRACZILLA identifies T-TP and T-SCH as the major origins for the enhancement of $\sim$ 100 ppt HCN. However, depending on the age of the structures, namely the time of the trajectories from the release to confronting with the cloud top, a mixing down may have occurred before the measurement. Since TRACZILLA tracers indicate the mean age of the in-mixing from source regions to be less than 5 days for the main origins, the enhanced x_HCN structure could be more related to convective events from South China, the Tibet-Plateau and Southeast Asia [16], which produces similar influence on x_HCN during the dive of F6.

The first two ascents from the tropopause up to around 400 K show clearly diminished HCN and consistently low modelled tropospheric tracer fractions at the highest levels. Here good correlation of HCN exists between T-TP and T-INS (also T-Pakistan) at the two broad and structured HCN enhancements centred at 21 and 21.9 ks, which appear in between the first two excursions to 400 K and are clearly anti-correlated to the flight level. TRACZILLA and CLaMS consistently produced similar features that show qualitative correlation with x_HCN at the first two excursions (20 – 22.4 ks). These broad features are generally anti-correlated to the T-AMA tracer which represents air masses that have been circulating in the AMA when the model is initialized for backward trajectory calculations.

In addition to the broad signatures discussed above, there are two obvious shorter term enhancements in x_HCN at 20.8 and 21.6 ks, of which the latter unfortunately was obstructed by a calibration period. These signatures indicate shallow HCN enhanced layers, whihc are, however, merely obvious for the descending parts of the excursions. They might be reflected at 20.3 and 22.0 ks for the ascents, the measurements were again interrupted by the calibration period during the ascent at 20.2 ks. These slightly enhanced x_HCN signatures are not clearly shown in any of the tropospheric origin tracers but in the T-AMA tracer with some structures — enhancement at 20.8 ks and gradual increase from 21.2 to 22 ks — resemble these features.

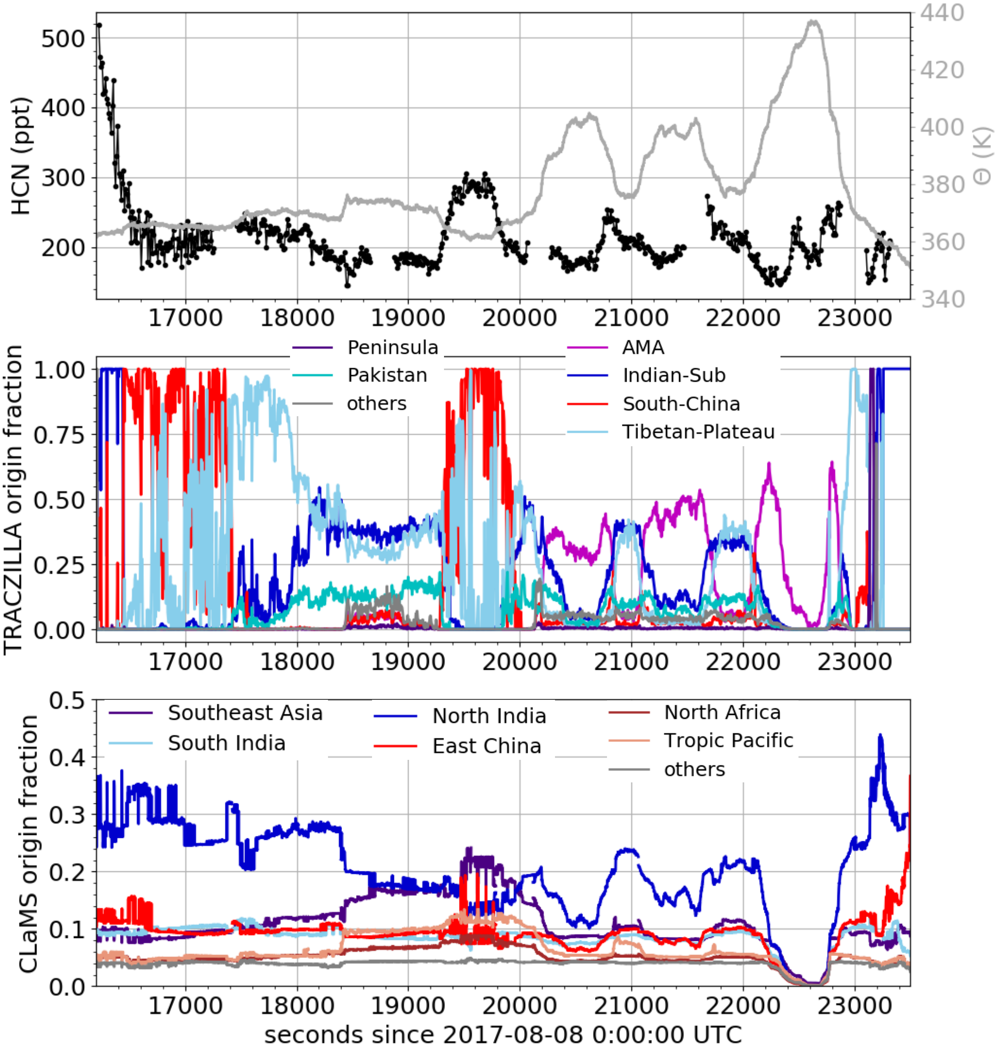

Figure 4.6: The fraction of simulated air mass origins contributing to the air parcels along the flight F7, similar to Fig. 4.5

However, they do not really seem coherent with what have happened at 22.2 ks when HCN decreases but T-AMA increases to contribute even more that it has done at 21.6 ks.

From 22.3 ks on, when the aircraft starts to climb up into the stratosphere (up to 437 K), HCN starts increasing again,nearly reaching the same concentration as that in the tropopause region. As the aircraft ascends to the highest levels, HCN decreases to an amount of 200 ppt before rising up again at the final descending part. No major influences from source regions are observed in both TRACZILLA and CLaMS simulations. To the contrary, the T-AMA origin tracer shows a feature here with two pronounced maxima at 22.2 and 22.8 ks but a strong decline from about 420 K upwards, which implies the air masses observed in between originating more from the free LS. This looks like inconsistent with the observed HCN enhancements at the first glance and intriguer more detailed discussion in the following section.

4.3.3 General features

In general, both models driven by different meteorological fields show fairly good performances and agreements in tracer simulations, whether simulating the major air mass origins from the middle to upper troposphere with convective parametrization (TRACZILLA) or from the lower troposphere without relying on the representation of convection in the meteorological fields (CLaMS). The implementation of convective parametrization makes TRACZILLA a good tool to study the convective influence on trace gas distributions. Furthermore, TRACZILLA can also simulate the transport of air in the AMA to the lower stratosphere atop of it when the AMA is included in the air mass source regions.

The major air mass origins prospected by both models in general show good correlation with FunMass HCN and COLD CO measurements, especially the tracers in TRACZILLA in terms of capturing the convective features in F6. Even the twin peak signature in HCN during the dive of F6 is well simulated in T-SCH (or C-ECH), C-SEA and T-TP, which is consistent with what the tracer simulations show for the dive during F7.

However, some smaller scale features in x_HCN are not reflected in the air mass origins, such as the unsymmetrical HCN shape at the two shoulders (20 – 22 ks) in F7 during the descent and ascent of the first two excursions into the lower stratosphere. Furthermore, the HCN enhancements from 420 – 437 K between 22.3 – 22.8 ks during the last excursion can hardly be explained by the air mass origins. In the following section, this HCN feature is further investigated using backward trajectories and the mean age of air (AOA).

4.4 Enhanced HCN in the lower stratosphere

The enhanced HCN feature observed in the LS during F7 and introduced in the previous section is depicted in the partially enlarged time series of 22 – 23 ks, see Fig. 4.7, where Θ and different tropospheric or stratospheric tracers are plotted, such as COLD CO, particle number densities by COPAS (diameter > 6 nm) and UHSAS (65 – 251 nm) as well as FOZAN O_3. HCN starts to increase at 22.3 ks, peaks at 22.45 ks and then decreases to a level at 22.55 ks. So do HNO_3 and O_3. Another peak appeared at 22.75 ks ($\sim$ 430 K) when the aircraft was descending again, indicating the encountering of two significantly different air masses in the LS above the AMA. The three-dimensional plot of HNO_3 mixing ratio during this short time period drawn Fig. 4.8, shows more clearly the structure of $\sim$ 1.7 ppb HNO_3 — the bluish white contour on top — in between two red contours of $\sim$ 2 – 2.4 ppb HNO_3, which reveals the filament of high HCN, HNO_3 and O_3 extending northward in the lower stratosphere.

Since CO, which is a tropospheric tracer with $\sim$ 2 months lifetime and whose concentration is at the stratospheric background level, does not behave the same as HCN, this feature is

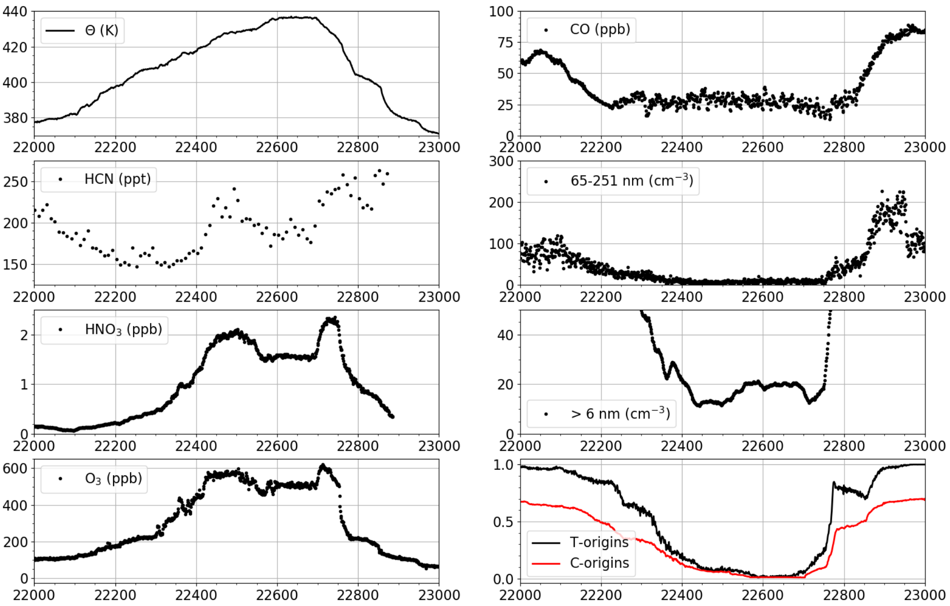

Figure 4.7: Expanded time series of Θ, HCN, HNO_3, FOZAN O_3, COLD CO, UHSAS particle number densities (65–251 nm), COPAS particle number densities (> 6nm) and total tropospheric tracer fractions simulated by TRACZILLA and CLaMS. X-axes is the time interval of the last excursion to the lower stratosphere for F7 in seconds since 2018-08-08 0:00 UTC. Y-axes are the values of the respective species with units given in the legends.

certainly not caused by fresh convection, through which HCN-rich tropospheric air is brought up into the lower stratosphere inducing an enhanced HCN layer between 420 – 437 K. This is consistent with the tracer simulations by TRACZILLA and CLaMS, which show small total fractions (< 0.1) of air masses from the troposphere, see the bottom right plot of Fig. 4.7. The pronounced filament structure could be resulted from either a filament of older HNO_3/O_3-rich air starting at around 420 K or a filament of younger air atop of it. To clarify this structure, the mean AOA has been calculated with CLaMS driven by ERA-Interim winds and using diabatic heating rates by Felix Plöger of the IEK-7 theory group based on the studies about the effect of mixing and circulation on stratospheric mean AOA [108, 107, 109]. The mean AOA of an air parcel in the stratosphere is an indicator of the average time elapsed since the air parcel has been last in contact with the well-mixed troposphere. An air parcel that has entered the stratosphere through the tropopause will steadily age without mixing. The simulated mean AOA for the last flight segment of F7 is presented in Fig. 4.9. Over the plotted time period the shape of the stratospheric tracers x_HNO_3, which resembles a Bactrian camel's back, is almost perfectly reproduced by the simulated mean age of air. The time interval in the figure corresponds to a horizontal distance of around 175 km with about 30 km between the two humps (22.55 – 22.7 ks). The mean AOA of the older air on the humps is 14 – 18 months while at the minimum in between the simulated mean AOA is around 10 months.

In order to better understand the horizontal structure over the AMA region, Figure 4.10 shows the mean AOA on 9 isentropic levels from the main convective outflow layer to around 20 km altitude. From 360 K to 390 K, the flight region of the StratoClim campaign indicated

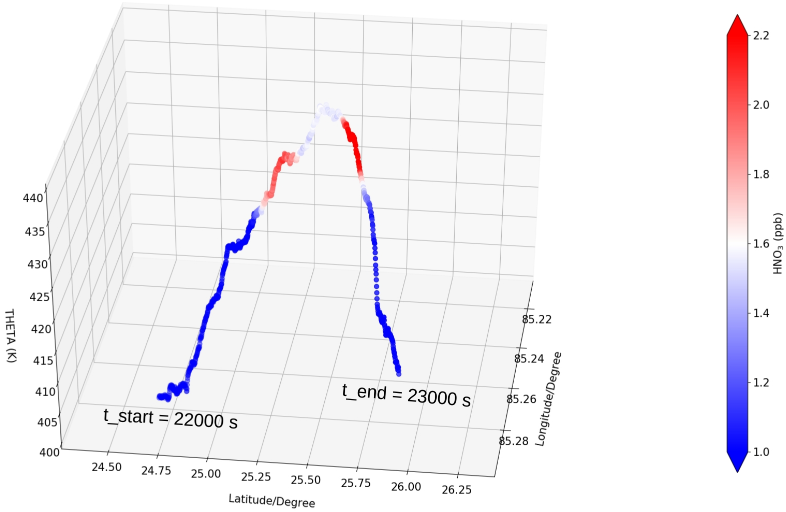

Figure 4.8: Three-dimensional view of the x_HNO$_3$ between 22 – 23 ks during F7. The red and blue contour show low to high mixing ratio of HNO$_3$ respectively.

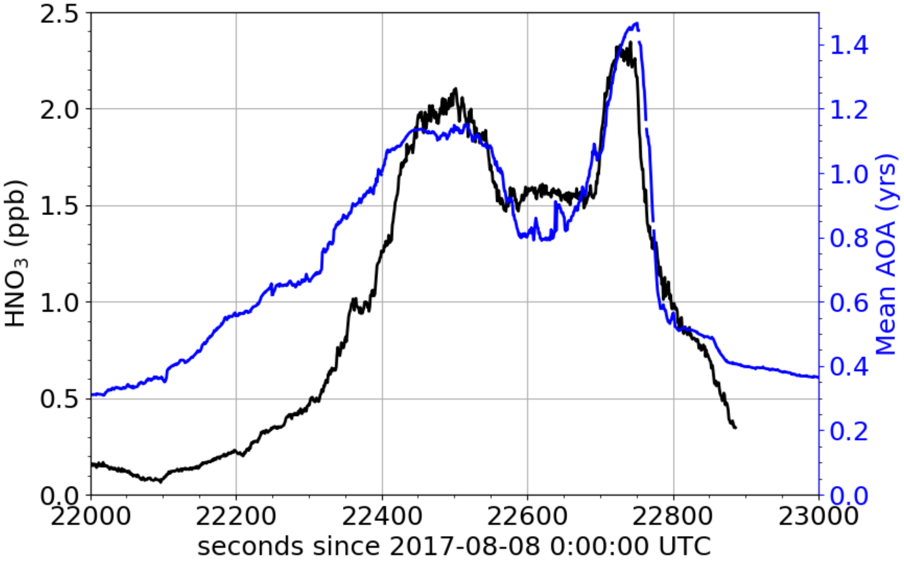

Figure 4.9: x_HNO$_3$ (black) and the mean age of air (blue) calculated by CLaMS between 22 – 23 ks.

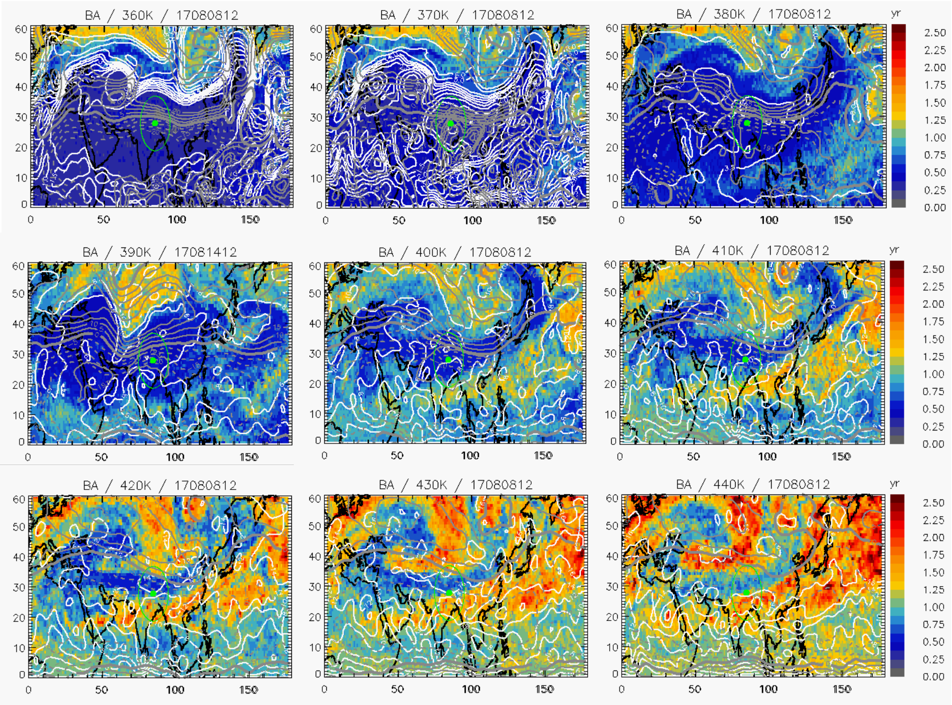

Figure 4.10: The mean AOA at different isentropic levels from 360 K to 440 K at noon time of August 8, 2017. The white and grey contours are the potential vorticity and zonal wind (solid: westerly, dashed: easterly) respectively. The green dot shows the location of Kathmandu with the green circle having a 1000 km radius.

by the green circle is exclusively composed of young air. Going up from 400 K to 410 K the confinement of the AMA is still visible but the confined area gets much smaller. At these levels on the northern and southern edge of the green circle, older air (> 1 year) starts to penetrate into the confined AMA area from the East and is drawn into the anticyclone. Above 410 K the southern part of the green circle is dominated by older air with a mean AOA of 1 – 2 years. Starting at 420 K the filament of older air has reached the observation region — the south of Kathmandu — and can explain FunMass observations on these levels.

Forty-day backward trajectories for the air parcels on the humps and in between, presented in Fig. A.2, show the transport pathways of the old air in the filament and younger air in between. However, it is difficult to trace back the primary origins of the old air due to the uncertainty in trajectories spanning a longer period of time. The particle number densities in Fig. 4.7 indicate the 4-8 months difference allows bigger particles observed using in UHSAS to completely settle out, while the small particles (> 6 nm) have settled out more (down to 10 cm^{-3}) in the "hump air" than in the valley between. During this time period, the in-situ O_3 production (around 100 ppb in 6 months) could contribute to cause the humps as well as the in-mixing of mid-latitude stratospheric air [68, 22].

The enhancement of HCN together with HNO_3 and O_3, which seems odd at the first glance, however, can be caused by the air originating from mid-latitudes or even further northwards (which can not be fixed due to missing back trajectories), a region that carried a higher load of HCN due to increased peatland burning in Indonesia as a result of the 2015-16 El Niñno and intense biomass burning in mainland Southeast Asia reported by Sheese and co-authors [128]. According to the same paper, HCN mixing ratio peaked of $\sim$ 350 – 450 ppt in the global lower stratosphere in early 2016 and was significantly larger than climatological mean and the values measured by ACE-FTS over all other years. Considering the long lifetime of (1 – 2 year) HCN in the lower stratosphere, it is possible that the stratospheric air transported to the flight path brought HNO_3, O_3 and HCN as well into the lower stratosphere and mixed with air slowly ascending from the AMA into this level to cause the observed filament feature.

4.5 Discussion and conclusions

This chapter focuses on the study of the observed structures of HCN using Lagrangian model simulations, aiming to understand the influence of convective events on HCN distribution in the Asian UTLS and to clarify the source regions of air parcels along the flight paths. The major lessons and results from this study will be summarized and discussed in the following paragraphs.

Back-trajectory simulations using two different models are adopted to explain interesting features in HCN along the flight tracks. The simulations with CLaMS are driven by ECMWF ERA-Interim meteorological fields, while the TRACZILLA simulations are driven by the latest and better temporally and spatially resolved ERA5 counterparts. The TRACZILLA trajectory module includes a parametrization for convection employing the cloud top height observed by satellites and traces air mass origins back to the upper troposphere (>300 hPa). The three-dimensional global simulation in CLaMS are releasing "emission tracers" from the lower troposphere ($\sim$ 2 – 3 km) above the Earth's surface, thereby relying on the representation of convection in ERA-Interim.

The Correlation of the convective fraction calculated from TRACZILLA back-trajectories with the observed HCN clearly indicates the overall distribution of HCN in the tropopause region is convectively influenced. However, a consistent correlation of convective fractions with HCN in the tropopause layer is not observed for all flight sections. At some locations of the flight F6 where CO reveals strong convectively influenced features that are consistent with TRACZILLA convective fractions, FunMass HCN does not show such obvious enhancements. Observed HCN during the dive in both F6 and F7 imply the existence of a convective outflow layer exhibiting significantly enhanced HCN as compared to the upper troposphere below and the CPT layer above. This structure is, however, not clearly observed in CO.

The seemingly inconsistent results for HCN and CO can be most probably explained by their different origins from the planetary boundary layer. While CO sources are more homogeneously distributed especially over the Northern Indian and Nepal regions, HCN has strong local sources in South-East Asia towards the Peninsula and Indonesia [128, 5]. Therefore, the upper troposphere is more homogeneously filled with "local" CO, while high HCN transported from the source regions in the lower troposphere in Southeast Asia sticks out when convectively injected and produces the observed enhancement in the outflow layer. However, this observation is limited to a few occasions during F6 and F7 and therefore must not be a permanent or horizontally more extended feature of the Asian Monsoon upper troposphere.

In spite of different meteorological input fields and different treatments of convection in TRACZILLA and CLaMS, both models generally show quite consistent results for air mass origins along the flight paths. Surface origin tracers simulated by CLaMS employing ERA-Interim fields suggest that tracers from the Indian Subcontinent, East China and Southeast Asia make the biggest contribution to the observed structures of HCN in the AMA for F6 and F7. Convective events in these regions prompt the transport of tropospheric air pollutants into the AMA, as is shown in the fractions of air mass origins between 50 – 300 hPa simulated with TRACZILLA.

The air mass origin study with the models provides some insights into understanding the observed general structure of HCN. However, no single specific air mass origin alone gives a consistent correlation with x_HCN during the flights. It seems that the observed structures can only be understood by a combination of several regional tracers, especially obvious from some HCN enhancements observed during the ascents/descents in F7, where the contribution of the air masses recirculating in the AMA (T-AMA) over the complete back trajectory period needs to be taken into account in addition to the lower tropospheric sources. The TRACZILLA study attributes Northern India and the Tibet Plateau to the main sources of CO observed during the StratoClim flights, but during F6 and F7, the observed CO structures are more of South China origin. CLaMS, which tracks air masses down to the lower troposphere, finds the biggest contributions from the Indian Subcontinent, East China and Southeast Asia as well to F6 and F7.

In the last segment of F7 when the aircraft was flying to the so-called top-of-confinement layer (TOC) [15] and into the free lower stratosphere, a filament of older stratospheric air but enriched in HCN was detected between 420 – 437 K with x_HCN, x_HNO_3 and x_O_3 all decreasing again at the highest flight level around 440 K. Judging from the HNO_3/O_3 correlation this filament appears to be an intrusion of stratospheric air from higher latitudes. In addition, the filament is found to tilt strongly,ascending towards the north in the vertical coordinate Θ.

To understand the filament structure in HCN, HNO_3 and O_3 any attempts employing back-trajectory analyses were unsuccessful. Nevertheless, a CLaMS simulation of the mean AOA at different isentropic levels in the ASM region driven by ERA-Interim meteorological fields and diabatic heating rates [108, 109] was compared to the observations. The mean AOA tells the air parcels with enhanced $HCN/HNO_3/O_3$ within the filament measured in ascent and descent are 4 and 8 months older than those with lower $HCN/HNO_3/O_3$ in between, respectively. This suggests the filament feature is a result of old stratospheric air rich in $HCN/HNO_3/O_3$ being (more or less) horizontally transported into the lower stratosphere at the TOC layer and then locally mixing with the younger air that rises from the AMA. A horizontal overview of the mean AOA in the ASM region from 360 K to 440 K clearly shows the filament of older air in the lower stratosphere on respective layers moving inward from the south-east edge of the anticyclone and following the anticyclonic motion. The younger air masses transported upwards within the anticyclone mix at the northern edge of the filament which is strongly tilted to the observed northern direction.

The high HCN concentration in the filament is attributed to the extraordinarily high HCN emissions as a result of the intense drought and associated peatland burning events in Indonesia in the Winter 2015 and biomass burning in Southeast Asia in the Spring 2016 driven by the strong El Niñno event in 2015-16 [32]. A massive burden of CO and particulate matters to the Indonesian and Southeast Asian troposphere was observed from satellite observations [32, 97]. The emissions were shown to have filled the mid-latitude stratosphere with high HCN until late 2016 and early 2017 [128]. However, it seems close to impossible to judge the exact origin of the observed filament due to the long transport time which prevents a meaningful backward trajectory analysis. But in this case it seems highly plausible that the old air being transported from middle or high latitudes carries higher HCN – correlated with higher O_3 and HNO_3 – than the younger air that has ascended within the anticyclone in 2017.

This filament, seeming to be an isolated feature observed "accidentally" during F7 and followed up due to its "contradictory" tracer signature, proves that air masses atop the AMA mix with air from the free lower stratosphere that are transported there horizontally, as prescribed in the ERA-Interim meteorological fields, which the mean AOA analysis computed with the CLaMS model based on lead to the same conclusion. and could be shown analysis computed with the CLaMS model. It also suggests that the view of the TOC layer at the top of the anticyclone [15] seems quite idealized. Instead, towards the TOC layer mixing happens more and more frequently with air from the free lower stratosphere that is drawn into the anticyclonic motion and mixes down the younger air that has ascended inside the AMA, and the TOC layer gets increasingly constricted extending upwards.

Chapter 5

Measurements with FunMass in a chamber study

Measurements of nitric acid and other relevant gaseous components were carried out in the outdoor atmospheric simulation chamber SAPHIR in July - August 2018, as a campaign took place to study the nocturnal chemistry of isoprene. This chapter is dedicated to describe the set-up of FunMass during this campaign and the experimental conditions. Furthermore, data are analysed and discussed on the basis of different controlled situations in the chamber.

5.1 NO_3-initiated oxidation of isoprene

The main objective of the SAPHIR chamber study is to better understand the nighttime oxidation of one of the most prominent Biogenic Volatile Organic Compounds (BVOCs) — isoprene (C_5H_8) — by the nitrate (NO_3) radical. A simplified reaction scheme of the most relevant reactions is illustrated in Fig. 5.1. The long names and structural formulas of the organic products are listed in Table 5.1 and shown in Fig. 5.2, respectively, regardless of their isomers. A by-product of the NO_3-initiated C_5H_8 reactions is HNO_3 which was measured and quantified by FunMass. Dinitrogen pentoxide, N_2O_5, is the main origin of HNO_3 under dark conditions and is formed from the reaction of NO_3 radicals with NO_2, as is shown in Figs. 1.3 and 5.1.

The reaction forming N_2O_5 is reversible with the backward decomposition rate (k_{-1} listed below) being much faster, which means that N_2O_5 is very likely to decompose once it forms. The gas-phase production rate of HNO_3 from N_2O_5 (k_2) is the sum of the second order reaction and the third order reaction [146], employing a minimum and maximum H_2O mixing ratio of 0.002 % and 2 %, respectively. While the hydrolysis of N_2O_5 is the slowest step ($k_2 \ll k_1 < k_{-1}$),

Table 5.1: Assigned organic nitrates detected by FunMass and the mass-to-charge ratios of the respective parent molecules and the detected CO_3^--cluster ions (m/z, Unit: Th)

Actual mass (m/z, Th)	Cluster (m/z, Th)	Assignment	Formula
145	205	isoprene carbonyl nitrate (ICN)	$C_5H_7NO_4$
147	207	isoprene hydroxy nitrate (IHN)	$C_5H_9NO_4$
161	221	isoprene hydroxy carbonyl nitrate (IHCN)	$C_5H_7NO_5$
163	223	isoprene nitrate peroxide (INP)	$C_5H_9NO_5$
177	237	isoprene carbonyl peroxy nitrate (ICPN)	$C_5H_7NO_6$
179	239	isoprene hydroxy peroxy nitrate (IHPN)	$C_5H_9NO_6$

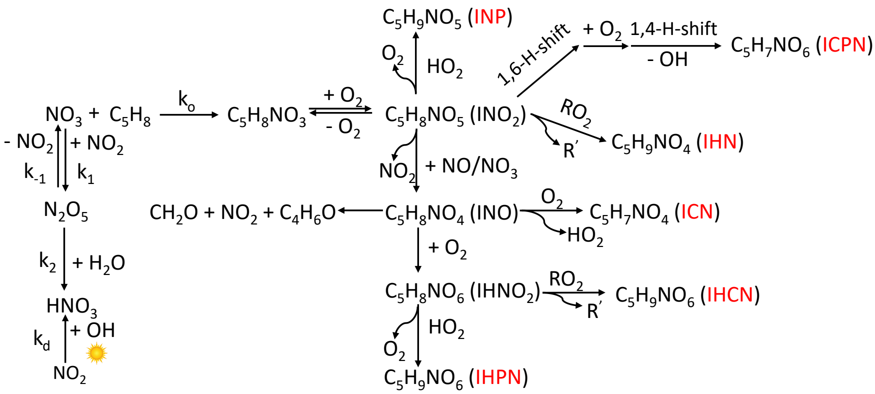

Figure 5.1: A simplified reaction scheme of C_5H_8 with NO_3 radicals. Organic products detected by FunMass are designated by their molecular formulas and their common abbreviations are in red, see Table 5.1 and Fig. 5.2 for the structural information. k_o is the reaction rate constant of C_5H_8 with NO_3 radicals. k_1 and k_{-1} are the absolute forward and backward rate coefficients for N_2O_5 respectively. k_2 is the gas-phase production rate of HNO_3. k_d stands for the rate constant of NO_2 reacting with the OH radical under daylight conditions.

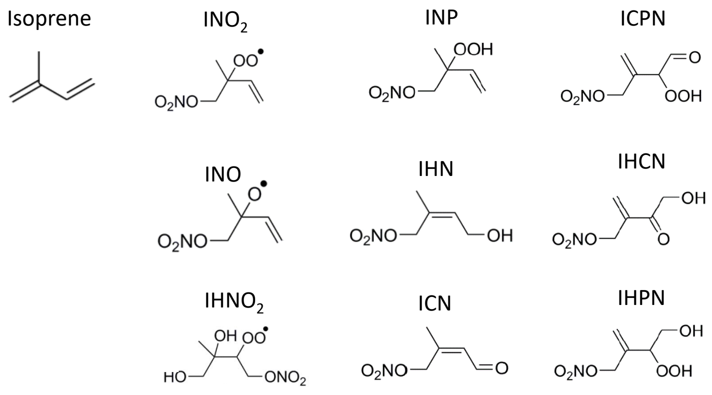

Figure 5.2: Structural formulas of the organic compounds shown in Fig. 5.1 regardless of isomers

it determines the generation of HNO_3. N_2O_5 will reach a dynamical equilibrium at some point between its formation and depletion.

$NO_3 + NO_2 \longrightarrow N_2O_5$ $k_1 = 2.2\times10^{-12}$ cm^3 molecule^{-1} s^{-1}
$N_2O_5 \longrightarrow NO_3 + NO_2$ $k_{-1} = 4.4\times10^{-2}$ s^{-1}
$N_2O_5 + H_2O \longrightarrow 2\,HNO_3$ & $N_2O_5 + 2\,H_2O \longrightarrow 2\,HNO_3 + H_2O$
$x\_H_2O = 0.002$ % $k_2 = 2.5\times10^{-22}$ cm^3 molecule^{-1} s^{-1}
$x\_H_2O = 2$ % $k_2 = 1.14\times10^{-21}$ cm^3 molecule^{-1} s^{-1}
$NO_3 + C_5H_8 \longrightarrow C_5H_8NO_3$ $k_o = 6.5\times10^{-13}$ cm^3 molecule^{-1} s^{-1}
$OH + NO_2 + M \longrightarrow HNO_3$ $k_d = 5.6\times10^{-11}$ cm^3 molecule^{-1} s^{-1}

When C_5H_8 is introduced and it continuously consumes NO_3 radicals, the equilibrium will shift to the decomposition of N_2O_5, which prevents the formation of HNO_3. During the daytime, HNO_3 is mainly formed from the reaction of NO_2 with the OH radical.

The NO_3-initiated oxidation of isoprene leads to the formation of peroxy radicals (RO_2), such as the isoprene nitrate peroxy radical (INO_2) and isoprene hydroxy nitrate peroxy radical ($IHNO_2$) drawn in Fig. 5.1. The subsequent chemistry to form the organic nitrates listed in Table 5.1, i.e. isoprene carbonyl nitrate ($C_5H_7NO_4$, ICN), isoprene hydroxy carbonyl nitrate ($C_5H_7NO_5$, IHCN), isoprene carbonyl peroxy nitrate ($C_5H_7NO_6$, ICPN), isoprene nitrate peroxide ($C_5H_9NO_5$, INP), isoprene hydroxy nitrate ($C_5H_9NO_4$, IHN) and isoprene hydroxy peroxy nitrate ($C_5H_9NO_6$, IHPN), depends on which radical, e.g. HO_2, RO_2, NO/NO_3, the RO_2 radicals react with. These organic nitrates are the major first-generation products [120, 105, 104, 99, 72, 19] and they are likely to partition into condensed liquid particles contributing to the SOA formation as a result of their low volatility. Large SOA yields (4 – 24 %) are found from the nocturnal chemistry of C_5H_8 and the condensed compounds are formed mostly from the further oxidation of these organic nitrates [99, 120]. Many studies suggested that organic nitrates formed in regions that are strongly impacted by BVOCs result in significantly high SOA production [77, 154, 11].

As the formation of HNO_3 is controlled by the concentration of NO_3, NO_2 and water vapour (x_NO_3, x_NO_2 and x_H_2O), the discussion about HNO_3 production is then based on the behaviour of NO_3, N_2O_5 and humidity in the chamber together with the competition from C_5H_8 oxidation. Two instruments using cavity ring down spectroscopy (CRDS), the CRDS-MPI (Max Plank Institute, [150]) and CRDS-ICARE (Institut de Combustion, Aérothermique, Réactivitét Environnement, [14, 12]), provided x_NO_3 and $x\_N_2O_5$ measurements. The mixing ratio of isoprene ($x\_C_5H_8$) was measured by the Proton-Transfer-Reaction Time-of-Flight mass spectrometer from Utrecht University (PTR-1000). In situations where the PTR-1000 data are questionable, the data from Vocus-PTR (Tofwerk AG/Aerodyne Research, Inc.) are used. Table 5.2 lists the specifications of the instruments that measure NO_2, NO_3, N_2O_5, O_3, H_2O and C_5H_8.

5.2 The SAPHIR chamber and FunMass sampling system

SAPHIR is an experimental platform for simulating atmospheric conditions in the research center of Jülich. The chamber has been described in detail in previous publications, e.g. [118, 149]. It consists of a double-wall FEP film, which is framed as a horizontal cylinder (length 18 m, diameter 5 m, volume 270 m^3). The chamber has a shutter system to carry out experiments in total darkness or natural sunlight. Synthetic air used in experiments is produced from liquid nitrogen and oxygen of high purity (Linde, purity > 6.0). a variety of sensitive instruments can be attached to the chamber from long sides of or underneath the chamber,

Table 5.2: Specifications of the instruments measuring species relevant to HNO_3 production

Instrument	Species	Detection limit	Sensitivity
CRDS-MPI	NO_3	a few ppt (100s)	0.5 ppt sec^{-1}
	N_2O_5	a few ppt (100s)	3.8 ppt sec^{-1}
CRDS-ICARE	NO_3	0.4 ppt (1s)	0.25 ppt sec^{-1}
	N_2O_5	2 ppt (1s)	0.9 ppt sec^{-1}
Chemiluminescence (Eco Physics)	NO_2	<0.05 ppb	-
UV absorption (Ansyco)	O_3	< 1 ppb (50s)	-
Picarro CRDS	H_2O	in ppb range	-
PTR-1000	C_5H_8	-	40 cps ppb^{-1} (Benzene)
Vocus-PTR	C_5H_8, MVK, ANs	-	10000 cps ppb^{-1} (Benzene)

mostly with instruments seated in the such containers as shown in Fig. 5.3 and implemented with different sampling lines to taking chamber air. A combination of these instruments allows for studying systems under well-defined atmospheric conditions and trace gas concentrations. SAPHIR has also proven to be a valuable tool for inter-comparisons of different measurement techniques [124, 151, 36, 26], as all instruments are assured to sample the same air composition.

A series of experiments was performed in SAPHIR from July 31 – August 24, 2018. The focus of these experiments is to investigate (by-)products from nocturnal oxidation of C_5H_8 by the NO_3 radical in the absence/presence of seed aerosols. During the chamber study, FunMass was deployed to measure HNO_3 production from simulated nighttime reactions of C_5H_8 with NO_3 radicals.


Figure 5.3: View of the SAPHIR chamber

HNO_3 is a notoriously sticky gas on surfaces. As is also pointed out in the literature [10, 98] and has been proven by tests in our own laboratory, Teflon tubes have an outstanding transmittance for HNO_3 similar to Sulfinert-treated (SilcoNert-2000, SilcoTek GmbH) tubes and superior to Dursan-treated (SilcoTek GmbH) or glass counterparts [63]. Due to its flexibility all sampling inlets and flow tubes, marked as yellow lines in Fig. 5.4, are made of Teflon. Figure 5.4 is a diagram of the sampling and online calibration set-up for chamber measurements. FunMass was placed under the SAPHIR platform and connected to the chamber with a 1.5-metre-long (OD = 6 mm) PFA tube. Around 30 cm of the tube sticks out of the floor into the chamber to sample well-mixed air. Two 3-port 3-way Teflon valves (V1 and V4) are inserted in the tube connecting the SAPHIR chamber port and FunMass inlet. They enable to switch

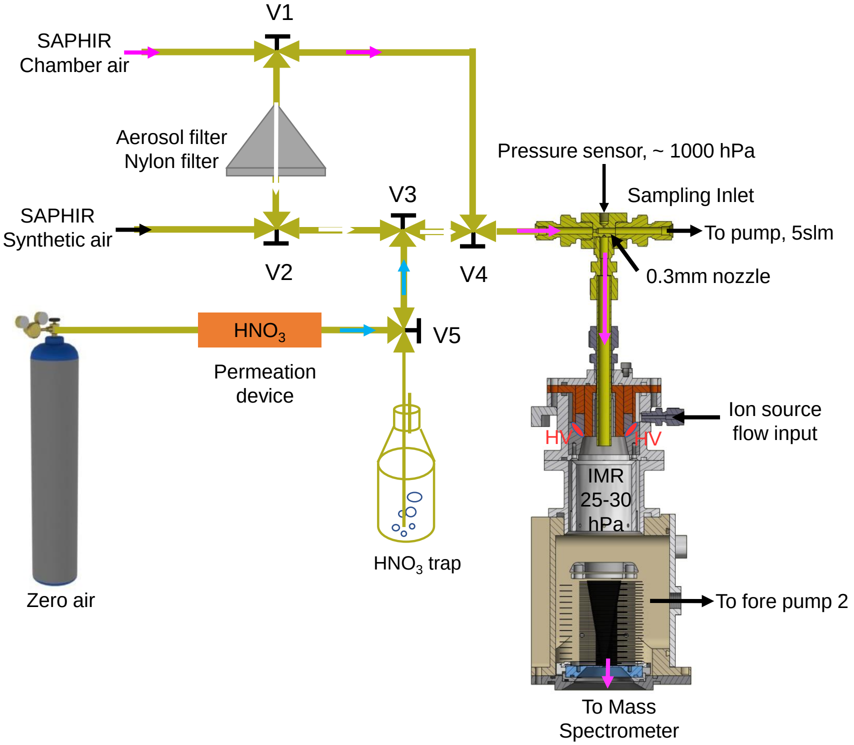

Figure 5.4: Schematic set-up of the FUNMASS sampling and calibration system for the SAPHIR chamber study. Yellow colour indicates PFA and PTFE parts. V1–V5 are 3-port-3-way valves. Purple arrows show the main flow direction, sampling chamber air (measurement mode, "mm"). White arrows means chamber air passes the aerosol and nylon filter (blank mode, "bm"). Blue arrows shows the output flow from the HNO_3 permeation oven.

measurements between chamber air sampling (the purple arrow) and online calibration (the white/blue arrow). The online calibrating procedure will be described later on.

The total sampling flow from the chamber is 5 slm generated by a scroll pump (MD8T diaphragm dry vacuum pump, Vacuubrand GmbH), which provide a fast flow (> 6 m/s) of the analyte air to the inlet nozzle. The nozzle acting as the sampling inlet of FunMass is made of PTFE and has a diameter of 0.3 mm. Approximate 600 sccm out of 5 slm chamber air is extracted into the instrument, while excessive flow is transferred to an exhaust pipe by the scroll pump. Pressure at the inlet is closely monitored using a pressure sensor to note down pressure disturbances during flow diversions. The 600 sccm analyte air keeps the ion funnel pressure in the range of 25 – 30 hPa when the IS flow of 400 sccm is added so that the ion funnel can work at its optimal performance.

The online calibration process has been briefly mentioned in Section 2.4.3. An example of one online calibration cycle on August 1, 2018 is shown in Fig. 2.12. For every experiment day at least three calibration cycles are completed. At the beginning of experiments, calibrations are used to estimate background signals. In the middle and end of experiments, calibrations are done to quantify x_HNO_3 produced from nocturnal reactions. Each calibration cycle takes around 1 hour, including blank signals from filtered chamber air (bm in short, the white arrow in Fig. 5.4), addition of HNO_3 to blank signals (cma, white arrows plus HNO_3 along the blue arrow), addition of HNO_3 to chamber flow (cmb, purple arrows plus blue arrow). The filtration consists of two filters in a row: a PTFE-filter (142 mm in diameter and 0.2-μm pore size, Sartorius Stedim Biotech S.A.) to collect particles [27, 86] in order to avoid aerosol invasion and a Nylon-filter (142 mm in diameter and 0.45-μm pore size, Pall Corporation) to scrub off HNO_3 [40, 57, 125]. Due to the stickiness of HNO_3 on surfaces, switching from one mode to another happens only when the m/z=123 signal reached a stable level. A cost of 10 minutes for HNO_3 to level is shown in Fig. 2.12 when switching between different measurement modes.

5.3 Course of the campaign

The inner pressure in the SAPHIR chamber is kept 35 Pa higher than the atmospheric pressure to prevent leaks from the real atmosphere, which causes a loss of air at the speed of $\sim$ 7 m^3 h^{-1}. A pressure regulated flow controller provides replenishment air (max. 20 m^3 h^{-1}) into the chamber, leading to a dilution effect of $\sim$ 6 % h^{-1}. Fans can be operated to ensure good mixing in the chamber, which increases wall loss of certain chemicals at the same time.

The campaign was divided into two phases. The first stage was focused on organic nitrates formation from gas-phase NO_3 radicals induced C_5H_8 oxidation, while the second stage was dedicated to study the contribution of organic nitrates to SOA formation. Fans were in operation all the time during gas phase experiments. During the aerosol phase, the high-speed fan was operated when injecting initial reactants and was replaced with the low-speed fan after the injections for good mixing. The detailed experimental conditions, such as the initial concentrations of the reactants, the H_2O mixing ratio in the chamber, the ambient temperature, *etc.*, are listed in Table 5.3 for gas-phase experiments and Table 5.4 for the aerosol phase.

During the experiments on August 1 – 4, an internal H_2O supply was switched on to add water into the IMR region through the sheath gas inlet in FunMass. The addition of H_2O enhances the formation of $CO_3^-(H_2O)$ ion clusters and meanwhile increases both the reagent CO_3^- ion and product $CO_3^-(HNO_3)$ ion signals without changing the sensitivity and the detection limit of HNO_3 [64]. Later as the humidity in the SAPHIR chamber became high enough to compensate the effects, the internal water addition was switched off. On August 3, 6, 12, 16 and 18, daytime and nighttime experiments were combined to explore the photochemistry of the intermediates and products from the NO_3-C_5H_8 reaction. To promote reactions between peroxy radicals, mainly the RO_2-HO_2 reaction, the hydroperoxyl radical HO_2 was produced from the ozonolysis of propene (C_3H_6) in the experiments on August 7, 9 and 21.

In the second stage of the campaign, some changes were also made on seed aerosols to have a deeper insight into the role that primary aerosols play in SOA formation. For example, the ozonolysis of β-caryophylene was initiated at the beginning of the experiment on August 18 and 20 so that the $(NH_4)HSO_4$ seed particles were organically coated. N_2O_5 was used as a replacement for NO_2 and O_3 to generate NO_3 radicals on August 20. Further, some other changes were applied during the campaign, like the addition of products (acetaldehyde and methyl vinyl ketone (MVK)) and replacing C_5H_8 with real plant emissions from oak trees. Such differences from one experiment to another are all listed in Table 5.3 and 5.4 for an overview about the campaign.

Table 5.3: Initial conditions of experiments for the pure gas phase

Date	NO_2 (ppb)	O_3 (ppb)	max. C_5H_8 (ppb)	H_2O[1] (%)	Extra H_2O	max. $J(NO_2)$[2] (10^{-3} s^{-1})	CO[3] (ppb)	C_3H_6[4]	Temperature (°C)
31/7/2018	1 – 5	90 – 120	0	0	off	-	0	No	25 – 35
1/8/2018	2 – 5	85 – 115	1.5	0	on	-	0	No	22 – 31
2/8/2018	2 – 5	85 – 120	3	0	on	-	0	No	23 – 38
3/8/2018	1 – 5	45 – 100	2.1	1.3 – 2.7	on	5	0	No	30 – 42
6/8/2018	1 – 6	45 – 110	2.4	1.4	on	5	15	No	20 – 44
7/8/2018	3 – 4.5	45 – 60	1.8	0.45 – 0.6	off	-	0	No	20 – 41
8/8/2018	13 – 30	75 – 115	7	0	off	-	0	No	22 – 28
9/8/2018	2.5 – 6	65 – 115	3	0	off	-	120000	yes	20 – 27
10/8/2018	3.5 – 5	40 – 65	1.8	0	off	-	100	No	17 – 28
12/8/2018	4 – 12	70 – 115	2.3	0	off	4.8	120000	No	14 – 36
13/8/2018	12 – 23	75 – 110	7	0	off	-	0	No	18 – 24

[1] The amount of H_2O in the chamber is the percentages of water in the chamber air.

[2] The photolysis frequencies were calculated from actinic flux measured outside the chamber by a spectroradiometer applying a transfer model.

[3] CO was added as OH scavenger during daytime reactions.

[4] Propene was brought in as a HO_2 source via its ozonolysis to study the fate of peroxy radicals (RO_2) under dark conditions.

Table 5.4: Initial conditions of experiments seeded with aerosols

Date	NO_2 (ppb)	O_3 (ppb)	max. C_5H_8 (ppb)	H_2O (%)	max. J(NO_2) (10^{-3} s^{-1})	CO (ppb)	Temperature (°C)	others
14/8/2018	13 – 22	70 – 110	11	0.01	-	0	19 – 24	
15/8/2018	8 – 21	80 – 115	7	1.3 – 2.0	-	0	20 – 28	
16/8/2018	2 – 5	80 – 115	2.5	1.6	4.8	20	20 – 28	
17/8/2018	0 – 17	0 – 400	0	1.2 – 1.7	0	5	18 – 26	acetaldehyde[1]
18/8/2018	2 – 5	80 – 110	2.5	1.3 – 1.4	4.8	20	14 – 31	β-caryophylene[2]
19/8/2018	0 – 20	0 – 110	2.3	0.07	-	8	16 – 31	N_2O_5[3], MVK[1]
20/8/2018	3 – 5	85 – 130	4.5	1.2 – 1.9	-	8	20 – 26	β-caryophylene
21/8/2018	2 – 5	55 – 130	4.5	1.5 – 1.9	-	120000	20 – 30	propene[4]
22/8/2018	2.5 – 8.5	75 – 110	4	1.3 – 1.7	–	20	18 – 33	plant emissions[4]
23/8/2018	3.5 – 5	45 – 100	3	1.5 – 2.2	-	13	18 – 31	
24/8/2018	2.3 – 5.5	85 – 110	18	1 – 1.6	-	5	17 – 23	β-caryophylene, $(NH_4)HSO_4$[5]

[1] Acetaldehyde and MVK were injected in the final stage of experiments for product analysis.

[2] The ozonolysis of β-caryophylene was used to produce seed organic aerosols.

[3] N_2O_5 was used to generate NO_3 radicals replacing NO_2-O_3 mixture.

[4] Isoprene was directly emitted from oak trees.

[5] $(NH_4)HSO_4$ was added to observe the impacts of acidic seed aerosols on the formation of SOA.

The main task of FunMass during the campaign was to measure HNO_3, which is a by-product from the NO_2-O_3-C_5H_8 reactions. HNO_3 production during experiments was calibrated with the permeation device mentioned in Chapter 2 and the results will be shown in the following sections along with discussions. What is also included in this chapter is the detection of organic products by FunMass and discussions about the impacts of different factors on the measurement species.

5.4 HNO_3 production in the gas phase

5.4.1 Background HNO_3 measurements in the chamber

The first experiment took place on July 31 without C_5H_8 injected into the chamber in order to derive the production and degradation of the NO_3 radicals, particles and other inorganic species in dry and "blank" condition. As the instrument started to sample chamber air at 7:45 UTC (all time will be given in Coordinated Universal Time) with only O_3 added to the chamber, it showed a rather high background signal of around 0.4 ppb HNO_3. The blank value gradually decreased to slightly above 0.1 ppb at 9:30. As soon as NO_2 was added into the system, it underwent exponential decay with time and in the meantime a growth was synchronously observed in HNO_3. HNO_3 peaked at a value of about 0.66 ppb at 12:30 before being interrupted by the online calibration.

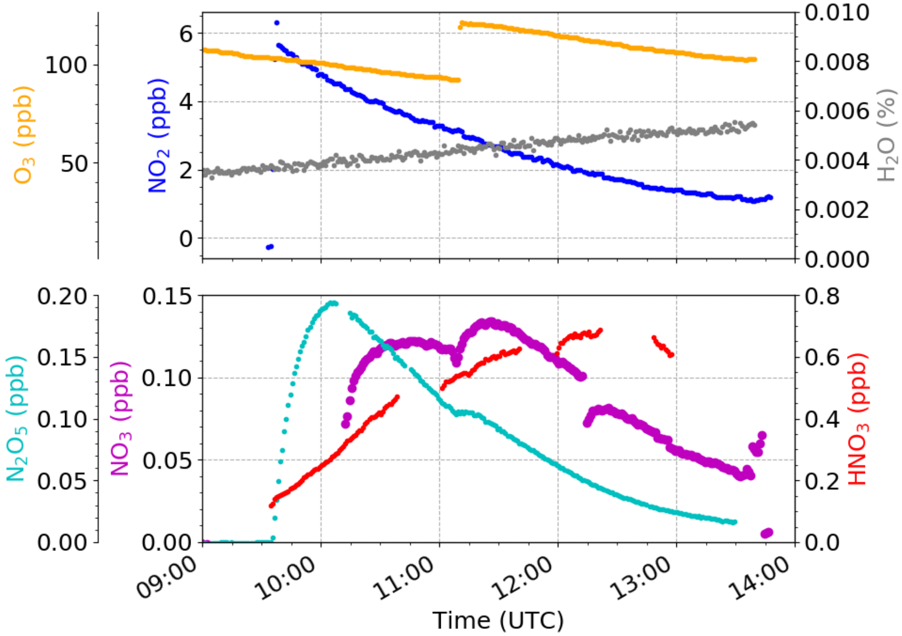

Figure 5.5: Time series of HNO_3 and relevant species on July 31, 2018. Upper panel: mixing ratios of reactants. x_O_3 and x_NO_2 in orange and blue respectively are on the left y-axis. x_H_2O is in grey on the right y-axis. Lower panel: mixing ratios of NO_3, N_2O_5 and HNO_3. NO_3 and N_2O_5 in magenta and cyan, respectively, are on the left y-axis. HNO_3 in red is on the right y-axis

After the calibration, HNO_3 shows a trend of decreasing before the consumption of NO_2 levelled out. Before the termination of the experiment, the amount of HNO_3 in the chamber was 0.6 ppb accompanied by ~ 1.2 ppb NO_2 and 105 ppb O_3. The chamber was kept under

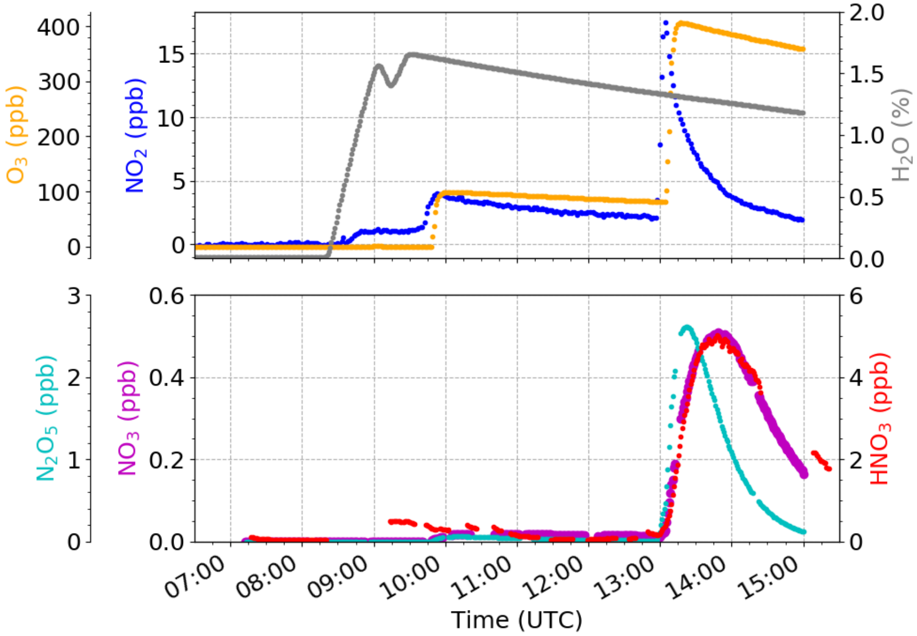

Figure 5.6: Time series of HNO_3 and relevant species on August 17, 2018, similar to Fig. 5.5.

dark and dry conditions during this experiment. The source of the initial background HNO_3 could be the chamber wall, where some acidic residuals from previous chamber experiments reacted with NO_2 and O_3, and then released HNO_3. This blank HNO_3 signal appeared in other dry experiments as well, independent of the internal water supply in FunMass. Although the chamber was flushed with synthetic air (Linde, purity 5.0) overnight before any injection of substances for initiating reactions, the interference from the chamber wall probably still existed. The Teflon wall acting as a source of nitrous acid (HONO) has been quantified before [118] and losses of NO_3 and N_2O_5 on the wall have also been determined via comparisons between kinetics simulations and measurements [35].

The other background test that was run on August 17 under humid conditions with 1.2 – 1.7 % water (milli-Q water with a resistivity of ~18 MΩ·cm) in the chamber, as is shown in Fig. 5.6). The production of HNO_3 was mainly driven by the inorganic species without C_5H_8 in the system. When NO_2 and O_3 were pushed to 18 and 400 ppb respectively, HNO_3 started to soar up at 13:00 and reached the peak within 40 minutes. Because the formation of HNO_3 is a very slow reaction, this strong peak in a short time interval seems more likely to be related to the heterogeneous reaction of N_2O_5 with H_2O involving chamber walls or particles, which has been investigated in a chamber study [147]. The decrease of HNO_3 at 14:00 was due most probably to the fast decline of NO_2, which reduced the formation of N_2O_5 — the direct source of HNO_3. It may also be a result of the settlement of HNO_3 on the chamber walls.

During the humidification process, FunMass measured around 0.4 ppb HNO_3, which may be outgased from the wall as a result of disequilibrium caused by water absorption in the chamber. As the humidification stopped at 9:15, it seems that HNO_3 reached equilibrium again and became stable before the second injection of NO_2 at 9:45. The gas-phase production of HNO_3 in the chamber was very low and was dropping from 0.4 to 0.1 ppb at 11:30 in response to the addition of 4 ppb NO_2 and 90 ppb O_3 at 9:45. The maximum likelihood is that HNO_3 dissolved into water at a faster speed because of its extremely high solubility and the high x_H_2O in the chamber which may even trigger the heterogeneous reaction of N_2O_5. Comparing this part of the experiment to the one on July 31 that was carried out under dry conditions, around 0.4 ppb gas-phase HNO_3 was lost under humid conditions, while x_NO_3 and x_N_2O_5 did not differ much. It seems that the chamber walls has taken up much more HNO_3 than under dry conditions. This should be noted when discussing the production of gas-phase HNO_3 from experiments with humidification.

5.4.2 Test with a low amount of C_5H_8 in the chamber

On August 2 the experiment was conducted under the same initial conditions as the one on July 31, except that 2.5 ppb of C_5H_8 was injected into the chamber and the internal H_2O supply in the instrument was switched on, of which the function has been mentioned in Sec. 5.3. Similar to the blank test on July 31, around 0.1 ppb background HNO_3 was measured with FunMass in the synthetic flushed chamber before the addition of NO_2 and O_3.

N_2O_5 and NO_3 started to accumulate as soon as NO_2 and O_3 were injected, peaking at 9:30 and 10:00 respectively, while the formation of gaseous HNO_3 was rather slow, reaching 1 ppb before the replenishment of NO_2 and O_3. Compared to July 31, NO_3, N_2O_5 and HNO_3 were all in a larger amount on August 2.

The re-injection of NO_2 and O_3 brought x_HNO_3 up quickly to 1.2 ppb, but HNO_3 started to go down very slowly as soon as C_5H_8 was added into the chamber at shortly after 11:00. Because the net production of NO_3 was curbed due to its consumption by C_5H_8 which led to less formation of N_2O_5, HNO_3 decreased briefly by around 0.2 ppb from 11:05 to 12:40. During

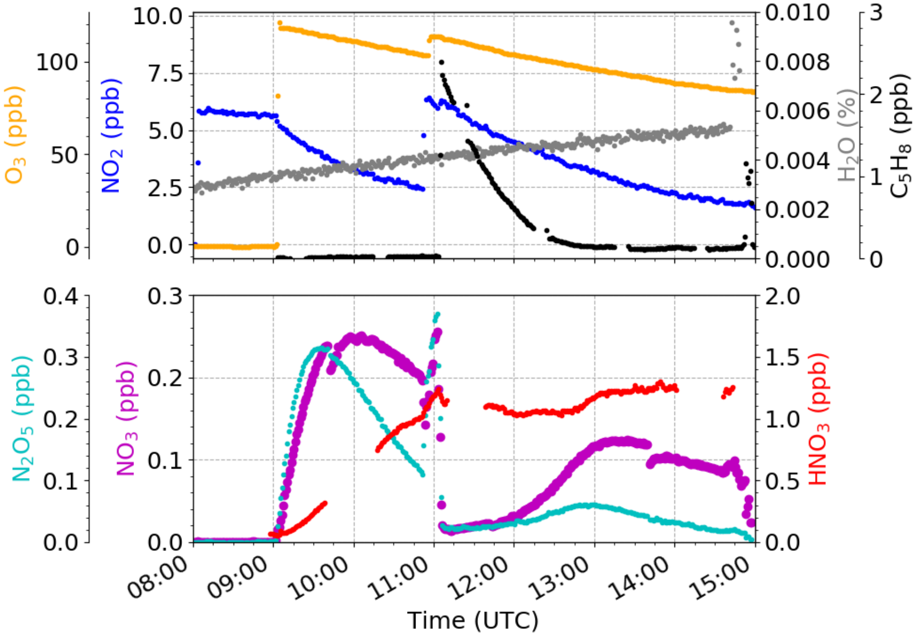

Figure 5.7: Time series of HNO_3 and relevant species on August 2, 2018, similar to Fig. 5.5. The mixing ratio of C_5H_8 (PTR-1000) is shown in black on the right y-axis in the upper panel.

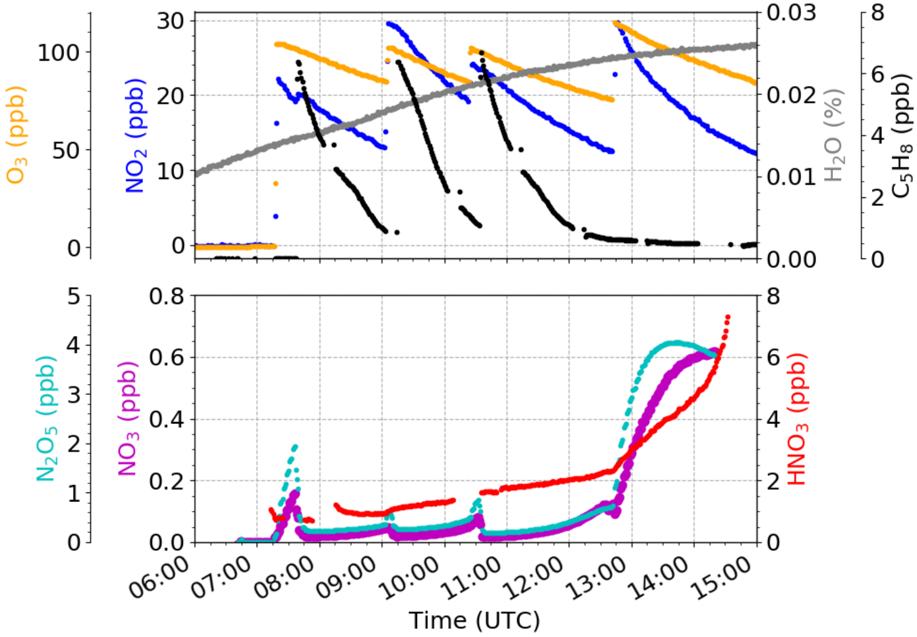

Figure 5.8: Time series of HNO_3 and relevant species on August 8, 2018, similar to Fig. 5.7.

this time period, the reaction of NO_3 with C_5H_8 dominated the system [6, 42]. Although the reaction of NO_3 with NO_2 was competitive [21] against the NO_3-initiated oxidation of C_5H_8, HNO_3 production was constrained by the combination of N_2O_5 with H_2O [146], of which the rate constant k_2 is very small under relatively dry conditions. Only when C_5H_8 was nearly depleted did HNO_3 start to rise again to 1.4 ppb, as NO_3 and N_2O_5 were exclusively reacting to form HNO_3.

5.4.3 Tests with high amounts of NO_2 and C_5H_8

The experiment on August 8 was set up with 7 ppb C_5H_8, 13 – 30 ppb NO_2 and 75 – 115 ppb O_3, as is shown in Table 5.3 and the upper panel of Fig. 5.8. During the day, re-injections of the above species were done for three times to maintain the reactivity of in-situ produced organic species. FunMass was switched for measurements at around 7:20.

Similar to the case on August 2, x_HNO$_3$ grew only slightly and slowly during the fast depletion of C_5H_8. During the three additions of C_5H_8, the growth of HNO_3 was almost linear from 0.8 ppb to 2.2 ppb until C_5H_8 was completely depleted at 12:45. Right after NO_2 and O_3 were supplemented for the fourth time, NO_3, N_2O_5 and HNO_3 all became to increase at a stranger rate instantly. HNO_3 hit 7.5 ppb before the sampling process was cut off at around 14:30.

However, the yield of HNO_3 on this day may be seriously underestimated due to the leak of hydrochloric acid (HCl) into the chamber from the LOPAP instrument when measuring nitrous acid (HNO_2). Despite that the amount of HCl leaked into the chamber can not be quantified, the contamination of HCl in the chamber caused a huge depletion of the reagent ion CO_3^- and the formation of chlorine-containing ions, as is illustrated by the spectra in Fig. 5.9. The differences between the spectra from blank (∼ 10:30) and chamber air (∼ 11:00) measurements

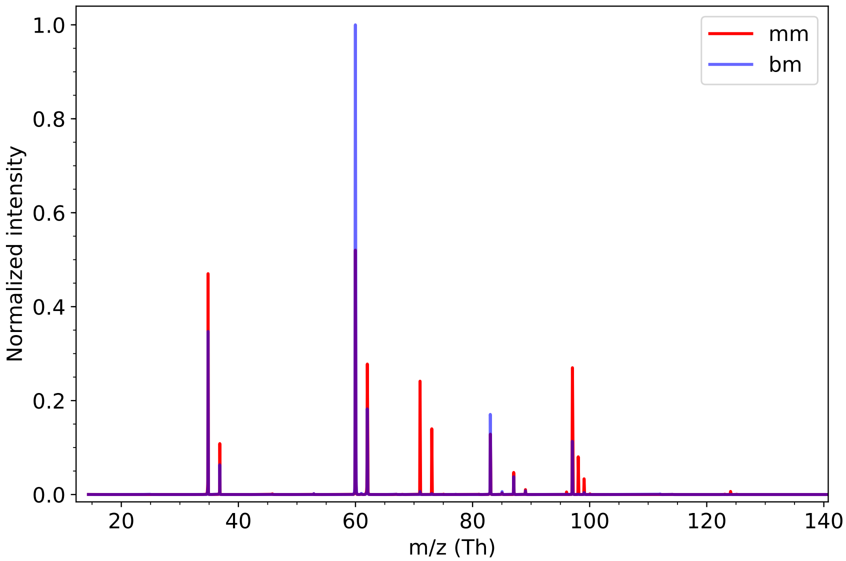

Figure 5.9: Mass Spectra of blank (bm, blue) and chamber air (mm, red) measurements at around 11:00 on August 8. Mass peak intensities are normalized to the CO_3^- (60 Th) signal from the blank mode. Half of the CO_3^- are depleted due to the HCl contamination and many chlorine-related ions are formed.

demonstrate that around half of CO_3^- ions were consumed by other species and meanwhile many other product ions were formed, such as 35/37 Th and 71/73/75 Th, which are most likely the mass peaks of Cl^- and $Cl^-(HCN)$ respectively. The fact that CO_3^- was considerably depleted by an excess of analytes adds uncertainty to the quantification of HNO_3 especially from 13:00 on towards the end of the experiment. As a consequence of the heavy depletion of CO_3^- ions the calibration for HNO_3 will no longer be just linear in its abundance. With NO_3^- ions becoming more abundant, HNO_3 reacting to NO_3^- to form $NO_3^-(HNO_3)$ (125 Th) will be largely prompted. The contamination of HCl in the chamber, therefore, could have caused a severe underestimation of the HNO_3 yield on August 8, which will accordingly put the measurements for this day into question.

The same experiment was repeated on August 13 except that NO_2 (12 – 23 ppb) and C_5H_8 (5 – 6 ppb) were in slightly lower mixing ratios, as is shown in Fig. 5.10. Nevertheless the amounts of NO_3 and N_2O_5 were almost doubled before the fourth injection of NO_2 and O_3 in comparison to August 8, according to the MPI-CRDS instrument. Consequently, the yield of HNO_3 for this day was four times the amount on August 8. From the first addition of C_5H_8 at 7:30 to right before the last injection of NO_2 and O_3, HNO_3 experienced a slowly steady rise from 0.06 ppb (the background in the chamber) to 9 ppb in almost 7 hours. The last addition of NO_2 and O_3 caused an increase of NO_3 and N_2O_5 by a factor of ~ 3. In the meantime, a fast and strong HNO_3 formation was observed with HNO_3 increasing by a factor of ~ 5 from 9 ppb to 47 ppb.

For both cases, the x_HNO_3 increased very slowly during the first three injections of initial reactants, because the formation of HNO_3 from N_2O_5 was severely hindered by the oxidation of the large amount of C_5H_8. In addition, the water content was rather low in the chamber.

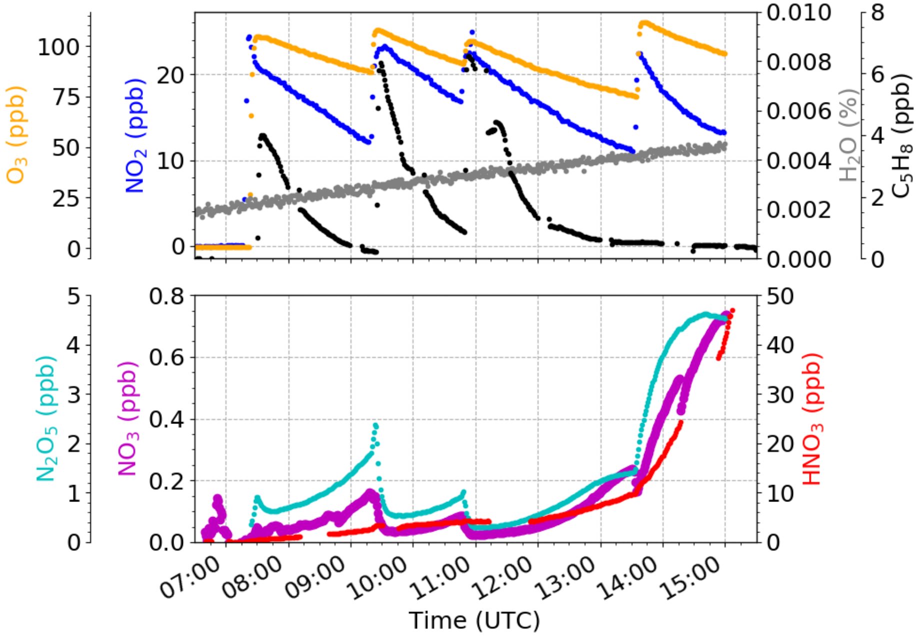

Figure 5.10: Time series of HNO_3 and relevant species on August 13, 2018, similar to Fig. 5.7.

HNO_3 production is, therefore, somewhat suppressed in spite of the presence of NO_3 radicals and N_2O_5. As soon as C_5H_8 was totally depleted in the chamber, the growth of NO_3 and N_2O_5 was sky-rocketing accompanied by the formation of HNO_3. Figure 5.11 shows the spectra of blank ($\sim$ 14:30) and chamber air ($\sim$ 15:00) measurements from the last addition of NO_2 and O_3 on August 13, which illustrates there was no significant depletion of the CO_3^- ion even when 50 ppb HNO_3 was subjected to analysis. From this point of view, the production of HNO_3 on August 8 could be severely underestimated due to the mostly consumed CO_3^- ion by HCl, considering the increases of NO_3, N_2O_5 and HNO_3 before and after the final injection of NO_2 and O_3.

5.5 HNO_3 production with seed aerosols in the chamber

5.5.1 Indirect and direct HNO_3 production from NO_2-O_3-H_2O and N_2O_5

$(NH_4)_2SO_4$ seed aerosols were injected into the chamber for the first time on August 14 to monitor SOA formation from NO_3-initiated oxidation of C_5H_8. It is generated from a special generator producing particles with a mean diameter of $\sim$ 80 nm. The initial mass concentration of seed aerosols in the chamber is 30 – 50 μg cm^{-3}. The injection of seed aerosols slightly humidifies the chamber (0.1 %), which is, however, still considered as dry conditions. As is obviously shown in Fig. 5.12, NO_2 and O_3 were added into the chamber at an approximate amount of 20 ppb and 110 ppb respectively, leading to a production of $\sim$ 10 ppt NO_3 radicals, measured by the CRDS-ICARE instrument. HNO_3 climbed up to 4 ppb before 12 ppb C_5H_8 was injected. Along with the injection of C_5H_8, the rapid increase of HNO_3 stopped and it dropped back to around 2 ppb. Minor fluctuations in HNO_3 were observed with the second addition

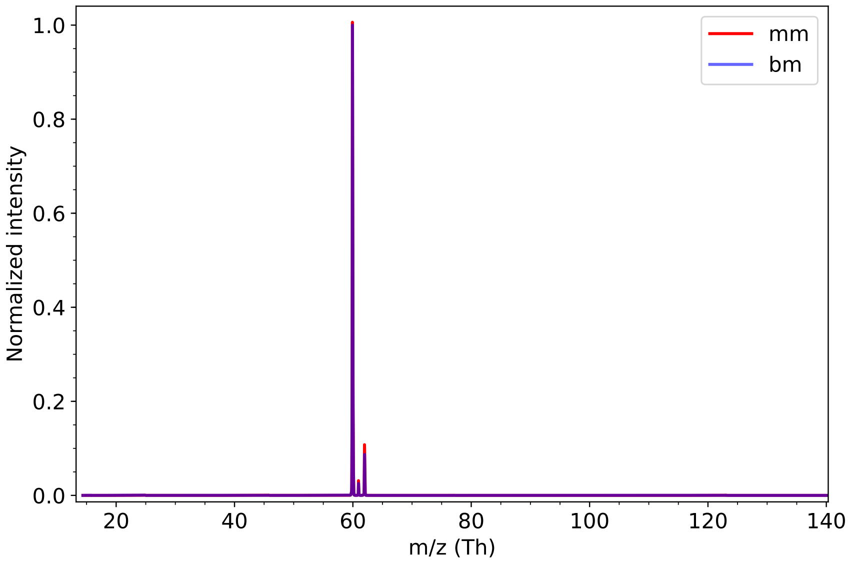

Figure 5.11: Mass Spectra of blank (bm, blue) and chamber air (mm, red) measurements from the last addition of NO_2 and O_3 on August 13, similar to Fig. 5.9.

of C_5H_8. Similar to previous cases, HNO_3 started to gradually rise again at around 13:00 with about 80 % of C_5H_8 being depleted.

The experiment on August 19 shown in Fig. 5.13 was a test with N_2O_5 being the source of NO_3 radicals. Liquid N_2O_5 was evaporated at a rate of 1.5 ppb per hour with 200 sccm bypass flow through a N_2O_5 cold trap. The production rate of N_2O_5 was similar to its gas-phase formation rate from the NO_2-O_3 reaction in previous experiments. H_2O was kept at the same level as that on August 14, but the amount of NO_3 decreased to 0.05 ppb after an initial surge up to 0.46 ppb before the first C_5H_8 injection at 8:30, according to the CRDS-ICARE instrument. As can be seen in the upper panel of Fig. 5.13, the amount of NO_2 kept growing due to the decomposition of N_2O_5. In this case the consumption of NO_3 by C_5H_8 led to increased N_2O_5 decomposition from the equilibrium between N_2O_5 and NO_2/NO_3, as is obviously shown by the sharp drop in N_2O_5. Initially, HNO_3 experienced a sharp increase, synchronized with the surge of NO_3. HNO_3 began to increase very slowly at 8:30 when the addition of C_5H_8 took place and NO_2 formation was speeding up. The second injection of C_5H_8 caused a slight decrease of HNO_3 at shortly past 9:00. The third addition of C_5H_8 didn't cause very obvious changes in HNO_3, though NO_2 was increasing steadily. This indicates that NO_3 radicals were slowly increasing from the equilibrium with N_2O_5 as C_5H_8 was being depleted. Bringing in O_3 at 13:30 resulted in fast NO_2 consumption and rapid NO_3 formationas well as a strong growth of HNO_3, as is clearly shown in the lower panel of Fig. 5.13.

With similar amounts of NO_2 and H_2O in the chamber on August 14 and August 19, the final HNO_3 production on August 19 was nearly double the amount on August 14. The addition of C_5H_8 very likely caused the difference in HNO_3 formation. Regardless of the different x_NO_3 and x_N_2O_5 on August 14 and 19, HNO_3 yields on both days were similar ($\sim$ 4 ppb) before the injection of C_5H_8. This means that ammonium sulphate seed aerosols don't influence

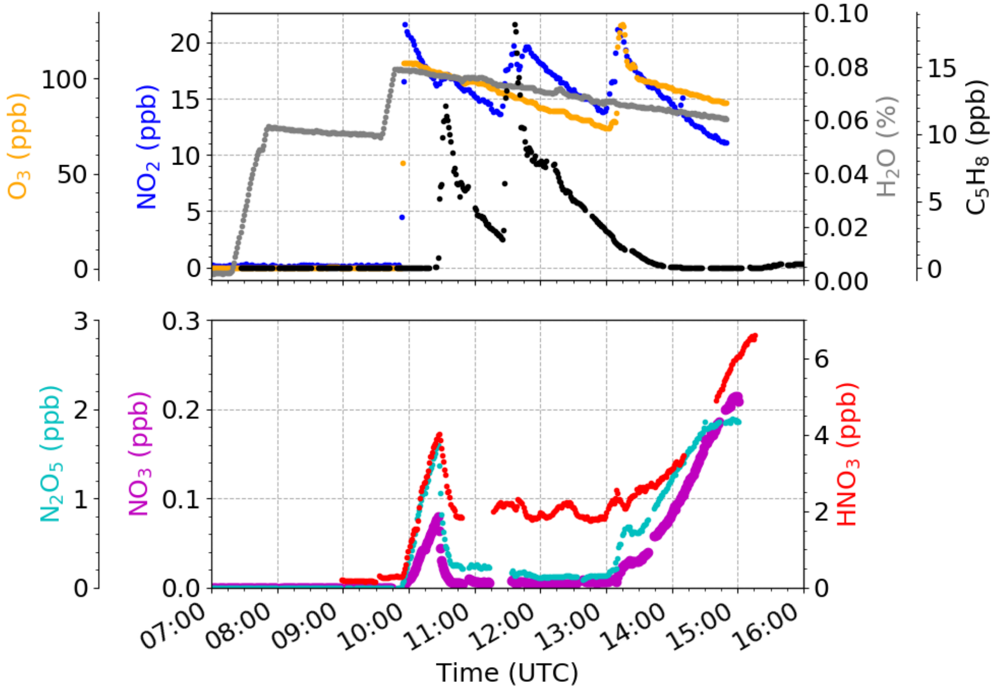

Figure 5.12: Time series of HNO_3 and relevant species on August 14, 2018 without humidification. Seed aerosol injection stopped at 9:47.

the formation of HNO_3 under dry conditions. When 10 ppb C_5H_8 was introduced into the chamber, HNO_3 experienced a strong decrease by 2 ppb on August 14, which was not observed on August 19 with an addition of less than 2.5 ppb C_5H_8. Not until C_5H_8 was almost fully completed did HNO_3 start to rise again at around 13:30 with the same amounts of NO_2 and O_3 added at the last injection on both days. The HNO_3 production rate after the final addition was much faster with more NO_3 radicals formed on August 19.

5.5.2 Nighttime and daytime chemistry combined experiment

One nighttime and daytime chemistry combined experiment was carried out under humid conditions on August 18. The chamber was humidified to contain 1.4 % H_2O so that the seed aerosols would take up water to form aqueous aerosols, which will increase the partitioning of oxygenated products onto/into the aerosol. Besides, β-caryophylene was added along with the first injection of O_3 to organically coat the seed aerosols. In this case, NO_2 and C_5H_8 were kept at low concentrations, 5 and 2 ppb respectively as indicated in Fig. 5.14, which caused a quite low production of $\sim$ 2 ppt NO_3 radicals in the system. However, HNO_3 reached a higher yield in the dark than that on August 2, which could be most probably caused by the high humidity and aerosol concentration. On August 24 (under dark conditions, Fig. A.5 in Appendix A), NO_3 and H_2O were at very similar levels but HNO_3 was heavily reduced to only 0.3 ppb with a much higher abundance of C_5H_8 (5 – 20 ppb). Even though the reaction of NO_3 with NO_2 is $\sim$ 4 times faster (k_1) than the oxidation of C_5H_8 by NO_3 radicals, the fast decomposition of N_2O_5 constrains the formation of HNO_3. With more C_5H_8 added into the chamber, N_2O_5 is promoted

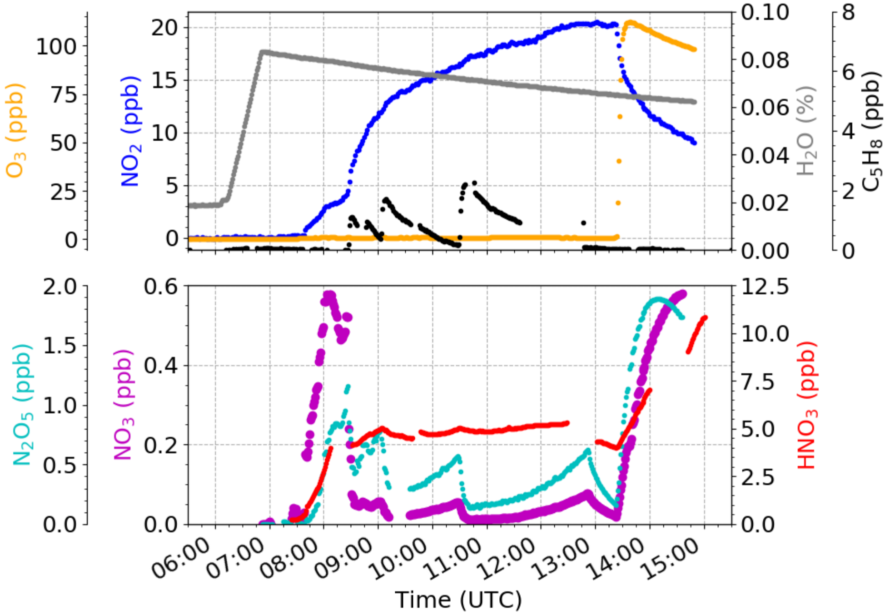

Figure 5.13: Time series of HNO_3 and relevant species on August 19, 2018 without additional humidification. N_2O_5 was added as the source of NO_3. Seed aerosol injection started at 6:05 and ended at 6:50.

to decompose by the continuously consumption of NO_3 by C_5H_8. This further illustrates the strong negative impact of C_5H_8 oxidation on HNO_3 production in the system.

The measurement of HNO_3 on August 18 started only after the humidification. As soon as O_3 was injected, HNO_3 started to rise up continuously. This is contradictory to previous cases, for example, on August 2 and August 22 (Fig. A.4), where HNO_3 started to form only after adding both NO_2 and O_3. The disequilibrium between adsorption and desorption of H_2O on the chamber wall may account for immediate increase of HNO_3 from [O3] injection only. All additions of NO_2, O_3 and C_5H_8 were completed before opening the chamber roof.

The chamber was exposed to sunlight at 11:07, when a sharp decrease in NO_3 and N_2O_5 happened immediately as can be clearly seen in Fig. 5.14. An acute drop of HNO_3 by 0.8 ppb accompanied but delayed by around 40 minutes. Because even if NO_3 radicals and N_2O_5 instantly decomposed due to photolysis as soon as the whole environment was exposed to sunlight, OH radicals were generated from the photolysis of O_3 (R1 and R2 in Chapter 1). The reaction of OH radicals with NO_2 (Fig. 1.3) will continue to contribute to the production of HNO_3. This is the reason why a very slow increase in HNO_3 appeared shortly after the chamber roof open and between 11:45 – 13:00 in Fig. 5.14.

To understand the abrupt drop in HNO_3 at around 11:45, the raw CO_3^- and $CO_3^-(HNO_3)$ signals were checked. An increase, which did not really appear in 123 Th, happened to 60 Th at 11:45, making the normalized $CO_3^-(HNO_3)$ signal (123 Th to 60 Th) diminish and consequently causing the decrease of HNO_3. The change in CO_3^- is very likely not due to the drift in the DBD-IS, because the change in the DBD-IS tends to have the same influence on both CO_3^- and $CO_3^-(HNO_3)$ based on laboratory experiments on the performance of DBD-IS. It could be that the there were less ion-molecule reactions involving CO_3^- ions as a result of the photolysis of some oxidized products after the chamber roof was open. Regardless of the sudden change in CO_3^-, an average amount of $\sim$ 2.5 ppb HNO_3 remained in the chamber by calculating with the

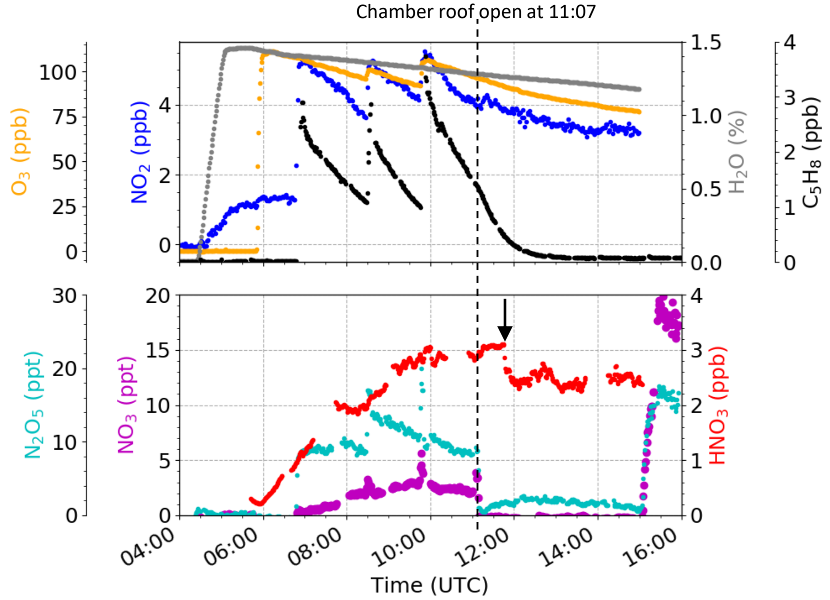

Figure 5.14: Time series of HNO_3 and relevant species on August 18, 2018. The chamber roof was opened at 11:07 and was closed at 15:01. The black arrow in the lower panel points to the sharp decrease in HNO_3 at around 11:45 due to the sudden increase of CO_3^-.

normalized signal of $CO_3^-(HNO_3)$. However, x_HNO$_3$ could also be kept at slightly above 3 ppb if only considering the flat signal of $CO_3^-(HNO_3)$ after the chamber roof was open. As the shutter of the chamber closed at 15:30, NO_3 and N_2O_5 sprang up again. The FunMass HNO_3 measurement had stopped already, however, a strong increase in HNO_3 could be expected from previous its behaviour.

5.6 Detection of organic nitrates

Carbonate ions provide good performances in detecting inorganic gases, like SO_2, HNO_3 and HCN in FunMass [2, 64]. As for organic species, laboratory experiments were carried out to study the reaction of CO_3^- with formic acid (HCOOH) and acetic acid (CH_3COOH)[141]. Besides, the ion-molecule reaction of CO_3^- with HCOOH was investigated in a computational study by Papa and Elrod [18]. However, the application of CO_3^--CIMS to measure oxidised products from the atmospheric oxidation of BVOCs, for example C_5H_8, has not yet been reported.

Figure 5.15 shows the FunMass mass spectra normalized to the peak intensity of the reagent ion CO_3^- at 14:00 for the blank mode (mm) and 14:20 for the measurement mode (mm) on August 14. Table 5.1 in Sec. 5.1 lists the organic nitrates that have been assigned for the first time in the CO_3^--CIMS spectra of FunMass based on previous studies [99, 120, 127]. The corresponding reaction pathways to form these organic nitrates have been illustrated in Fig. 5.1. Some other product ions at higher mass-to-charge ratios, for example 254 Th, 352 Th, 368 Th and 384 Th, were also observed with FunMass during chamber air measurements, but they

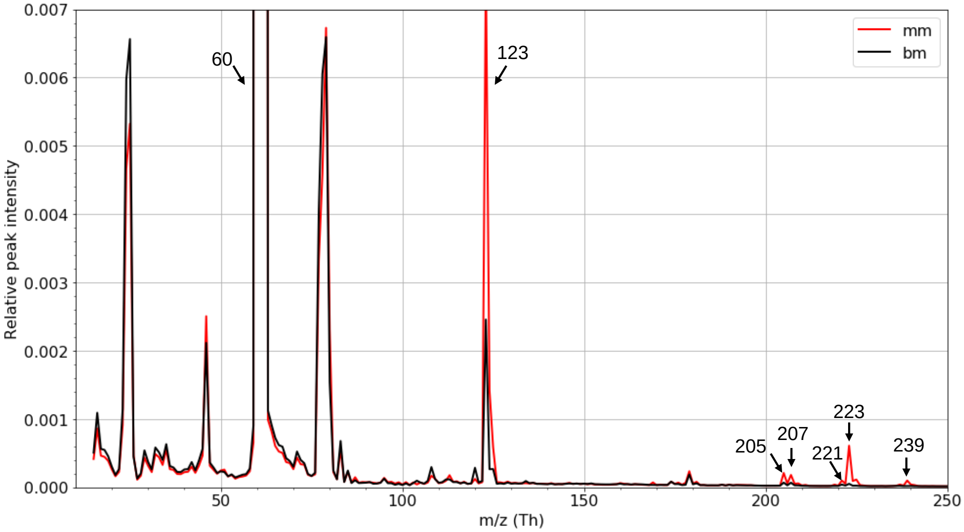

Figure 5.15: Mass spectra of measured organic nitrates for the blank (black) and chamber air (red) measurements at 14:20 and 14:00 respectively on August 14, 2018. The mass spectra are scaled to the reagent ion peak (m/z = 60).

could not be identified yet based on literature. Thus, discussions are focused only on the masses listed in the table.

Due to the shortage of synthetic standards for the complex and unstable reaction products, calibration is unavailable for the organic nitrates mentioned here. Instead, the normalized signals, namely the signal ratios of the respective cluster ions to CO_3^- — as introduced in Chapter 2 — are used as the reference, which should be proportional to the actual concentrations. Therefore, the organic species measured by FunMass cannot be quantitatively discussed herein. However, several other mass spectrometric measurements detecting the same organic species can be used for a qualitative inter-comparison.

1. The Vocus-PTR of the Institute of Energy and Climate Research: Troposphere (IEK-8). It has a resolving power of 12000 and provides very good mass accuracy for distinguishing most isobaric species. The measurements of the Vocus-PTR are calibrated by addition of certain amounts of hydrocarbons, such as C_5H_8, MVK, MACR, *etc.*, which should ensure a stable but unfortunately not absolute calibration for the organic nitrates.

2. The I^--CIMS of University of Gothenburg [23] measures organic compounds in both gas and particle phase. To measure the composition in aerosols, particles are collected on a Teflon filter and then vaporized with heated nitrogen.

3. The Br^--CIMS of IEK-8 [3] provides a good selectivity and sensitivity for hydroperoxyl radical (HO_2) measurements and is also sensitive to organic nitrates. It has an online calibration unit for HO_2 radicals.

Normalized isoprene nitrate peroxide (INP) measurements of the instruments listed above are compared for 3 selected days — August 13, 14 and 19 — in Fig. 5.16.

The left panels of the figure are the time series of INP on the corresponding days measured by Vocus-PTR (gold), I^--CIMS (blue) and Br^--CIMS (magenta) together with x_C_5H_8. The

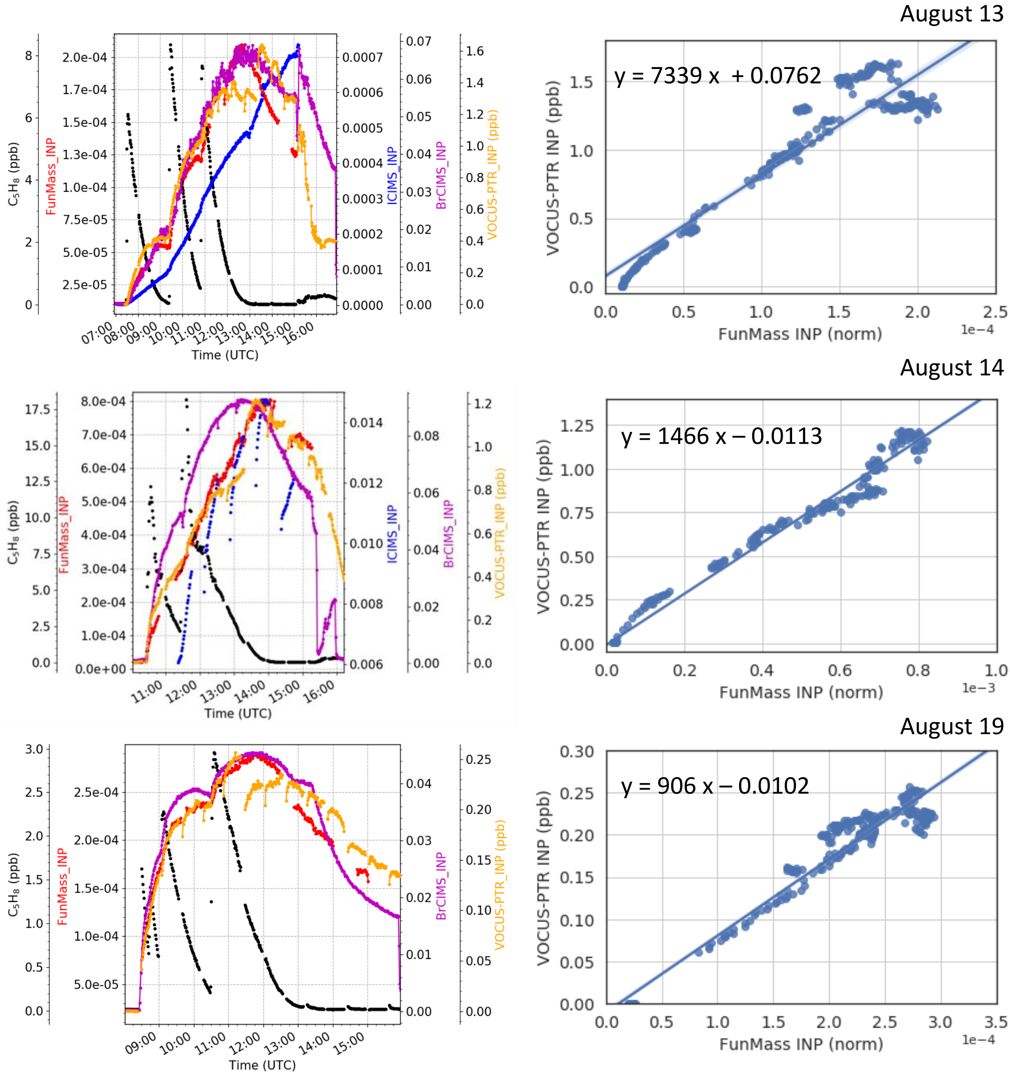

Figure 5.16: On the left: time series of normalized INP signals from FunMass (red), I^--CIMS (blue), Br^--CIMS (magenta), INP (gold) and C_5H_8 (black) concentrations in ppb from Vocus-PTR on August 13 (top), August 14 (middle) and August 19 (bottom). On the right: linear regression of INP between FunMass (x-axes) and Vocus-PTR (y-axes) on corresponding days. The small breaks in the FunMass INP time series are due to HNO_3 calibration intervals.

Vocus-PTR provided roughly calibrated x_INP based on the isotopic ratio of C^{13} labelled C_5H_8 to the standard counterpart, while the INP signals provided by I^--CIMS and Br^--CIMS were normalized to the total ion counts instead of the reagent ions. Relative traces mostly show good (FunMass and Br^--CIMS) to excellent (FunMass and Vocus-PTR) agreements among these three days. More time series from other experiment days can be found in Figs. A.8 and A.9. Just the I^--CIMS shows some systematic differences which may be due to their heating cycles to evaporate aerosols from the Teflon filter. The INP signal in FunMass started rising immediately after the first injection of C_5H_8 and also responded to other additions of C_5H_8 well, synchronized with the changes of INP in Vocus-PTR and Br^--CIMS. Therefore, CO_3^--CIMS seems to have a very good performance in detecting INP from the oxidation of C_5H_8, even though the mass resolution of FunMass is 20 times lower than that of Vocus-PTR, which for organic substances often causes strong overlaps with other isobaric species. But due to the high specificity of negative ionization, CO_3^--CIMS seems highly selective to INP and probably also to the other detected nitrates listed in Table 5.1 which, however, still needs to be further investigated.

The right panels show the linear regressions between normalized INP signal from FunMass (x-axes) and INP mixing ratios (x_INP) given by Vocus-PTR (y-axes) on the three selected days. FunMass INP and Vocus-PTR INP are very nicely correlated with each other on a single experiment day. But during the whole campaign when both instruments acquired INP data, the linear correlation between FunMass and Vocus-PTR INP varies from one day to another, as is shown in Figure. A.6 where all FunMass and Vocus-PTR INP from August 10 – 24 are plotted. The linear regression coefficient on many days was around 1550, like on August 14 (the upper left plot in Fig. 5.16). On some other days, the sensitivity of FunMass to INP became either somewhat higher (August 19: 906) or much lower (August 13: 7343), if considering the measurements by Vocus-PTR close to reality.

A similar kind of variation in INP is observed between Br^--CIMS and Vocus-PTR as well (Fig. A.7). For example, when Vocus-PTR measured 1.2 ppb INP on both August 13 and 14, the normalized signal of Br^--CIMS INP on August 13 was only half the value on August 14. The maximum signal from Br^--CIMS, which was equal to 0.45 ppb on August 14, corresponded to only 0.25 ppb INP from Vocus-PTR In this perspective on August 19. In this perspective, FunMass and BR^--CIMS therefore agreed with each other on INP measurements but differed from Vocus-PTR, which was perhaps a result of the interference from other organic species, given that the positive ionisation in Vocus-PTR is less selective. However, the correlation between FunMass and Br^--CIMS INP varied as well during the same time period in a similar way that happened between FunMass and Vocus-PTR INP, as is shown in Fig. A.7, which should not happen since all instruments undergo daily calibration procedures that should also ensure a constant relative calibration coefficient for INP. The reasons for the strong variation in the correlation coefficient between sensitivities of different instruments for INP (and maybe also for other species) needs to be cleared up and a technique to do reliable absolute calibrations for such species needs to be developed.

An example of the measurement of other first-generation organic nitrates, namely ICN, IHN, IHCN, ICPN and IHPN, is shown in Fig. 5.17, with August 13 on the upper panel and August 14 on the lower panel. The experiments were carried out with very similar amounts of NO_2 and O_3 and under relatively dry conditions, although the addition of seed aerosols slightly humidified the environment on August 14. The initial x_C_5H_8 on August 14 ($\sim$11 ppb) was almost double the amount on August 13, which resulted in a higher production of organic nitrates. Each time when C_5H_8 was injected (the black arrows in Fig. 5.17), a clear step was found at the same time in organic nitrate evolution, especially obvious in INP, ICN and IHN on August 13. The reason for this could be the faster reactions of the peroxy nitrate radicals INO_2 with HO_2, RO_2 and NO/NO_3, as shown in Fig. 5.1, while the formation of ICPN, IHCN and IHPN takes further reaction steps and thus is slower. The fact that the changes in INP, ICN and IHN with C_5H_8 addition were less obvious on August 14 in spite of higher x_C_5H_8 could be a result from the gas-particle partitioning process with seed aerosols introduced into the chamber and the fact that FunMass measured only the gaseous organic nitrates. When C_5H_8 was completely consumed at 12:30 on August 13 and 14:00 on August 14, INP, ICN and IHN, IHCN and IHPN stopped accumulating and started to decrease because of further reactions or dilution in the chamber, while ICPN was still formed via the slow 1,4-H-shift reaction pathway.

(a) August 13

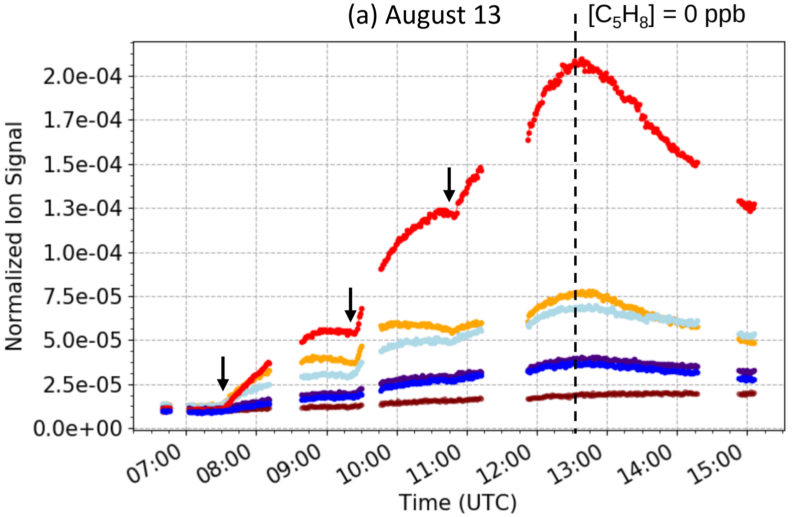

(b) August 14

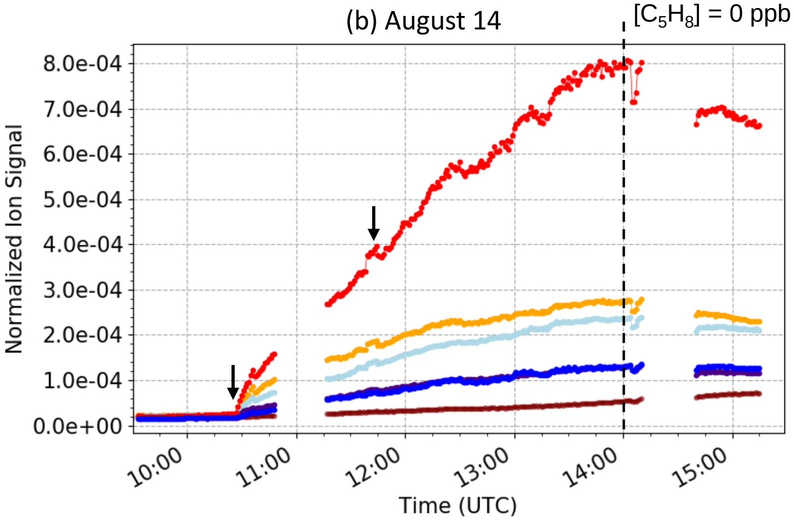

Figure 5.17: Time series of INP (red), ICN (orange), IHN (light blue), IHCN (indigo), ICPN (maroon) and IHPN (blue) on August 13 and August 14. The y-axes show normalized ion-cluster signals of these nitrates. The black arrow marks the addition of ∼ 11 ppb C_5H_8 on August 13 and ∼ 6 ppb on August 14. The black dashed lines indicate when C_5H_8 were consumed. See Figs. 5.10 and 5.12 for the initial mixing ratios of reactants and seed aerosol injection

Figure A.10 shows more product ion signals of organic nitrates detected with FunMass from other experiment days which are, however, not further discussed here.

HNO_3 can be principally ionised with both naked CO_3^- ions as well as $CO_3^-(H_2O)$ cluster ions. Although $CO_3^-(H_2O)$ does not improve the conversion of HNO_3 to $CO_3^-(HNO_3)$ [64] due probably to insufficient humidity in the IMR chamber, the $CO_3^-(HNO_3)$ cluster ions are still detected with high sensitivity with the CO_3^- ionisation scheme. This cluster is very stable and easily survives the transfer stage settings, which are optimized to serve for the detection of $CO_3^-(HNO_3)$ and has the advantage of supplying efficient ion transfer. The settings in the ion transfer stage are quite "hard" on clusters, such as $CO_3^-(HCN)$, and do not necessarily favour the generation of other cluster ions of the organic nitrates. Therefore, a better performance of FunMass on organic nitrate measurements can potentially be achieved by adjusting the settings in the ionisation and transfer stage so that the CO_3^--nitrate cluster ions formed in the IMR can survive the transfer stage leading to higher production and transmission for the organic clusters in a higher mass range.

5.7 Conclusion

FunMass was deployed to measure gaseous HNO_3 in the atmospheric simulation chamber SAPHIR during the time period of July 31 – August 24 in 2018, when a campaign took place to study the NO_3-initiated nighttime oxidation of isoprene. An innovative and up-to-date concentric-DBD ion source was used for the first time in a measurement campaign to dominantly generate the CO_3^- reagent ion. A flexible sampling system with online calibration for HNO_3 was designed and operated to reliably quantify the yield of HNO_3. The online calibration unit is a home-made permeation oven with a permeation tube constantly releasing gaseous HNO_3. The $k_p\_HNO_3$ was determined to be 9.53 ng min^{-1} with simultaneous ion chromatographic analyses during the campaign.The measurements have yielded several interesting results:

1. The formation of HNO_3 from NO_3-initiated oxidation of C_5H_8 was controlled by NO_2, O_3, C_5H_8 and humidity in the chamber, and was independent of seed aerosol injection. Comparable amounts of HNO_3 were measured by FunMass from the gas and aerosol phase experiments under relatively dry conditions (Figs. 5.8 and 5.12).

2. The production of HNO_3 was rather low (< 1.5 ppb) for an amount of 6 ppb NO_2 injected into the chamber (Fig. 5.7), but was greatly enhanced when more NO_2 and O_3 was added to the chamber (Figs. 5.8 and 5.6). The addition of C_5H_8 suppressed the formation of HNO_3 due to the competitiveness of C_5H_8 reacting with NO_3 radicals, reducing the formation of N_2O_5, which is the direct nocturnal source of HNO_3 (Figs. 5.7, 5.8 and 5.12) and decomposes very fast to NO_3 radicals.

3. From the production rates of HNO_3 on different days, the formation of HNO_3 in the chamber can be either from the homogenous reaction of N_2O_5 with H_2O from which the production rate of HNO_3 is very slow as on July 31/ August 2, or from the heterogeneous reaction involving aqueous particles from which HNO_3 can be produced in a large amount in a short time period ($\sim$ 1 – 2 h), e.g. on August 13, 14 and 17. The results from FunMass HNO_3 measurements resemble what has been shown in previous chamber studies [146, 147].

4. Humidity influences not only the HNO_3 background signal in the chamber but also the yield of HNO_3. Because gaseous HNO_3 is very sticky, the humidity in the chamber could break the equilibrium between HNO_3 in the gas phase and HNO_3 adsorbed on all the walls. A stable background of 100 ppb was observed during dry gas phase

experiments (Fig. 5.5). With the chamber being humidified, the desorption of HNO_3 from the walls caused a stronger HNO_3 background, which may be due to the large adsorption effect of water on the walls. Thereafter, the uptake of gaseous HNO_3 by water made the background signal in humid conditions keep dropping until NO_2 and O_3 was injected (Fig. 5.14). Comparing the experiment on August 2 with the nighttime part on August 18 and considering only one injection of all the reactants, the amount of HNO_3 formed under humid condition (Fig. 5.14) doubled that under dry condition (Figs. 5.7). Therefore, it is very important to consider carefully the wall effect of HNO_3 when discussing the production of HNO_3 under different environmental conditions.

5. The CO_3^- ionisation technique also provides primary access to measure the first generation organic nitrates from the oxidation of C_5H_8 by the NO_3 radical. FunMass detected in total 6 nitrate species including INP, IHN, ICN, IHCN, IHPN and ICPN, among which INP gave the strongest signal. A good linear correlation especially between FunMass and Vocus-PTR INP measurements is found on each experiment day, however, the relative sensitivity appear to vary strongly from day to day over the campaign without systematic behaviour. Good agreements on INP are also found among the three negative ionisation mass spectrometric (FunMass, Br^--CIMS and partly I^--CIMS) measurements. It seems that there may be some problem with the calibration stability of the Vocus-PTR. This important issue is under further investigation. The measurements of other nitrates were not so responsive as INP to the injection of C_5H_8, which may be due to their slower multi-stage production rates or the settings in the ion transfer stage which do not favour weakly bonded clusters and could be somewhat modified to transmit more of these product ion clusters. For any further measurements on this subject FunMass should be upgraded using some technique to absolutely calibrate at least with some similar organic nitrate species.

Chapter 6

Conclusions and perspectives

6.1 Conclusions

Atmospheric processes important for air quality or global climate are often dominated by trace species at mixing ratios in low *ppb* down to *sub-ppt* range. In order to properly understand corresponding chemical and physical processes, highly sensitive and spatially well-resolved measurements in the atmosphere are essential to validate and improve respective models for reliable future prognoses.

This work presents the first detailed validation and interpretation of HNO_3 and HCN data obtained during the first two campaign deployments of the innovative Chemical Ionization Time-of-Flight Mass Spectrometer FunMass [64]. These campaigns have focussed on science objectives as versatile as UTLS chemistry and dynamics above the Asian Monsoon region with FunMass on board the high altitude research aircraft M55-Geophysica for the 2017 StratoClim campaign on one hand and the nighttime oxidation of isoprene explored during the 2018 NO_3-Isoprene campaign in the atmospheric simulation chamber SAPHIR on the other hand.

Preparations about laboratory tests and optimization on FunMass measuring SO_2 and HNO_3 with the reagent ion CO_3^- produced from the standard Dielectric Barrier Discharge (DBD) ion source were done before the StratoClim campaign. In flight, the sampling inlet of FunMass was SilcoNert-coated and heated to improve the transmission of trace gases. An online calibration unit with a standard SO_2 gas mixture (100 ppb) was deployed for the airborne measurements. But due to a leakage in the SO_2 calibration source, no valid SO_2 data were determined from the aircraft campaign. Data analysis on HNO_3 and HCN had to rely on post flight calibrations employing a home-build permeation oven, which poses some uncertainties to the determination of their ambient mixing ratios due to the uncertainty in HNO_3 permeation rate and extrapolating HCN from the calibration with relatively high mixing ratios. To more reliably quantify HNO_3 measured in the chamber study, HNO_3 was calibrated online with the permeation oven, while in parallel the permeation rate of HNO_3 was cross-checked against ion chromatographic analyses. The wall loss of HNO_3 in the sampling system was avoided by using Teflon tubing, valves and nozzle, which were tested in the laboratory to provide the best transmission for HNO_3.

FunMass HNO_3 and HCN measured during the 6th and 7th flight of the StratoClim Nepal campaign are compared to satellite observations of HNO_3 by the Microwave Limb Sounder (MLS) and HCN by the Fourier Transform Spectrometer ACE-FTS in the Asian Monsoon Anticyclone (AMA) and the lower stratosphere atop it. Good agreements are found between the in-situ airborne measurements and remote observations, which in turn ensures the data quality of the satellite measurements.

HCN structures in the troposphere and tropopause region indicate the existence of a convective outflow layer at around 365 K with HCN enhanced in a way different from the observed flat CO structure. The differences in observed HCN and CO could be attributed to the inhomogeneous and homogeneous boundary distribution of HCN and CO, respectively, due to their different biomass burning emission factors. In the lower stratosphere from 420 to 437 K, a filament of high HNO_3/O_3 and in parallel high HCN further supports the concept of the top of confinement (TOC) layer in the lower stratosphere above the AMA, suggested by Brunamonti and co-authors based on balloon measurements [15]. Besides, the northward tilted filament shown in observed HNO_3 and HCN can be an indicator of in-mixing of the middle or high latitudes stratospheric air into the TOC layer, since the air in the filament has an mean age of around 4 – 8 months older than the young air in this TOC layer (simulated by CLaMS employing ERA-Interim meteorological fields). It reveals the TOC layer is a more horizontally constricted area and is a mixture of young air ascending from the AMA and old air intruding from the stratosphere.

HNO_3 measured in the SAPHIR chamber with online calibrations show very different HNO_3 production when studying NO_3-initiated oxidation of isoprene under different well controlled environments. Four factors have been considered with HNO_3 measurements: (1) The formation of HNO_3 could be from homogeneous (slow) or heterogeneous (fast) reactions regardless of the mixing ratio of water in the chamber. (2) The humidification causes the desorption of HNO_3 from the chamber wall, which in turn implies possible underestimation of gas-phase HNO_3 formation due to the uptake of HNO_3 by the walls. (3) Aerosols injected or formed in the chamber seems to play a role in the production of gaseous HNO_3 as well. However, the influence is very hard to quantify without detailed modelling. (4) Last but not the least, one calibration issue, namely the depletion of reagent ions, may affect the determination of extremely high HNO_3 amounts generated towards the end of some measurement days.

This thesis demonstrates, for the first time, that the CO_3^- ionisation scheme shows good performance in detecting organic nitrates such as Isoprene Nitrate Peroxide (INP), Isoprene Carbonyl Nitrate (ICN) and the like. Due to a lack of standard gases for online calibration, it is, however, hard to quantify the amounts of the nitrate species. Nevertheless, efforts were made to qualitatively judge the INP measurements by comparing the normalized CO_3^--INP cluster signal from FunMass with other mass spectrometric measurements (Br^--CIMS and Vocus-PTR). There is a good linear correlation between FunMass INP and Br^--CIMS/Vocus-PTR INP found for single experiment days. However, the correlation coefficient varies during the campaign period by a maximum factor of 5 and 10 for Br^--CIMS and Vocus-PTR INP, respectively, which may result from the influence of aerosols in the sampling procedure, instrumental drifts or the selectivity of the ionisation schemes. For now which measurement is more affected by the mentioned problems is left open.

FunMass deployed under challenging conditions during the two campaigns has shown to be a very valuable new tool for versatile measurements of trace gases involved in complicated atmospheric chemical and dynamic processes. The data obtained for HNO_3 and HCN in the Asian Monsoon region as well as HNO_3 and organic nitrates production studied in the SAPHIR chamber allow for interesting studies on relevant underlying atmospheric processes, some of which have been presented and discussed in this work.

6.2 Perspectives

In addition to the results derived from the FunMass data and presented in this work there are some issues to be further refined and analysed in the future.

1. An extensive study on other tropospheric and stratospheric originated trace gases measured during the StratoClim Campaign, which have not yet been available, should be considered to consolidate or refine the results on the convective outflow layer and the structure of the TOC layer.

2. More efforts should be made to enable detailed dynamical and chemical model studies of the observed HCN and especially HNO_3 structures in the UTLS. This may give more insights especially on the convective *vs.* lightning origin of the observed HNO_3 enhancements observed early in flight F6.

3. More interesting chemical species can probably be extracted from the mass spectra recorded by FunMass during StratoClim, such as isocyanic acid (HNCO) which was recently identified and also mainly originates from biomass/biofuel burning.

4. More efforts can be made based on the chamber HNO_3 measurements to more systematically study the wall effects and uptake coefficient of HNO_3 by aerosols. The observed varying correlations for the detection of the organic nitrates by different CIMS techniques should be urgently revealed.

Although FunMass has performed quite well during the deployments the following issues can be improved for upcoming measurement activities:

1. The new concentric-DBD ion source produces high reagent ion concentrations. However, highly reactive radical species that can react with some analytes are also produced, therefore enhancing or reducing the respective mass peaks and causing possible qualitative as well as quantitative artefacts. Consequently, the output of such interfering species should be minimized or suppressed by some radical scavengers.

2. The tested and calibrated I^- ionisation mode should finally be deployed for upcoming measurements as it may enable the detection of even more interesting species. Other ionization modes can also be further realised.

3. The detection of organic nitrates can be improved by establishing a suitable way to calibrate these species. By optimizing the transfer stage settings of FunMass the detection limit of organic nitrate species may be improved, enabling the detection of more such species as well.

4. FunMass is build to carry out airborne measurements onboard of M55-Geophysica where future deployments unfortunately are quite uncertain. Therefore the integration and deployment onboard alternate platforms, *e.g.* the High Altitude and Long Range Research Aircraft (HALO), should be further pursued. Further deployments for chamber or even ground-based ambient measurements should be explored and possibly achieved.

Bibliography

[1] S. K. Akagi et al., Emission factors for open and domestic biomass burning for use in atmospheric models, *Atmospheric Chemistry and Physics* 11.9 (2011), pp. 4039–4072, DOI: `10.5194/acp-11-4039-2011`.

[2] S. Albrecht, Development of a highly sensitive and versatile mass spectrometer system for laboratory and atmospheric measurements, PhD thesis, University of Wuppertal, 2014.

[3] S. R. Albrecht et al., Measurements of hydroperoxy radicals (HO_2) at atmospheric concentrations using bromide chemical ionisation mass spectrometry, *Atmospheric Measurement Techniques* 12.2 (2019), pp. 891–902, DOI: `10.5194/amt-12-891-2019`.

[4] D. Aljawhary, A. K. Y. Lee, and J. P. D. Abbatt, High-resolution chemical ionization mass spectrometry (ToF-CIMS): application to study SOA composition and processing, *Atmospheric Measurement Techniques* 6.11 (2013), pp. 3211–3224, DOI: `10.5194/amt-6-3211-2013`.

[5] M. O. Andreae, Emission of trace gases and aerosols from biomass burning – an updated assessment, *Atmospheric Chemistry and Physics* 19.13 (2019), pp. 8523–8546, DOI: `10.5194/acp-19-8523-2019`.

[6] R. Atkinson et al., Evaluated kinetic and photochemical data for atmospheric chemistry: Volume II – gas phase reactions of organic species, *Atmospheric Chemistry and Physics* 6.11 (2006), pp. 3625–4055, DOI: `10.5194/acp-6-3625-2006`.

[7] R. Atkinson, Atmospheric chemistry of VOCs and NO_x, *Atmospheric Environment* 34.12 (2000), pp. 2063 –2101, DOI: `https://doi.org/10.1016/S1352-2310(99)00460-4`.

[8] R. Atkinson and J. Arey, Atmospheric Degradation of Volatile Organic Compounds, *Chemical Reviews* 103.12 (2003), pp. 4605–4638, DOI: `10.1021/cr0206420`.

[9] T. Berndt, Rapid Formation of Sulfuric Acid Particles at Near-Atmospheric Conditions, *Science* 307.5710 (2005), pp. 698–700, DOI: `10.1126/science.1104054`.

[10] J. Bowermaster and R. W. Shaw, A Source of Gaseous HNO_3 and Its Transmission Efficiency through Various Materials, *Journal of the Air Pollution Control Association* 31.7 (1981), pp. 787–820, DOI: `10.1080/00022470.1981.10465279`.

[11] S. S. Brown et al., Nocturnal isoprene oxidation over the Northeast United States in summer and its impact on reactive nitrogen partitioning and secondary organic aerosol, *Atmospheric Chemistry and Physics* 9.9 (2009), pp. 3027–3042, DOI: `10.5194/acp-9-3027-2009`.

[12] S. Brown, H. Stark, and A. Ravishankara, Cavity ring-down spectroscopy for atmospheric trace gas detection: application to the nitrate radical (NO_3), *Applied Physics B* 75.2 (2002), pp. 173–182, DOI: `10.1007/s00340-002-0980-y`.

[13] S. S. Brown and J. Stutz, Nighttime radical observations and chemistry, *Chemical Society Reviews* 41.19 (2012), p. 6405, DOI: `10.1039/c2cs35181a`.

[14] S. S. Brown et al., Simultaneousin situdetection of atmospheric NO_3 and N_2O_5 via cavity ring-down spectroscopy, *Review of Scientific Instruments* 73.9 (2002), pp. 3291–3301, DOI: 10.1063/1.1499214.

[15] S. Brunamonti et al., Balloon-borne measurements of temperature, water vapor, ozone and aerosol backscatter on the southern slopes of the Himalayas during StratoClim 2016–2017, *Atmospheric Chemistry and Physics* 18.21 (2018), pp. 15937–15957, DOI: 10.5194/acp-18-15937-2018.

[16] S. Bucci et al., Deep convective influence on the UTLS composition in the Asian Monsoon Anticyclone region: 2017 StratoClim campaign results (2020), DOI: 10.5194/acp-2019-1053.

[17] F. Cairo et al., An overview of the SCOUT-AMMA stratospheric aircraft, balloons and sondes campaign in West Africa, August 2006: rationale, roadmap and highlights, *Atmospheric Chemistry and Physics Discussions* 9.5 (2009), pp. 19713–19781, DOI: 10.5194/acpd-9-19713-2009.

[18] C. D. Cappa and M. J. Elrod, A computational investigation of the electron affinity of CO_3 and the thermodynamic feasibility of $CO_3^-(H_2O)_n$ROOH reactions, *Physical Chemistry Chemical Physics* 3.15 (2001), pp. 2986–2994, DOI: 10.1039/b102981a.

[19] A. G. Carlton, C. Wiedinmyer, and J. H. Kroll, A review of Secondary Organic Aerosol (SOA) formation from isoprene, *Atmospheric Chemistry and Physics* 9.14 (2009), pp. 4987–5005, DOI: 10.5194/acp-9-4987-2009.

[20] C. Clerbaux et al., CO measurements from the ACE-FTS satellite instrument: data analysis and validation using ground-based, airborne and spaceborne observations, *Atmospheric Chemistry and Physics* 8.9 (2008), pp. 2569–2594, DOI: 10.5194/acp-8-2569-2008.

[21] P. Connell and H. S. Johnston, The thermal dissociation of N_2O_5 in N_2, *Geophysical Research Letters* 6.7 (1979), pp. 553–556, DOI: 10.1029/gl006i007p00553.

[22] S. S. Das et al., Upper tropospheric ozone transport from the sub-tropics to tropics over the Indian region during Asian summer monsoon, *Climate Dynamics* 52.7-8 (2018), pp. 4567–4581, DOI: 10.1007/s00382-018-4418-6.

[23] P. F. DeCarlo et al., Field-Deployable, High-Resolution, Time-of-Flight Aerosol Mass Spectrometer, *Analytical Chemistry* 78.24 (2006), pp. 8281–8289, DOI: 10.1021/ac061249n.

[24] D. P. Dee et al., The ERA-Interim reanalysis: configuration and performance of the data assimilation system, *Quarterly Journal of the Royal Meteorological Society* 137.656 (2011), pp. 553–597, DOI: 10.1002/qj.828.

[25] M. Derrien, H. L. Gléau, and M Raoul, "The use of the high resolution visible in SAFNWC/MSG cloud mask", 2010.

[26] H.-P. Dorn et al., Intercomparison of NO_3 radical detection instruments in the atmosphere simulation chamber SAPHIR, *Atmospheric Measurement Techniques* 6.5 (2013), pp. 1111–1140, DOI: 10.5194/amt-6-1111-2013.

[27] E. S. Edgerton et al., The Southeastern Aerosol Research and Characterization Study: Part II. Filter-Based Measurements of Fine and Coarse Particulate Matter Mass and Composition, *Journal of the Air & Waste Management Association* 55.10 (2005), pp. 1527–1542, DOI: 10.1080/10473289.2005.10464744.

[28] F. L. Eisele and D. J. Tanner, Ion-assisted tropospheric OH measurements, *Journal of Geophysical Research* 96.D5 (1991), p. 9295, DOI: 10.1029/91jd00198.

[29] L. K. Emmons et al., Validation of Measurements of Pollution in the Troposphere (MOPITT) CO retrievals with aircraft in situ profiles, *Journal of Geophysical Research: Atmospheres* 109.D3 (2004), n/a–n/a, DOI: `10.1029/2003jd004101`.

[30] S. Fadnavis et al., Transport of aerosols into the UTLS and their impact on the Asian monsoon region as seen in a global model simulation, *Atmospheric Chemistry and Physics* 13.17 (2013), pp. 8771–8786, DOI: `10.5194/acp-13-8771-2013`.

[31] S. Fadnavis et al., Trends in peroxyacetyl nitrate (PAN) in the upper troposphere and lower stratosphere over southern Asia during the summer monsoon season: regional impacts, *Atmospheric Chemistry and Physics* 14.23 (2014), pp. 12725–12743, DOI: `10.5194/acp-14-12725-2014`.

[32] R. D. Field et al., Indonesian fire activity and smoke pollution in 2015 show persistent nonlinear sensitivity to El Niño-induced drought, *Proceedings of the National Academy of Sciences* 113.33 (2016), pp. 9204–9209, DOI: `10.1073/pnas.1524888113`.

[33] V. E. Fioletov et al., A global catalogue of large SO_2 sources and emissions derived from the Ozone Monitoring Instrument, *Atmospheric Chemistry and Physics* 16.18 (2016), pp. 11497–11519, DOI: `10.5194/acp-16-11497-2016`.

[34] H. J. L. Forstner, R. C. Flagan, and J. H. Seinfeld, Secondary Organic Aerosol from the Photooxidation of Aromatic Hydrocarbons: Molecular Composition, *Environmental Science & Technology* 31.5 (1997), pp. 1345–1358, DOI: `10.1021/es9605376`.

[35] J. L. Fry et al., Organic nitrate and secondary organic aerosol yield from NO_3 oxidation of $beta$-pinene evaluated using a gas-phase kinetics/aerosol partitioning model, *Atmospheric Chemistry and Physics* 9.4 (2009), pp. 1431–1449, DOI: `10.5194/acp-9-1431-2009`.

[36] H. Fuchs et al., Intercomparison of measurements of NO_2 concentrations in the atmosphere simulation chamber SAPHIR during the NO_3Comp campaign, *Atmospheric Measurement Techniques* 3.1 (2010), pp. 21–37, DOI: `10.5194/amt-3-21-2010`.

[37] H. Garny and W. J. Randel, Transport pathways from the Asian monsoon anticyclone to the stratosphere, *Atmospheric Chemistry and Physics* 16.4 (2016), pp. 2703–2718, DOI: `10.5194/acp-16-2703-2016`.

[38] N. Glatthor et al., Large-scale upper tropospheric pollution observed by MIPAS HCN and C_2H_6 global distributions, *Atmospheric Chemistry and Physics* 9.24 (2009), pp. 9619–9634, DOI: `10.5194/acp-9-9619-2009`.

[39] N. Glatthor et al., Seasonal and interannual variations in HCN amounts in the upper troposphere and lower stratosphere observed by MIPAS, *Atmospheric Chemistry and Physics* 15.2 (2015), pp. 563–582, DOI: `10.5194/acp-15-563-2015`.

[40] P. D. Goldan et al., Calibration and tests of the filter-collection method for measuring clean-air, ambient levels of nitric acid, *Atmospheric Environment (1967)* 17.7 (1983), pp. 1355–1364, DOI: `10.1016/0004-6981(83)90410-9`.

[41] B Gravendeel and F. J. de Hoog, Clustered negative ions in atmospheric negative corona discharges in the Trichel regime, *Journal of Physics B: Atomic and Molecular Physics* 20.23 (1987), pp. 6337–6361, DOI: `10.1088/0022-3700/20/23/025`.

[42] C. R. Greene and R. Atkinson, Rate constants for the gas-phase reactions of O_3 with a series of alkenes at 296 ± 2 K, *International Journal of Chemical Kinetics* 24.9 (1992), pp. 803–811, DOI: `10.1002/kin.550240905`.

[43] J. H. Gross, *Mass Spectrometry*, Springer Berlin Heidelberg, 2011, DOI: `10.1007/978-3-642-10711-5`.

[44] A. Guenther et al., A global model of natural volatile organic compound emissions, *Journal of Geophysical Research* 100.D5 (1995), p. 8873, DOI: `10.1029/94jd02950`.

[45] M. Hanke et al., Atmospheric measurements of gas-phase HNO_3 and SO_2 using chemical ionization mass spectrometry during the MINATROC field campaign 2000 on Monte Cimone, *Atmospheric Chemistry and Physics* 3.2 (2003), pp. 417–436, DOI: `10.5194/acp-3-417-2003`.

[46] G. W. Harris et al., Observations of nitrous acid in the Los Angeles atmosphere and implications for predictions of ozone-precursor relationships, *Environmental Science & Technology* 16.7 (1982), pp. 414–419, DOI: `10.1021/es00101a009`.

[47] J. J. Harrison, C. D. Boone, and P. F. Bernath, New and improved infra-red absorption cross sections and ACE-FTS retrievals of carbon tetrachloride (CCl_4), *Journal of Quantitative Spectroscopy and Radiative Transfer* 186 (2017), pp. 139–149, DOI: `10.1016/j.jqsrt.2016.04.025`.

[48] M. R. Heal, P. Kumar, and R. M. Harrison, Particles, air quality, policy and health, *Chemical Society Reviews* 41.19 (2012), p. 6606, DOI: `10.1039/c2cs35076a`.

[49] M. I. Hegglin et al., A global view of the extratropical tropopause transition layer from Atmospheric Chemistry Experiment Fourier Transform Spectrometer O_3, H_2O, and CO, *Journal of Geophysical Research* 114 (2009), DOI: `10.1029/2008jd009984`.

[50] D. K. Henze et al., Global modeling of secondary organic aerosol formation from aromatic hydrocarbons: high- vs. low-yield pathways, *Atmospheric Chemistry and Physics* 8.9 (2008), pp. 2405–2420, DOI: `10.5194/acp-8-2405-2008`.

[51] M. von Hobe, F. Stroh, and N. Spelten, A compact low-cost permeation oven (In preparation).

[52] M. von Hobe et al., Reconciliation of essential process parameters for an enhanced predictability of Arctic stratospheric ozone loss and its climate interactions (RECONCILE): activities and results, *Atmospheric Chemistry and Physics* 13.18 (2013), pp. 9233–9268, DOI: `10.5194/acp-13-9233-2013`.

[53] M. von Hobe et al., Transport pathways in the Asian monsoon UTLS inferred from (STRATOCLIM) trace gas observations, *Atmospheric Chemistry and Physics* (In preparation).

[54] P. Hoor et al., Seasonality and extent of extratropical TST derived from in-situ CO measurements during SPURT, *Atmospheric Chemistry and Physics* 4.5 (2004), pp. 1427–1442, DOI: `10.5194/acp-4-1427-2004`.

[55] M. Höpfner et al., Ammonium nitrate particles formed in upper troposphere from ground ammonia sources during Asian monsoons, *Nature Geoscience* 12.8 (2019), pp. 608–612, DOI: `10.1038/s41561-019-0385-8`.

[56] L. G. Huey, Measurement of trace atmospheric species by chemical ionization mass spectrometry: Speciation of reactive nitrogen and future directions, *Mass Spectrom. Rev.* 26.2 (2007), pp. 166–184.

[57] L. G. Huey et al., Fast time response measurements of HNO_3 in air with a chemical ionization mass spectrometer, *J. Geophys. Res.* 103.D3 (1998), pp. 3355–3360.

[58] L. Huey et al., CIMS measurements of HNO_3 and SO_2 at the South Pole during ISCAT 2000, *Atmospheric Environment* 38.32 (2004), pp. 5411–5421, DOI: `10.1016/j.atmosenv.2004.04.037`.

[59] J. H. Jiang et al., An assessment of upper troposphere and lower stratosphere water vapor in MERRA, MERRA2, and ECMWF reanalyses using Aura MLS observations, *Journal of Geophysical Research: Atmospheres* 120.22 (2015), pp. 11,468–11,485, DOI: `10.1002/2015jd023752`.

[60] H. Junninen et al., A high-resolution mass spectrometer to measure atmospheric ion composition, *Atmospheric Measurement Techniques* 3.4 (2010), pp. 1039–1053, DOI: `10.5194/amt-3-1039-2010`.

[61] T. Jurkat et al., A quantitative analysis of stratospheric HCl, HNO_3, and O_3 in the tropopause region near the subtropical jet, *Geophysical Research Letters* 41.9 (2014), pp. 3315–3321, DOI: `10.1002/2013gl059159`.

[62] T. Jurkat et al., The airborne mass spectrometer AIMS – Part 2: Measurements of trace gases with stratospheric or tropospheric origin in the UTLS, *Atmospheric Measurement Techniques* 9.4 (2016), pp. 1907–1923, DOI: `10.5194/amt-9-1907-2016`.

[63] F. Kaemmerer, Chemical Ionisation Mass Spectrometery with a Time of Flight detector (CIMS-TOF) measurements in support of the calibration of the airborne "FunMass" instrument, MA thesis, Fachhochshule Aachen, 2018.

[64] T. Khattatov, Development, calibration and deployment of an airborne chemical ionization mass spectrometer fpr trace gas measurements, PhD thesis, University of Wuppertal, 2019.

[65] K. Kita et al., A Chemical Ionization Mass Spectrometer for Ground-Based Measurements of Nitric Acid, *Journal of Atmospheric and Oceanic Technology* 23.8 (2006), pp. 1104–1113, DOI: `10.1175/JTECH1900.1`, eprint: `https://doi.org/10.1175/JTECH1900.1`.

[66] L. I. Kleinman et al., Ozone production rate and hydrocarbon reactivity in 5 urban areas: A cause of high ozone concentration in Houston, *Geophysical Research Letters* 29.10 (2002), pp. 105–1–105–4, DOI: `10.1029/2001gl014569`.

[67] G. Knop and F. Arnold, Stratospheric trace gas detection using a new balloon-borne ACIMS method: Acetonitrile, acetone, and nitric acid, *Geophysical Research Letters* 14.12 (1987), pp. 1262–1265, DOI: `10.1029/gl014i012p01262`.

[68] P. Konopka et al., Annual cycle of ozone at and above the tropical tropopause: observations versus simulations with the Chemical Lagrangian Model of the Stratosphere (CLaMS), *Atmospheric Chemistry and Physics* 10.1 (2010), pp. 121–132, DOI: `10.5194/acp-10-121-2010`.

[69] P. Konopka, F. Ploeger, and R. Müller, "Entropy-Based and Static Stability-Based Lagrangian Model Grids", *Lagrangian Modeling of the Atmosphere*, American Geophysical Union, 2013, pp. 99–110, DOI: `10.1029/2012gm001253`.

[70] J.-H. Koo et al., Global climatology based on the ACE-FTS version 3.5 dataset: Addition of mesospheric levels and carbon-containing species in the UTLS, *Journal of Quantitative Spectroscopy and Radiative Transfer* 186 (2017), pp. 52–62, DOI: `10.1016/j.jqsrt.2016.07.003`.

[71] B. Kärcher and C. Voigt, Formation of nitric acid/water ice particles in cirrus clouds, *Geophysical Research Letters* 33.8 (2006), DOI: `10.1029/2006gl025927`.

[72] A. J. Kwan et al., Peroxy radical chemistry and OH radical production during the NO_3-initiated oxidation of isoprene, *Atmospheric Chemistry and Physics* 12.16 (2012), pp. 7499–7515, DOI: `10.5194/acp-12-7499-2012`.

[73] S. M. L. et al., A comprehensive overview of the climatological composition of the Asian summer monsoon anticyclone based on 10 years of Aura Microwave Limb Sounder measurements, *Journal of Geophysical Research: Atmospheres* 122.10 (2017), pp. 5491–5514, DOI: `10.1002/2016JD026408`, eprint: `https://agupubs.onlinelibrary.wiley.com/doi/pdf/10.1002/2016JD026408`.

[74] L. J. Labrador, R. von Kuhlmann, and M. G. Lawrence, The effects of lightning-produced NO_x and its vertical distribution on atmospheric chemistry: sensitivity simulations with MATCH-MPIC, *Atmospheric Chemistry and Physics* 5.7 (2005), pp. 1815–1834, DOI: `10.5194/acp-5-1815-2005`.

[75] B. H. Lee et al., An Iodide-Adduct High-Resolution Time-of-Flight Chemical-Ionization Mass Spectrometer: Application to Atmospheric Inorganic and Organic Compounds, *Environmental Science & Technology* 48.11 (2014), pp. 6309–6317, DOI: `10.1021/es500362a`.

[76] B. H. Lee et al., Flight Deployment of a High-Resolution Time-of-Flight Chemical Ionization Mass Spectrometer: Observations of Reactive Halogen and Nitrogen Oxide Species, *Journal of Geophysical Research: Atmospheres* (2018), DOI: `10.1029/2017jd028082`.

[77] B. H. Lee et al., Highly functionalized organic nitrates in the southeast United States: Contribution to secondary organic aerosol and reactive nitrogen budgets, *Proceedings of the National Academy of Sciences* 113.6 (2016), pp. 1516–1521, DOI: `10.1073/pnas.1508108113`.

[78] K.-O. Lee et al., Convective hydration in the tropical tropopause layer during the StratoClim aircraft campaign: pathway of an observed hydration patch, *Atmospheric Chemistry and Physics* 19.18 (2019), pp. 11803–11820, DOI: `10.5194/acp-19-11803-2019`.

[79] J. Lelieveld et al., Atmospheric oxidation capacity sustained by a tropical forest, *Nature* 452 (Apr. 2008), p. 737.

[80] Q. Li et al., What drives the observed variability of HCN in the troposphere and lower stratosphere?, *Atmospheric Chemistry and Physics* 9.21 (2009), pp. 8531–8543, DOI: `10.5194/acp-9-8531-2009`.

[81] Q. Li et al., A global three-dimensional model analysis of the atmospheric budgets of HCN and CH_3SCN: Constraints from aircraft and ground measurements, *Journal of Geophysical Research: Atmospheres* 108.D21 (2003), DOI: `10.1029/2002jd003075`.

[82] Q. Li et al., Atmospheric hydrogen cyanide (HCN): Biomass burning source, ocean sink?, *Geophysical Research Letters* 27.3 (2000), pp. 357–360, DOI: `10.1029/1999gl010935`.

[83] Z. Li et al., Aerosol and monsoon climate interactions over Asia, *Reviews of Geophysics* 54.4 (2016), pp. 866–929, DOI: `10.1002/2015rg000500`.

[84] L. Liu et al., The role of nitric acid in atmospheric new particle formation, *Physical Chemistry Chemical Physics* 20.25 (2018), pp. 17406–17414, DOI: `10.1039/c8cp02719f`.

[85] N. J. Livesey et al., *Version 4.2x Level 2 data quality and description document*, tech. rep., Jet Propulsion Lab, 2017.

[86] F. D. Lopez-Hilfiker et al., A novel method for online analysis of gas and particle composition: description and evaluation of a Filter Inlet for Gases and AEROsols (FIGAERO), *Atmospheric Measurement Techniques* 7.4 (2014), pp. 983–1001, DOI: `10.5194/amt-7-983-2014`.

[87] T. Marcy et al., Measurements of trace gases in the tropical tropopause layer, *Atmospheric Environment* 41.34 (2007), pp. 7253–7261, DOI: `10.1016/j.atmosenv.2007.05.032`.

[88] R. V. Martin et al., Space-based constraints on the production of nitric oxide by lightning, *Journal of Geophysical Research* 112.D9 (2007), DOI: `10.1029/2006jd007831`.

[89] D. S. McKenna, A new Chemical Lagrangian Model of the Stratosphere (CLaMS) 1. Formulation of advection and mixing, *Journal of Geophysical Research* 107.D16 (2002), DOI: `10.1029/2000jd000114`.

[90] D. S. McKenna, A new Chemical Lagrangian Model of the Stratosphere (CLaMS) 2. Formulation of chemistry scheme and initialization, *Journal of Geophysical Research* 107.D15 (2002), DOI: `10.1029/2000jd000113`.

[91] H. McKenzie et al., Modelling of Nitric and Nitrous Acid Chemistry for Solvent Extraction Purposes, *Procedia Chemistry* 21 (2016), pp. 481–486, DOI: `10.1016/j.proche.2016.10.067`.

[92] O. Möhler and F. Arnold, Gaseous Sulfuric Acid and Sulfur Dioxide Measurements in the Arctic Troposphere and Lower Stratosphere: Implications for Hydroxyl Radical Abundances, *Berichte der Bunsengesellschaft für physikalische Chemie* 96.3 (1992), pp. 280–283, DOI: `10.1002/bbpc.19920960310`.

[93] O. Möhler, T. Reiner, and F. Arnold, A novel aircraft-based tandem mass spectrometer for atmospheric ion and trace gas measurements, *Review of Scientific Instruments* 64.5 (1993), pp. 1199–1207, DOI: `10.1063/1.1144455`.

[94] R. Müller, *Tracer-tracer Relations as a Tool for Research on Polar Ozone Loss*, vol. 58, Forschungszentrum Juelich GmbH, 2010.

[95] O. Möhler and F. Arnold, Flow reactor and triple quadrupole mass spectrometer investigations of negative ion reactions involving nitric acid: Implications for atmospheric HNO_3 detection by chemical ionization mass spectrometry, *Journal of Atmospheric Chemistry* 13.1 (1991), pp. 33–61, DOI: `10.1007/BF00048099`.

[96] S. Müller et al., Impact of the Asian monsoon on the extratropical lower stratosphere: trace gas observations during TACTS over Europe 2012, *Atmospheric Chemistry and Physics* 16.16 (2016), pp. 10573–10589, DOI: `10.5194/acp-16-10573-2016`.

[97] N. Nechita-Banda et al., Monitoring emissions from the 2015 Indonesian fires using CO satellite data, *Philosophical Transactions of the Royal Society B: Biological Sciences* 373.1760 (2018), p. 20170307, DOI: `10.1098/rstb.2017.0307`.

[98] J. A. Neuman et al., Study of Inlet Materials for Sampling Atmospheric Nitric Acid, *Environmental Science & Technology* 33.7 (1999), pp. 1133–1136, DOI: `10.1021/es980767f`.

[99] N. L. Ng et al., Secondary organic aerosol (SOA) formation from reaction of isoprene with nitrate radicals (NO_3), *Atmospheric Chemistry and Physics* 8.14 (2008), pp. 4117–4140, DOI: `10.5194/acp-8-4117-2008`.

[100] P. C. Novelli, K. A. Masarie, and P. M. Lang, Distributions and recent changes of carbon monoxide in the lower troposphere, *Journal of Geophysical Research: Atmospheres* 103.D15 (1998), pp. 19015–19033, DOI: `10.1029/98jd01366`.

[101] L. L. Pan et al., Transport of chemical tracers from the boundary layer to stratosphere associated with the dynamics of the Asian summer monsoon, *Journal of Geophysical Research: Atmospheres* 121.23 (2016), pp. 14,159–14,174, DOI: `10.1002/2016JD025616`, eprint: `https://agupubs.onlinelibrary.wiley.com/doi/pdf/10.1002/2016JD025616`.

[102] M. Park et al., Chemical isolation in the Asian monsoon anticyclone observed in Atmospheric Chemistry Experiment (ACE-FTS) data, *Atmospheric Chemistry and Physics* 8.3 (2008), pp. 757–764, DOI: `10.5194/acp-8-757-2008`.

[103] M. Park et al., Transport pathways of carbon monoxide in the Asian summer monsoon diagnosed from Model of Ozone and Related Tracers (MOZART), *Journal of Geophysical Research* 114.D8 (2009), DOI: `10.1029/2008jd010621`.

[104] F. Paulot et al., Isoprene photooxidation: new insights into the production of acids and organic nitrates, *Atmospheric Chemistry and Physics* 9.4 (2009), pp. 1479–1501, DOI: `10.5194/acp-9-1479-2009`.

[105] A. E. Perring et al., A product study of the isoprene+NO_3 reaction, *Atmospheric Chemistry and Physics* 9.14 (2009), pp. 4945–4956, DOI: `10.5194/acp-9-4945-2009`.

[106] I. Pisso and B. Legras, Turbulent vertical diffusivity in the sub-tropical stratosphere, *Atmospheric Chemistry and Physics* 8.3 (2008), pp. 697–707, DOI: `10.5194/acp-8-697-2008`.

[107] F. Ploeger et al., Quantifying the effects of mixing and residual circulation on trends of stratospheric mean age of air, *Geophysical Research Letters* 42.6 (2015), pp. 2047–2054, DOI: `10.1002/2014gl062927`.

[108] F. Ploeger et al., Variability of stratospheric mean age of air and of the local effects of residual circulation and eddy mixing, *Journal of Geophysical Research: Atmospheres* 120.2 (2015), pp. 716–733, DOI: `10.1002/2014jd022468`.

[109] F. Ploeger and T. Birner, Seasonal and inter-annual variability of lower stratospheric age of air spectra, *Atmospheric Chemistry and Physics* 16.15 (2016), pp. 10195–10213, DOI: `10.5194/acp-16-10195-2016`.

[110] R. Pommrich et al., Tropical troposphere to stratosphere transport of carbon monoxide and long-lived trace species in the Chemical Lagrangian Model of the Stratosphere (CLaMS), *Geoscientific Model Development* 7.6 (2014), pp. 2895–2916, DOI: `10.5194/gmd-7-2895-2014`.

[111] R. Pommrich et al., What causes the irregular cycle of the atmospheric tape recorder signal in HCN?, *Geophysical Research Letters* 37.16 (2010), p. L16805, DOI: `10.1029/2010gl044056`.

[112] J. M. Popovic and R. A. Plumb, Eddy Shedding from the Upper-Tropospheric Asian Monsoon Anticyclone, *Journal of the Atmospheric Sciences* 58.1 (2001), pp. 93–104, DOI: `10.1175/1520-0469(2001)058<0093:esftut>2.0.co;2`.

[113] P. J. Popp et al., Stratospheric correlation between nitric acid and ozone, *Journal of Geophysical Research* 114.D3 (2009), DOI: `10.1029/2008jd010875`.

[114] W. J. Randel et al., Asian Monsoon Transport of Pollution to the Stratosphere, *Science* 328.5978 (2010), pp. 611–613, DOI: `10.1126/science.1182274`, eprint: `http://science.sciencemag.org/content/328/5978/611.full.pdf`.

[115] M. Rautenhaus, G. Bauer, and A. Dörnbrack, A web service based tool to plan atmospheric research flights, *Geoscientific Model Development* 5.1 (2012), pp. 55–71, DOI: `10.5194/gmd-5-55-2012`.

[116] J. M. Roberts et al., Measurement of HONO, HNCO, and other inorganic acids by negative-ion proton-transfer chemical-ionization mass spectrometry (NI-PT-CIMS): application to biomass burning emissions, *Atmospheric Measurement Techniques* 3.4 (2010), pp. 981–990, DOI: `10.5194/amt-3-981-2010`.

[117] G. D. Robertson, D. M. Mason, and W. H. Corcoran, The Kinetics of the Thermal Decomposition of Nitric Acid in the Liquid Phase, *The Journal of Physical Chemistry* 59.8 (1955), pp. 683–690, DOI: `10.1021/j150530a004`.

[118] F. Rohrer et al., Characterisation of the photolytic HONO-source in the atmosphere simulation chamber SAPHIR, *Atmospheric Chemistry and Physics* 5.8 (2005), pp. 2189–2201, DOI: `10.5194/acp-5-2189-2005`.

[119] F. Rohrer and H. Berresheim, Strong correlation between levels of tropospheric hydroxyl radicals and solar ultraviolet radiation, *Nature* 442.7099 (2006), pp. 184–187, DOI: `10.1038/nature04924`.

[120] A. W. Rollins et al., Isoprene oxidation by nitrate radical: alkyl nitrate and secondary organic aerosol yields, *Atmospheric Chemistry and Physics* 9.18 (2009), pp. 6685–6703, DOI: `10.5194/acp-9-6685-2009`.

[121] S. Romakkaniemi et al., The influence of nitric acid on the cloud processing of aerosol particles, *Atmospheric Chemistry and Physics* 6.6 (2006), pp. 1627–1634, DOI: `10.5194/acp-6-1627-2006`.

[122] M. Sabo et al., Atmospheric Pressure Corona Discharge Ionisation and Ion Mobility Spectrometry/Mass Spectrometry study of the negative corona discharge in high purity oxygen and oxygen/nitrogen mixtures, *International Journal of Mass Spectrometry* 293.1-3 (2010), pp. 23–27, DOI: `10.1016/j.ijms.2010.03.004`.

[123] M. L. Santee et al., Validation of the Aura Microwave Limb Sounder HNO_3 measurements, *Journal of Geophysical Research* 112.D24 (2007), DOI: `10.1029/2007jd008721`.

[124] E. Schlosser et al., Intercomparison of Two Hydroxyl Radical Measurement Techniques at the Atmosphere Simulation Chamber SAPHIR, *Journal of Atmospheric Chemistry* 56.2 (2007), pp. 187–205, DOI: `10.1007/s10874-006-9049-3`.

[125] J. Schneider et al., Nitric acid (HNO_3) in the upper troposphere and lower stratosphere at midlatitudes: New results from aircraft-based mass spectrometric measurements, *Journal of Geophysical Research: Atmospheres* 103.D19 (1998), pp. 25337–25343, DOI: `10.1029/98jd02240`.

[126] J. Schulz et al., Operational climate monitoring from space: the EUMETSAT Satellite Application Facility on Climate Monitoring (CM-SAF), *Atmospheric Chemistry and Physics* 9.5 (2009), pp. 1687–1709, DOI: `10.5194/acp-9-1687-2009`.

[127] R. H. Schwantes et al., Isoprene NO_3 Oxidation Products from the RO_2 + HO_2 Pathway, *The Journal of Physical Chemistry A* 119.40 (2015), PMID: 26335780, pp. 10158–10171, DOI: `10.1021/acs.jpca.5b06355`, eprint: `https://doi.org/10.1021/acs.jpca.5b06355`.

[128] P. E. Sheese, K. A. Walker, and C. D. Boone, A global enhancement of hydrogen cyanide in the lower stratosphere throughout 2016, *Geophysical Research Letters* 44.11 (2017), pp. 5791–5797, DOI: `10.1002/2017gl073519`.

[129] P. E. Sheese et al., ACE-FTS ozone, water vapour, nitrous oxide, nitric acid, and carbon monoxide profile comparisons with MIPAS and MLS, *Journal of Quantitative Spectroscopy and Radiative Transfer* 186 (2017), pp. 63–80, DOI: `10.1016/j.jqsrt.2016.06.026`.

[130] A. Stohl et al., Technical note: The Lagrangian particle dispersion model FLEXPART version 6.2, *Atmospheric Chemistry and Physics* 5.9 (2005), pp. 2461–2474, DOI: `10.5194/acp-5-2461-2005`.

[131] D. Stone, L. K. Whalley, and D. E. Heard, Tropospheric OH and HO_2 radicals: field measurements and model comparisons, *Chemical Society Reviews* 41.19 (2012), p. 6348, DOI: `10.1039/c2cs35140d`.

[132] J. Stutz et al., UV-visible absorption cross sections of nitrous acid, *Journal of Geophysical Research: Atmospheres* 105.D11 (2000), pp. 14585–14592, DOI: `10.1029/2000jd900003`.

[133] J. A. Thornton, Ozone production rates as a function of NO_x abundances and HO_x production rates in the Nashville urban plume, *Journal of Geophysical Research* 107.D12 (2002), DOI: `10.1029/2001jd000932`.

[134] X. Tie et al., Effects of lightning on reactive nitrogen and nitrogen reservoir species in the troposphere, *Journal of Geophysical Research: Atmospheres* 106.D3 (2001), pp. 3167–3178, DOI: `10.1029/2000jd900565`.

[135] A.-S. Tissier and B. Legras, Convective sources of trajectories traversing the tropical tropopause layer, *Atmospheric Chemistry and Physics* 16.5 (2016), pp. 3383–3398, DOI: `10.5194/acp-16-3383-2016`.

[136] I. Tritscher et al., Lagrangian simulation of ice particles and resulting dehydration in the polar winter stratosphere, *Atmospheric Chemistry and Physics* 19.1 (2019), pp. 543–563, DOI: `10.5194/acp-19-543-2019`.

[137] P. Veres et al., Development of negative-ion proton-transfer chemical-ionization mass spectrometry (NI-PT-CIMS) for the measurement of gas-phase organic acids in the atmosphere, *International Journal of Mass Spectrometry* 274.1-3 (2008), pp. 48–55, DOI: `10.1016/j.ijms.2008.04.032`.

[138] P. Veres et al., Measurements of gas-phase inorganic and organic acids from biomass fires by negative-ion proton-transfer chemical-ionization mass spectrometry, *Journal of Geophysical Research* 115.D23 (2010), DOI: `10.1029/2010jd014033`.

[139] J.-P. Vernier, L. W. Thomason, and J. Kar, CALIPSO detection of an Asian tropopause aerosol layer, *Geophysical Research Letters* 38.7 (2011), DOI: `10.1029/2010gl046614`.

[140] S. Viciani et al., A cryogenically operated laser diode spectrometer for airborne measurement of stratospheric trace gases, *Applied Physics B* 90.3 (2008), pp. 581–592, DOI: `10.1007/s00340-007-2885-2`.

[141] J. Viidanoja, T. Reiner, and F. Arnold, Laboratory investigations of negative ion molecule reactions of formic and acetic acids: implications for atmospheric measurements by ion-molecule reaction mass spectrometry, *International Journal of Mass Spectrometry* 181.1-3 (1998), pp. 31–41, DOI: `10.1016/s1387-3806(98)14151-9`.

[142] B. Vogel et al., Fast transport from Southeast Asia boundary layer sources to northern Europe: rapid uplift in typhoons and eastward eddy shedding of the Asian monsoon anticyclone, *Atmospheric Chemistry and Physics* 14.23 (2014), pp. 12745–12762, DOI: `10.5194/acp-14-12745-2014`.

[143] B. Vogel et al., Impact of different Asian source regions on the composition of the Asian monsoon anticyclone and of the extratropical lowermost stratosphere, *Atmospheric Chemistry and Physics* 15.23 (2015), pp. 13699–13716, DOI: `10.5194/acp-15-13699-2015`.

[144] B. Vogel et al., Lagrangian simulations of the transport of young air masses to the top of the Asian monsoon anticyclone and into the tropical pipe, *Atmospheric Chemistry and Physics* 19.9 (2019), pp. 6007–6034, DOI: `10.5194/acp-19-6007-2019`.

[145] B. Vogel et al., Long-range transport pathways of tropospheric source gases originating in Asia into the northern lower stratosphere during the Asian monsoon season 2012, *Atmospheric Chemistry and Physics* 16.23 (2016), pp. 15301–15325, DOI: `10.5194/acp-16-15301-2016`.

[146] A. Wahner, T. F. Mentel, and M. Sohn, Gas-phase reaction of N_2O_5 with water vapor: Importance of heterogeneous hydrolysis of N_2O_5 and surface desorption of HNO_3 in a large Teflon chamber, *Geophysical Research Letters* 25.12 (1998), pp. 2169–2172, DOI: `10.1029/98gl51596`.

[147] A. Wahner et al., Heterogeneous reaction of N_2O_5 on sodium nitrate aerosol, *Journal of Geophysical Research: Atmospheres* 103.D23 (1998), pp. 31103–31112, DOI: `10.1029/1998jd100022`.

[148] J. Waters et al., The Earth observing system microwave limb sounder (EOS MLS) on the aura Satellite, *IEEE Transactions on Geoscience and Remote Sensing* 44.5 (2006), pp. 1075–1092, DOI: `10.1109/tgrs.2006.873771`.

[149] R. Wegener et al., Simulation chamber investigation of the reactions of ozone with short-chained alkenes, *Journal of Geophysical Research: Atmospheres* 112.D13 (2007), n/a–n/a, DOI: `10.1029/2006jd007531`.

[150] R. J. Wild et al., A Measurement of Total Reactive Nitrogen, NO_y, together with NO_2, NO, and O_3 via Cavity Ring-down Spectroscopy, *Environmental Science & Technology* 48.16 (2014), pp. 9609–9615, DOI: `10.1021/es501896w`.

[151] A. Wisthaler et al., Technical Note: Intercomparison of formaldehyde measurements at the atmosphere simulation chamber SAPHIR, *Atmospheric Chemistry and Physics* 8.8 (2008), pp. 2189–2200, DOI: `10.5194/acp-8-2189-2008`.

[152] X. Yan et al., The efficiency of transport into the stratosphere via the Asian and North American summer monsoon circulations, *Atmospheric Chemistry and Physics* 19.24 (2019), pp. 15629–15649, DOI: `10.5194/acp-19-15629-2019`.

[153] R. L. N. Yatavelli et al., A Chemical Ionization High-Resolution Time-of-Flight Mass Spectrometer Coupled to a Micro Orifice Volatilization Impactor (MOVI-HRToF-CIMS) for Analysis of Gas and Particle-Phase Organic Species, *Aerosol Science and Technology* 46.12 (2012), pp. 1313–1327, DOI: `10.1080/02786826.2012.712236`.

[154] K. Yu et al., Characterization of nighttime formation of particulate organic nitrates based on high-resolution aerosol mass spectrometry in an urban atmosphere in China, *Atmospheric Chemistry and Physics* 19.7 (2019), pp. 5235–5249, DOI: `10.5194/acp-19-5235-2019`.

[155] P. Yu et al., Composition and physical properties of the Asian Tropopause Aerosol Layer and the North American Tropospheric Aerosol Layer, *Geophysical Research Letters* 42.7 (2015), pp. 2540–2546, DOI: `10.1002/2015gl063181`.

[156] P. Yu et al., Efficient transport of tropospheric aerosol into the stratosphere via the Asian summer monsoon anticyclone, *Proceedings of the National Academy of Sciences* 114.27 (2017), pp. 6972–6977, DOI: `10.1073/pnas.1701170114`.

[157] L. N. Yurganov et al., Global AIRS and MOPITT CO measurements: Validation, comparison, and links to biomass burning variations and carbon cycle, *Journal of Geophysical Research* 113.D9 (2008), DOI: `10.1029/2007jd009229`.

[158] V. Yushkov et al., A Chemiluminescent Analyzer for Stratospheric Measurements of the Ozone Concentration (FOZAN), *Journal of Atmospheric and Oceanic Technology* 16.10 (1999), pp. 1345–1350, DOI: `10.1175/1520-0426(1999)016<1345:acafsm>2.0.co;2`.

[159] J. Zheng et al., Measurements of HNO_3 and N_2O_5 using ion drift-chemical ionization mass spectrometry during the MILAGRO/MCMA-2006 campaign, *Atmospheric Chemistry and Physics* 8.22 (2008), pp. 6823–6838, DOI: `10.5194/acp-8-6823-2008`.

Acknowledgements

First and foremost I would like to express my gratitude to my scientific advisor Dr. Fred Stroh for patiently guiding me throughout my doctorate study with his immense knowledge, experience and motivation from familiarizing me with the measuring technique to interpreting the results. I hope that I could be as lively, enthusiastic, energetic and creative as Fred for both life and work in the future.

Apart from my advisor, I would like to thank Prof. Dr. Thorsten Benter for giving me the opportunity to pursue my PhD under his supervision. I am also grateful to Prof. Dr. Martin Riese for providing me the chance to work in FZJ and being supportive for advancing my research work.

This dissertation would not have been possible without the research grant from the HITEC graduate school, which gave me the chance to further my career in Germany and experience the German culture. I am proud of being a part of the StratoClim community and involved in the aircraft campaigns. I also appreciate the cooperation with the colleagues from IEK-8 for the NO_3-isoprene campaign.

I would never forget Dr. Sascha Albrecht who developed the lab prototype of CI-ToF-MS and Dr. Talat Khattatov who developed FunMass and whom I spent most of the fun-time with when dealing with the instruments. They laid the foundation of my doctorate work and shared their life and study experience with me.

I am also pleased to say thank you to my officemate Dr. Marc von Hobe, who built the permeation oven, for generously sharing his research experience and encouraging me in difficult times.

I appreciate all the contributions from the colleagues in IEK-7, especially Dipl.-Ing. Vicheith Tan, Jochen Barthel, Nicole Spelten and Axel Schönfeld who gave me endless help in completing this thesis from the instrumentation side as well as Dr. Felix Plöger, Dr. Bärbel Vogel, Dr. Jwns-Uwe Grooß and Dipl.-Ing. Armin Afchine from the modelling side. In addition to their support at work, Anneliese Richter and Karlheinz Nogai helped me to practice my German skills.

I would also like to show my gratitude to Dr. Bernard Legras and Dr. Silvia Bucci from LMD France who provided us the TRACZILLA data and to Dr. Heinz Rongen and Markus Dick from ZEA-2 FZJ for optimizing the performance of the ion source and ion funnel.

As the supervisor for my master in South China University of Technology, Prof. Dr. Liming Wang led me into the field of atmospheric science. I would always remember his spirit of being encouraging and open-minded.

I would love to thank Dr. Christoph Kleimann for proofreading this work and being supportive for all what I have wanted.

In the end I am grateful to my sister, parents, grandparents and relatives for morally motivating me through my doctorate study and trusting me for chasing after my personal goals.

Appendix A

Additional table and figures

A.1 DBD ion source

Table A.1: Key parameters in FunMass for atmospheric measurements

Parameters	Airborne	Chamber
Ambient pressure [hPa]	60 – 100	1000 – 1050
Ambient temperature [°C]	- 62 – 38	15 – 38
Analyte flow [slm]	∼1.5	0.6
Inlet temperature [°C]	55 – 70	15 – 38
CO_2 (5.5) [sccm]	2	2
O_2 (6.0) [sccm]	450	400
IS voltage [kV]	3 – 3.8	2.5 – 4.2
IMR pressure [hPa]	30	20 – 30
Skimmer voltage [V]	6	6
BSQ voltage [V]	2.5	2.5
Lens voltage[V]	33	33
MCP voltage [V]	1950	1950
ToF pressure [$\times 10^{-6}$ hPa]	1.3 – 1.5	1.45
Mass range [Th]	11.7 – 540.4	14.3 – 539.3
Data storage [Hz]	2 Hz	2 Hz

A.2 StratoClim campaign

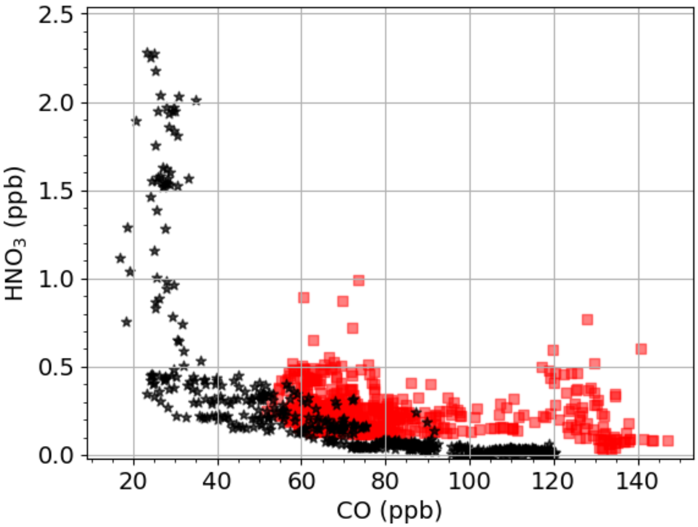

Figure A.1: The correlation of CO to HNO_3 in F6 (red squares) and F7 (black stars). CO-HNO_3 shows an expected 'L' shape: CO decrease with increasing HNO_3 below the tropopause and CO reaches the atmospheric background value (∼ 30 ppb) above the tropopause while HNO_3 steadily increases. HNO_3 shows a strong variability below the in the tropopause region in F6, which does not happen in F7. This is most likely due to convection or lightning-induced production.

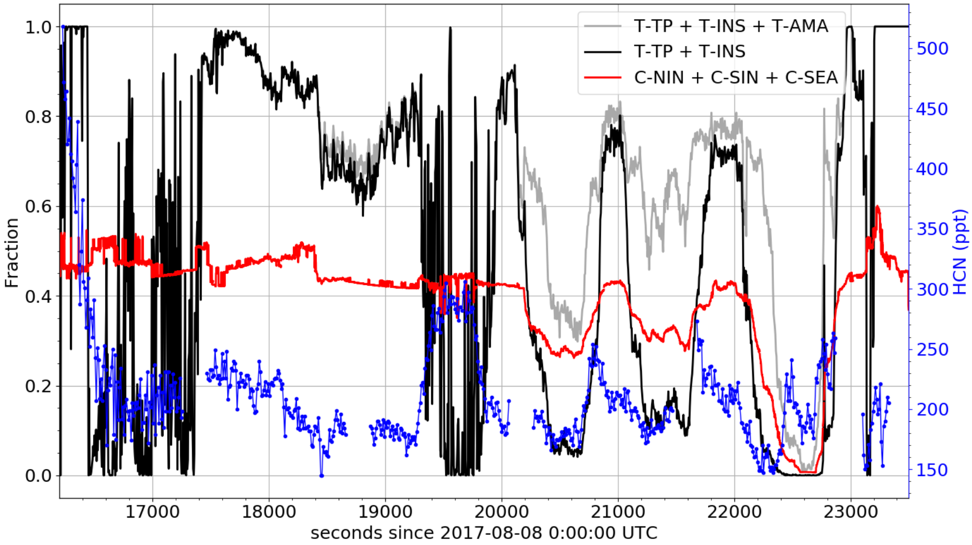

Figure A.2: Dominant source origins from TRACZILLA (black/grey) and CLaMS (red) contributing to the air parcels along the F7 path. Grey: total fraction of the tracer from the Tibet-Plateau, Indian Subcontinent and the AMA simulated with TRACZILLA. Black: similar to the black line but excluding the contribution made by the AMA. Red: CLaMS simulated tracer from Indian only. light red: CLaMS simulated tracer from Indian and Southeast Asia

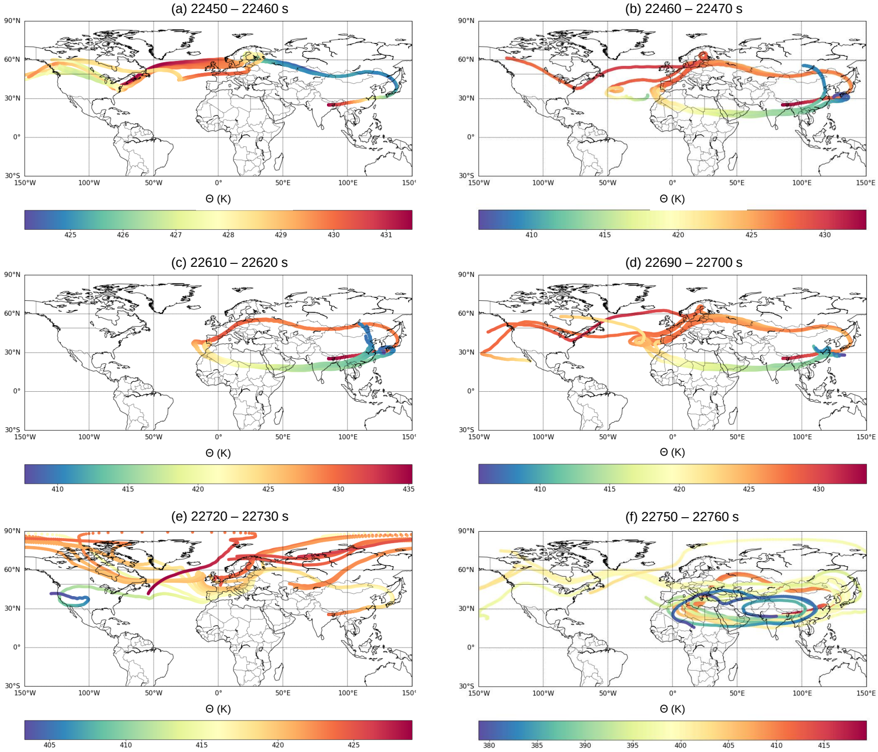

Figure A.3: The potential temperature evolution of the air parcels on the humps with high HCN and the ones in between for F7 on August 8, 2017. The subtitles of the plots marks the 10 s intervals extracted from Fig. 4.9 where the air parcels are subject to back-trajectory calculations. Figure (a) indicate that towards to the first hump the air parcel are more likely to be transported from the mid-latitude stratosphere. Figures (b) – (d) show the transition of the air from being a mixture of the mid-latitude stratosphere and anticyclonic air to being 100 % dominated by the anticyclonic vortex and to being a mixture again towards the second hump. From the second hump peak on as the aircraft was landing, the the input of high latitude stratosphere (Fig. (e)) became less influential and the air parcels are more probably ascent from the AMA (Fig. (f)). Note the different colour scales on the colour bars.

A.3 NO_3-isoprene campaign

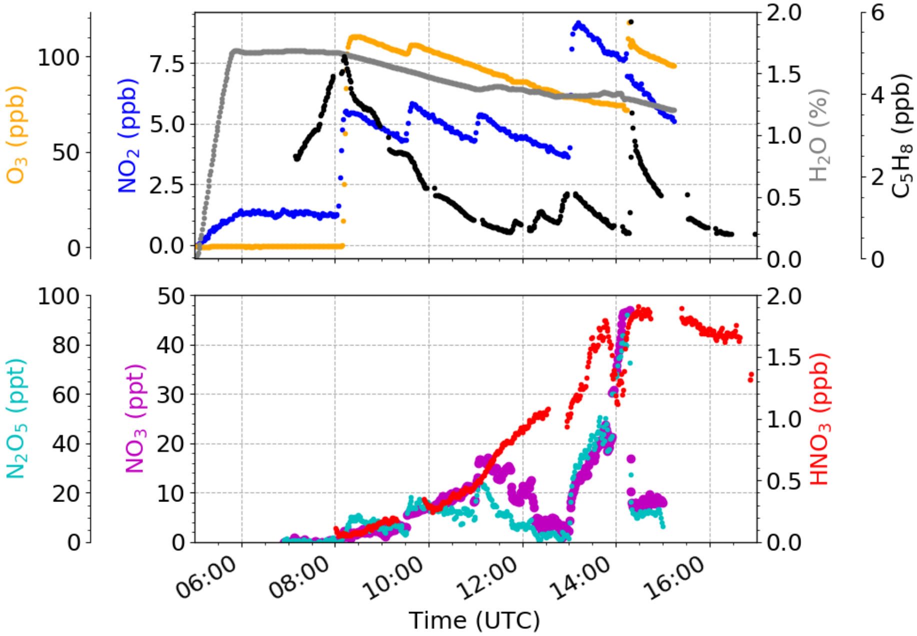

Figure A.4: Time series of HNO_3 and relevant species on August 22, 2018.

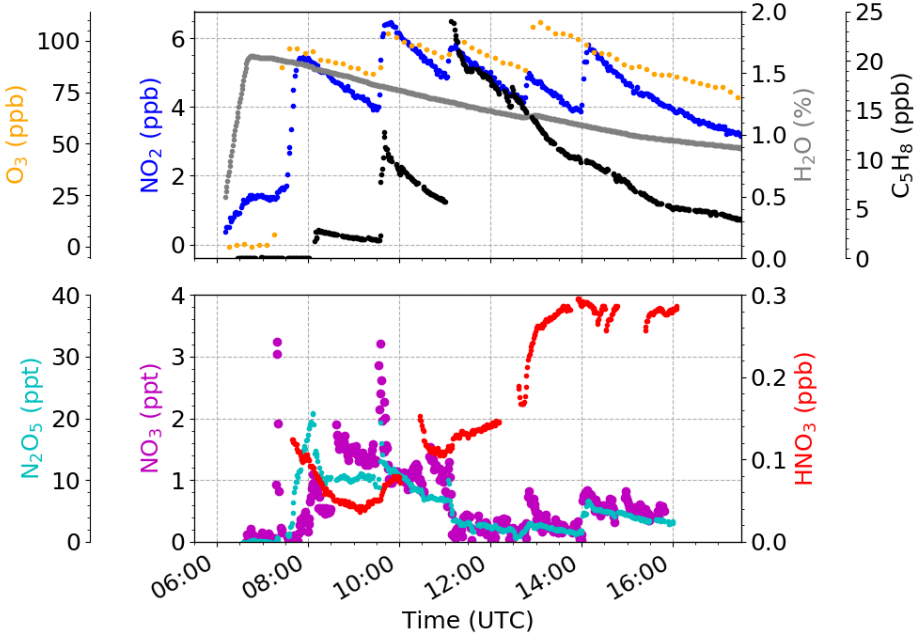

Figure A.5: The time series of HNO_3 and relevant species on August 24, 2018. The ozonolysis of β-caryophylene happened at 7:20 to organically coat the seed aerosol.

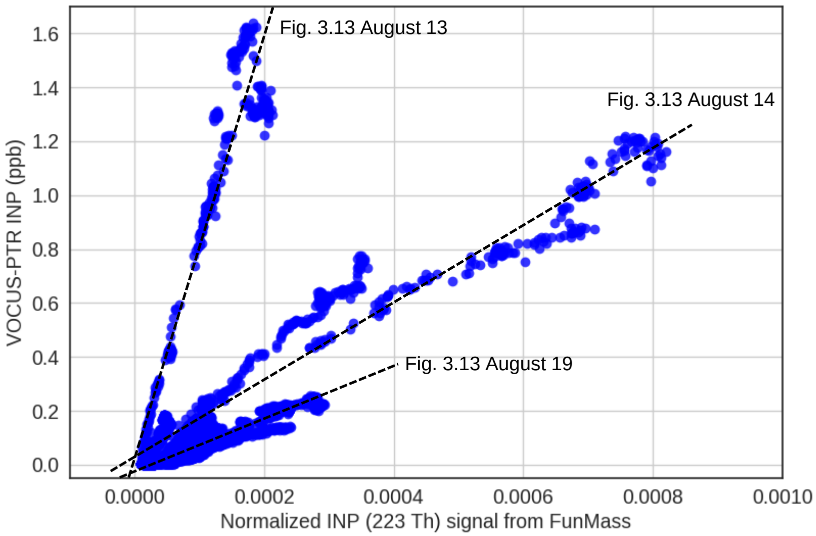

Figure A.6: Correlations between FunMass INP measurements and Vocus-PTR INP from August 10-24.

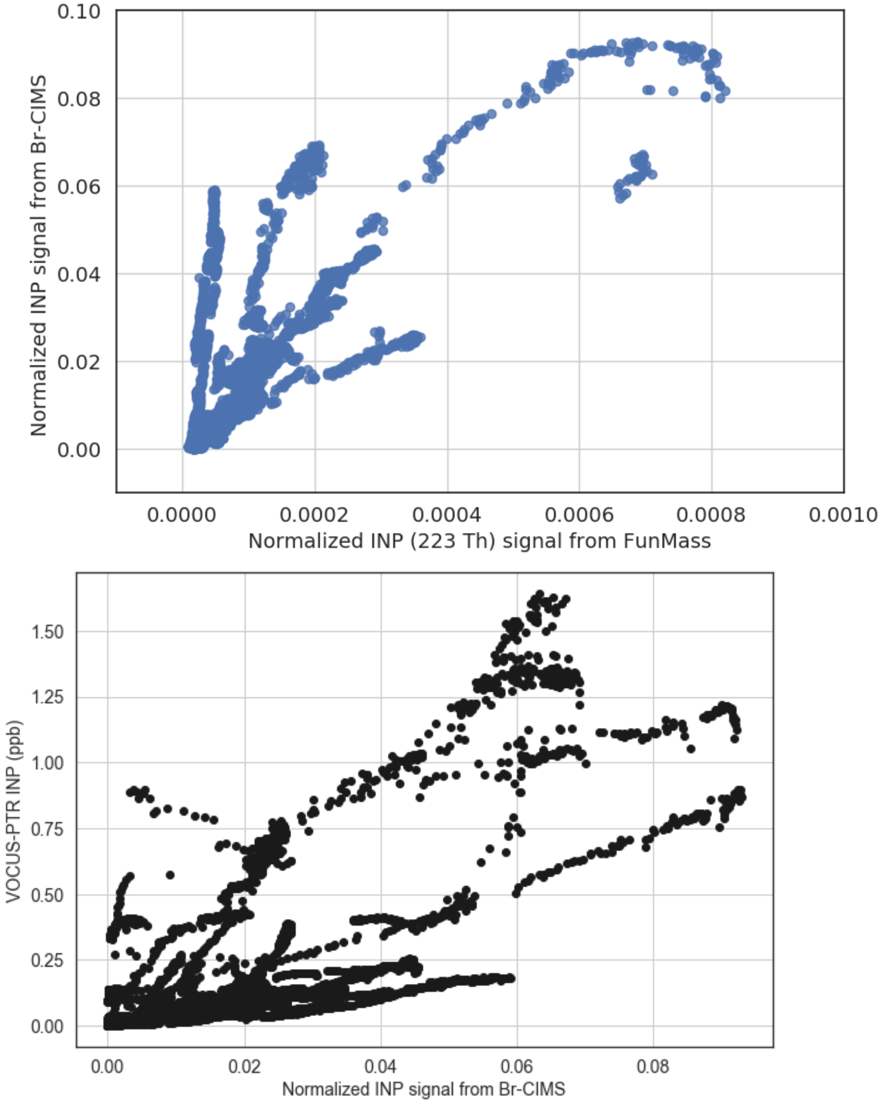

Figure A.7: INP measurements from August 10 – 24: Br^--CIMS *vs.* FunMass (top) and Vocus-PTR *vs.* Br^--CIMS (bottom).

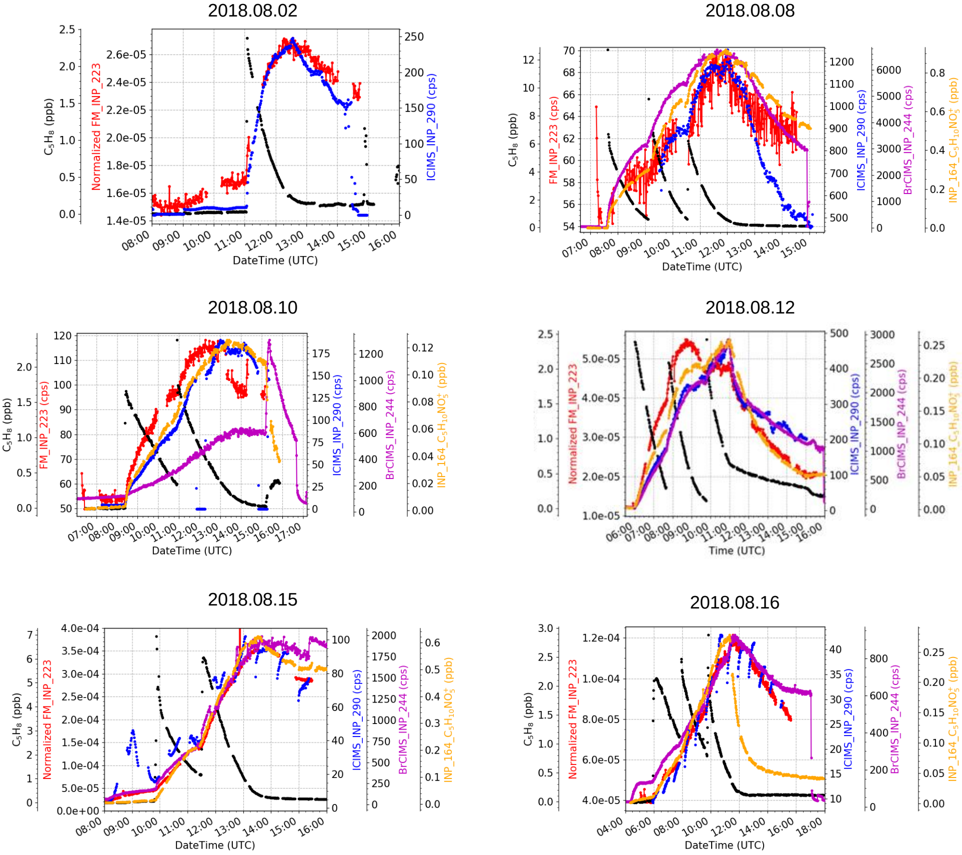

Figure A.8: INP detection on other days (1). Signals from I$^-$-CIMS and Br$^-$-CIMS are in the unit of counts per second (cps). INP from FunMass is shown in normalized product ion (223 Th) signal or cps if the reagent ion CO_3^- were severely consumed.

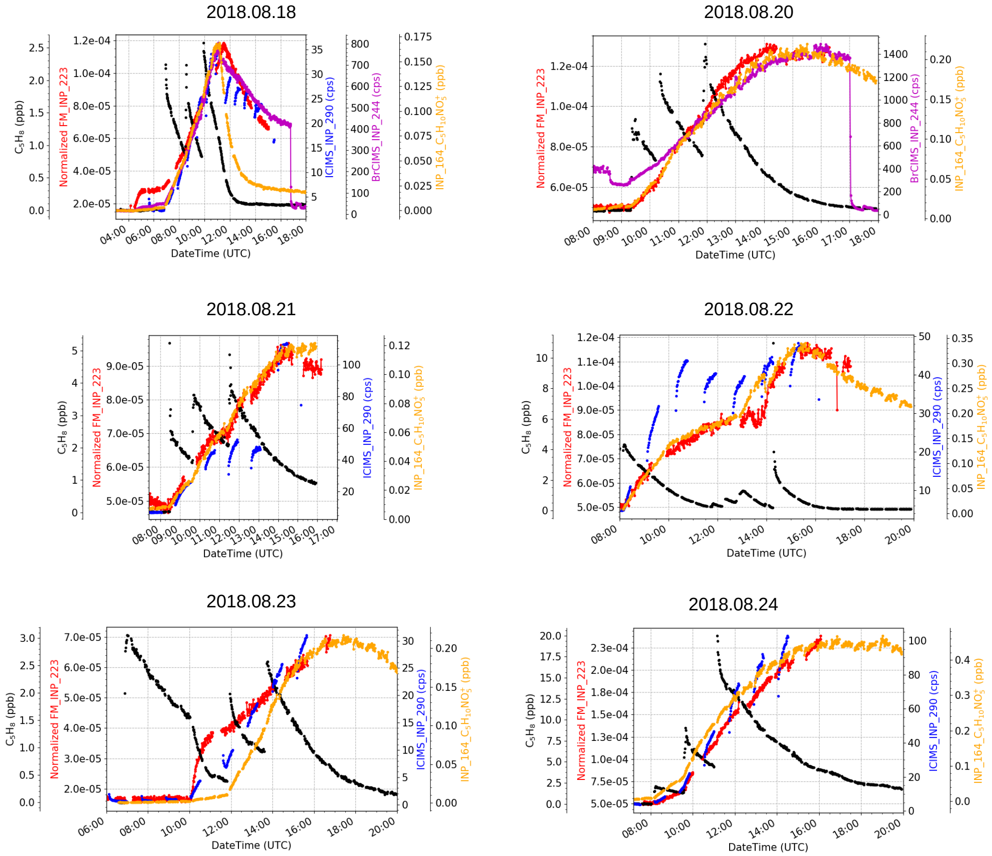

Figure A.9: INP detection on other days (2). Signals from I^--CIMS and Br^--CIMS are in the unit of counts per second (cps). INP from FunMass is shown in normalized product ion (223 Th) signal or cps if the reagent ion CO_3^- were severely consumed.

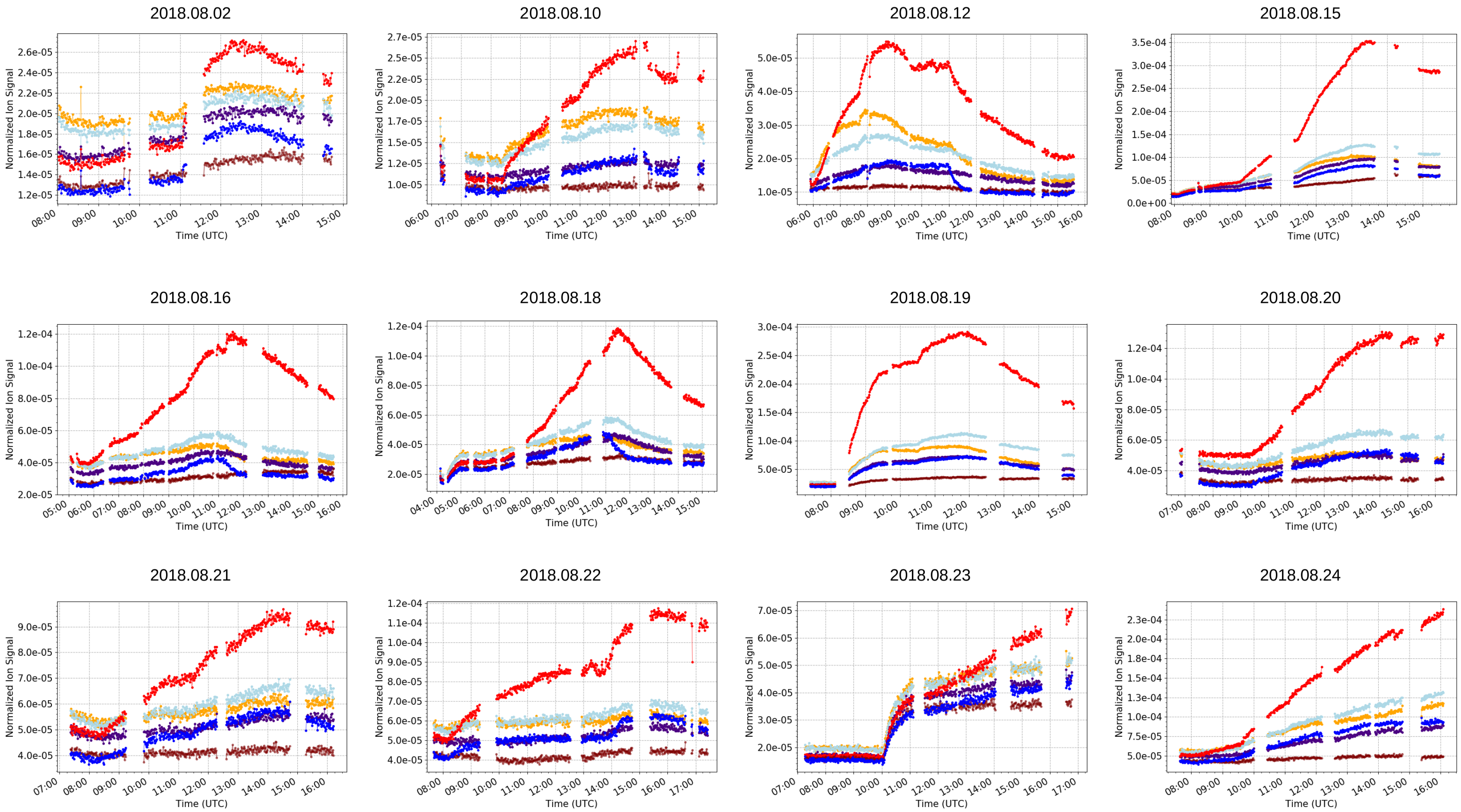

Figure A.10: Time series of normalized product ion signal of organic nitrate detected with FunMass on other experimental days: INP (223 Th, red), ICN (205 Th, orange), IHN (207 Th, light blue), IHCN (221 Th, indigo), ICPN (237 Th, maroon) and IHPN (239 Th, blue).

Band / Volume 512
Enhanced crosshole GPR full-waveform inversion to improve aquifer characterization
Z. Zhou (2020), VIII, 136 pp
ISBN: 978-3-95806-500-0

Band / Volume 513
Time-Resolved Photoluminescence on Perovskite Absorber Materials for Photovoltaic Applications
F. Staub (2020), viii, 198 pp
ISBN: 978-3-95806-503-1

Band / Volume 514
Crystallisation of Oxidic Gasifier Slags
J. P. Schupsky (2020), III, 127, XXII pp
ISBN: 978-3-95806-506-2

Band / Volume 515
Modeling and validation of chemical vapor deposition for tungsten fiber reinforced tungsten
L. Raumann (2020), X, 98, XXXVIII pp
ISBN: 978-3-95806-507-9

Band / Volume 516
Zinc Oxide / Nanocrystalline Silicon Contacts for Silicon Heterojunction Solar Cells
H. Li (2020), VIII, 135 pp
ISBN: 978-3-95806-508-6

Band / Volume 517
Iron isotope fractionation in arable soil and graminaceous crops
Y. Xing (2020), X, 111 pp
ISBN: 978-3-95806-509-3

Band / Volume 518
Geophysics-based soil mapping for improved modelling of spatial variability in crop growth and yield
C. Brogi (2020), xxi, 127 pp
ISBN: 978-3-95806-510-9

Band / Volume 519
Measuring and modelling spatiotemporal changes in hydrological response after partial deforestation
I. Wiekenkamp (2020), xxxvii, 276 pp
ISBN: 978-3-95806-512-3

Band / Volume 520
Characterization of Root System Architectures from Field Root Sampling Methods
S. Morandage (2020), xxii, 157 pp
ISBN: 978-3-95806-511-6

Band / Volume 521
Generation Lulls from the Future Potential of Wind and Solar Energy in Europe
D. S. Ryberg (2020), xxvii, 398 pp
ISBN: 978-3-95806-513-0

Band / Volume 522
Towards a Generalized Framework for the Analysis of Solar Cell Performance based on the Principle of Detailed Balance
B. J. Blank (2020), iv, 142 pp
ISBN: 978-3-95806-514-7

Band / Volume 523
A Robust Design of a Renewable European Energy System Encompassing a Hydrogen Infrastructure
D. G. Çağlayan (2020), xxii, 312 pp
ISBN: 978-3-95806-516-1

Band / Volume 524
Control and Optimization of a Lorentz Force Based Actuator System for External Flow
M. F. Seidler (2020), xii, 136 pp
ISBN: 978-3-95806-518-5

Band / Volume 525
ETV Online Tagung 2020
Industrielle Groß- und Hochtemperaturwärmepumpen im Energiesystem
D. Stolten, G. Markowz (Hrsg.) (2020), ca. 71 pp
ISBN: 978-3-95806-519-2

Band / Volume 526
Atmospheric Trace Gas Measurements Using Chemical Ionisation Time-of-Flight Mass Spectrometry
Y. Li (2020), xi, 110 pp
ISBN: 978-3-95806-520-8

Weitere ***Schriften des Verlags im Forschungszentrum Jülich*** unter
http://wwwzb1.fz-juelich.de/verlagextern1/index.asp

Energie & Umwelt / Energy & Environment
Band / Volume 526
ISBN 978-3-95806-520-8

Mitglied der Helmholtz-Gemeinschaft

JÜLICH
Forschungszentrum